

Modelling and Simulation of the Closed Injection Pultrusion Process

Zur Erlangung des akademischen Grades

Doktor der Ingenieurwissenschaften

der Fakultät für Maschinenbau

Karlsruher Institut für Technologie (KIT)

genehmigte

Dissertation

von

M.Sc. Renato Menezes Bezerra

Tag der mündlichen Prüfung: 24.10.2017

Hauptreferent: Prof. Dr.-Ing. Frank Henning

Korreferent: Prof. Dr.-Ing. Klaus Drechsler

Preamble

This Ph.D. thesis was undertaken during my engagement as a research employee at the Fraunhofer Society. During this period, I have had the pleasure to work at the Institute for Chemical Technology (ICT) in Pfinztal, Germany, later on at the project group Functional Lightweight Design (FIL) and at the Fraunhofer Research Institution for Casting, Composite and Processing Technology (IGCV) in Augsburg, Germany.

I would like to thank Prof. Dr.-Ing. Frank Henning for supervising my thesis and believing in the quality of my research work. I also thank Prof. Dr.-Ing. Klaus Drechsler for reviewing my work as a second supervisor and giving valuable insight.

Part of this thesis was conducted within the project PulForm funded by the German Federal Ministry of Education and Research (BMBF) (funding number 02PJ2035). Part of the experimental work was conducted within the general start-up activities of the project group FIL, funded by the Region of Bavaria, the City of Augsburg, BMBF and the European Union. I would like to acknowledge the financial support provided.

For the technical support, discussions and teamwork I would like to thank my colleagues Ingo Anschütz, Frederik Wilhelm, Sebastian Strauß and Alexander Chaloupka. I also appreciate the efforts of Dr. Iman Taha and Dr. John Puentes in reviewing this thesis and giving valuable input. A special thanks to Lazarula Chatzigeorgiou for making it possible to explore this topic at IGCV and for providing a flexible work environment. Many thanks also to all colleagues whom I may not have remembered here, but were helpful in many direct and indirect ways.

I would also like to thank my parents-in-law Yeda and Marcos for their continuous support and for their interest in my work. Finally, and most importantly, I would like to thank my wife Melissa for her endless support and patience and my daughters Luisa and Helena for clearing my mind from work every now and then, and pointing out the really important things in life. You are the joy of my life.

Augsburg, August 2017

Renato Menezes Bezerra

Abstract

Pultrusion is a mature processing technology for producing fiber reinforced composite profiles. The process is characterized by a relatively high level of automation at low investment and production costs in comparison to most other processing methods for composite parts. In a standard open bath pultrusion setup, an open tank filled with liquid resin is employed to wet the fiber reinforcement materials. Current technology and regulatory developments have started a trend that is expected to radically change the pultrusion industry state of the art in the long term. Examples include the tightening of working place regulations, the introduction of new resins of relatively short pot life (e.g. polyurethanes) to the pultrusion market, as well as the requirements of new applications with higher product quality demands (e.g. in the automotive sector). The design of pultrusion molds with integrated or attached cavities into which the resin is injected and thus impregnates the fiber reinforcements immediately before curing is foreseen to replace the open bath method.

In this thesis, simulation techniques are employed to get insight and a better understanding for the physical processes taking place within pultrusion molds with closed resin injection and impregnation: resin flow through the fiber stack while this is being compacted, heat transfer between material and mold, and resin curing reaction (coupled with changes in material state and release of exothermic reaction heat). To investigate these phenomena, material parameters of resin (curing kinetics and development of viscosity throughout curing) and fiber reinforcement (compressibility and permeability) are experimentally determined. The material parameters, a geometrical model of the pultrusion mold and suitable boundary conditions are used as the input for the numerical simulation conducted within a Computational Fluid Dynamics commercial software and complemented by an in-house Finite Difference code. The simulation calculates pressure, temperature, viscosity and degree of cure distributions within the mold cavity. Simulation results are compared to experimental processing conditions to validate the simulation model. Design details and process parameters are then varied and their impact on processing conditions is analyzed.

The simulation results have shown that the holistic approach pursued in this work, i.e. the coupling of thermo-chemical and flow models is needed for obtaining accurate predictions for the case of a fast reacting resin system. On the other hand, an expansion of the simulation models to account for mold body deformation would be necessary to improve the pressure rise prediction. Furthermore, depending on the cavity design, resin system and processing conditions, transient simulations would be needed for a better prediction and evaluation of process stability.

Kurzfassung

Pultrusion ist eine etablierte Herstellungstechnik für die Produktion faserverstärkter Kunststoffprofile. Der Prozess ist durch einen relativ hohen Automatisierungsgrad und geringe Investitions- und Betriebskosten im Vergleich zu den meisten anderen Herstellungstechniken für Faserverbundbauteile gekennzeichnet. Als Standard-Variante wird ein offener, mit flüssigem Harz gefüllter Behälter für die Tränkung der Faserverstärkungsmaterialien eingesetzt. Die Verschärfung von Gesetzen zum Schutz von Mitarbeitern am Arbeitsplatz, die Einführung neuer Harzsysteme mit kurzer Topfzeit (z.B. Polyurethane), sowie gestiegene Qualitätsanforderungen für neue Anwendungen (z.B. im Fahrzeugbau) haben einen Trend eingeleitet, der die Pultrusionstechnologie signifikant verändern soll. Die Auslegung von Pultrusionswerkzeugen mit integrierten bzw. zusammengebauten Werkzeugkavitäten, in die Harz eingespritzt wird, das die Verstärkungsstrukturen unmittelbar vor der Aushärtung tränkt, soll die offene Tränkungstechnik ersetzen.

In dieser Dissertation werden Simulationstechniken eingesetzt, um Erkenntnisse bzw. ein besseres Verständnis über die physikalischen Prozesse bei der Pultrusion mit geschlossener Harzeinspritzung und Imprägnierung zu gewinnen: das Fließen vom flüssigen Harz durch ein komprimiertes Faserpaket, Wärmeübertragung zwischen Material und Werkzeug, und die Aushärtung (verbunden mit Änderungen im Materialzustand und Wärmegenerierung durch die exothermische Reaktion). Um diese Prozesse zu untersuchen, werden Materialkennwerte des Harzsystems (Reaktionskinetik und Veränderung der Viskosität während der Aushärtung) und Faserstrukturen (Kompressibilität und Permeabilität) experimentell ermittelt. Ein geometrisches Modell des Werkzeugs und entsprechende Randbedingungen werden in eine kommerzielle Software numerischer Strömungsmechanik (englisch: Computational Fluid Dynamics, CFD) eingepflegt und der Prozess wird simuliert. Ein auf die finite Differenzmethode basiertes Simulationsprogramm wurde entwickelt, um das CFD-Modell zu ergänzen. Die Simulation liefert Druck-, Temperatur-, Viskositäts- und Aushärtegradfelder in der Kavität. Simulationsergebnisse werden mit Prozessparametern aus experimentellen Versuchen abgeglichen, um das Modell zu validieren. Geometrische Details werden parametrisiert, um den Einfluss auf die Prozessbedingungen zu evaluieren.

Die Simulationsergebnisse zeigen, dass der in dieser Arbeit verfolgte ganzheitliche Ansatz, d.h. die Kopplung eines thermochemischen Modells und des Strömungsmodells, zum Erzielen realitätsnaher Vorhersagen, zumindest für hochreaktive Harzsysteme erforderlich ist. Eine Modellerweiterung, welche die Ausdehnung der Werkzeugkavität berücksichtigt,

wäre hingegen für eine bessere Vorhersage des Druckanstiegs notwendig. Weiterhin, wäre für bestimmten Werkzeuggeometrien, Materialsystem bzw. Prozessfenster ein transienter Ansatz für eine realitätsnahe Vorhersage und für die Evaluierung der Prozessstabilität sinnvoll.

Contents

Preamble	I
Abstract	II
Kurzfassung	III
Contents	1
List of abbreviations	VIII
List of symbols	IX
1 Introduction and motivation	1
2 Objectives and outline of the thesis	3
3 State of the art	7
3.1 Pultrusion process overview.....	7
3.1.1 Standard pultrusion process.....	8
3.1.2 Closed injection pultrusion.....	10
3.1.3 Polymer Matrices for pultrusion	12
3.1.4 Fiber reinforcements	14
3.2 Resin chemorheological characterization	15
3.2.1 Reaction kinetics	16
3.2.2 Chemorheology.....	18
3.3 Reinforcement characterization	21
3.3.1 Compressibility.....	22
3.3.2 Permeability	23
3.4 Modelling and simulation	27
3.4.1 Numerical solving techniques.....	29
3.4.2 Modelling and simulation of the pultrusion die	30
3.4.2.1 Thermo-chemical modelling	31
3.4.2.2 Fluid dynamics modelling	32
3.4.2.3 Thermo-mechanical modelling	34
3.4.2.4 Modelling of pulling force.....	36
3.4.3 Simulation of the closed injection process	38
4 Resin characterization and modelling	40
4.1 Materials and methods	40
4.1.1 Resin system.....	40
4.1.2 Differential Scanning Calorimetry (DSC)	42
4.1.3 Rheology measurements	42
4.2 DSC measurement results	43
4.3 Kinetic modelling	45

4.4	Rheology measurement results	49
4.5	Rheology modelling.....	52
5	Fiber characterization and modelling	55
5.1	Material and methods.....	55
5.1.1	Reinforcement materials	55
5.1.2	Compressibility method	56
5.1.3	Permeability method.....	59
5.1.3.1	Unsaturated flow condition	61
5.1.3.2	Saturated flow condition	62
5.2	Compressibility measurement results	64
5.3	Permeability measurement results	69
5.3.1	Continuous filament mats.....	69
5.3.2	Roving stacks.....	70
6	Experimental trials with closed injection dies.....	75
6.1	Description of trial assemblies.....	76
6.1.1	Conical die	77
6.1.2	Tear drop die.....	78
6.2	Experimental data	79
6.2.1	Conical die	79
6.2.2	Tear drop die.....	83
6.2.3	Distribution of fibers within the tear drop injection chamber	86
7	Modelling and simulation of the closed injection pultrusion	91
7.1	Modelling of the closed injection pultrusion	91
7.1.1	Geometric design	93
7.1.1.1	Conical die	93
7.1.1.2	Tear drop die.....	95
7.1.2	Meshing strategy.....	96
7.1.2.1	Conical die	96
7.1.2.2	Tear drop die.....	97
7.1.3	Model parameters	98
7.1.3.1	Conical die	99
7.1.3.2	Tear drop die.....	103
7.1.4	Stress-strain model	105
7.1.4.1	Model development and validation	105
7.1.4.2	Application in pultrusion process	108
7.1.5	Simulation procedure	109
7.2	Simulation studies	110

7.2.1	Evolution of curing reaction	110
7.2.2	Flow behavior of liquid resin	115
7.2.2.1	Comparison with analytic models	116
7.2.2.2	Flow behavior in the conical inlet section.....	120
7.2.2.3	Flow behavior in the tear drop impregnation section	125
7.2.3	Parametrization of geometric design	128
8	Conclusions and outlook.....	136
	Appendix.....	139
	Appendix A: Processing data from pultrusion experimental trials	139
	Appendix B: Mesh quality parameters of the tear drop die 3D model	141
	Appendix C: Analytical model for the pressure rise in a conical inlet section	142
	References.....	144

List of abbreviations

ADE	<i>Alternating Difference Explicit discretization method</i>
CF	<i>Carbon Fiber</i>
CFM	<i>Continuous Filament Mat</i>
CSM	<i>Continuous Strand Mat</i>
CTE	<i>Coefficient of Thermal Expansion</i>
CV/FD	<i>Control Volume based Finite Difference</i>
DGEBA	<i>Diglycidyl Ether Bisphenol A</i>
DSC	<i>Differential Scanning Calorimetry</i>
EP	<i>Epoxy</i>
FDM	<i>Finite Difference Method</i>
FE/NCV	<i>Finite Element with Nodal Control Volume</i>
FEM	<i>Finite Element Method</i>
FRP	<i>Fiber Reinforced Plastic</i>
FSI	<i>Fluid-Structure Interaction</i>
FTIR	<i>Fourier Transform Infrared Spectroscopy</i>
FVM	<i>Finite Volume Method</i>
GF	<i>Glass Fiber</i>
IMR	<i>Internal Mold Release</i>
LCM	<i>Liquid Composite Molding</i>
MDI	<i>Methylene Diphenyl Diisocyanate</i>
NCF	<i>Non-Crimp Fabric</i>
OSH	<i>Occupational Safety and Health</i>
PU	<i>Polyurethane</i>
RTM	<i>Resin Transfer Molding</i>
TCR	<i>Thermal Contact Resistance</i>
TTT	<i>Time-Temperature-Transformation</i>
UP	<i>Unsaturated Polyester</i>
VE	<i>Vinyl Ester</i>

List of symbols

Symbol	Description	Units
α	Degree of cure	
α_g	Degree of cure at gelation	
A	Pre-exponential factor of the Arrhenius equation	s^{-1}
E	Activation energy of the Arrhenius equation	J/mol
H_R	Total heat of reaction	J/kg
m, n	Order of reaction	
K_{cat}	Autocatalytic factor	
τ	Stress	Pa
γ	Strain	
γ_A	Strain amplitude	
ω	Angular frequency	rad/s
δ	Phase lag / Loss factor	rad
G'	Shear storage modulus	Pa
G''	Shear loss modulus	Pa
η	Fluid apparent or dynamic Viscosity	Pa·s
P	Pressure	Pa
B	Bending stiffness of fiber	N.m ²
V_a	Maximum theoretical fiber volume fraction	
\mathbf{v}	Flow velocity vector	m/s
U	Pulling speed	m/s
K	Permeability of the porous medium	m ²
\emptyset	Porosity	
∇P	Pressure gradient	Pa
k_c	Kozeny-Carman constant	
V_f	Fiber volume content	
ρ	Density	kg/m ³
λ	Thermal conductivity	W/(m·K)
α_v	Volumetric coefficient of thermal expansion	K ⁻¹
β	Coefficient of volumetric shrinkage of resin due to curing	
θ	Tapering angle of die inlet region	°

1 Introduction and motivation

Pultrusion is a mature processing technology for producing fiber reinforced composite profiles. The process features a relatively high level of automation at low investment and production costs in comparison to most other processing methods for composite parts. Pultrusion has thus been characterized by the use of low cost raw materials (predominantly unsaturated polyester resins and glass fiber rovings and other reinforcements). On the other hand, pultrusion allows, with few exceptions, only the production of simple geometries (profiles of constant cross section). Pultruded products have found applications mainly where corrosion resistance (building and infrastructure) and dielectric properties of the material are advantageous. Applications in the area of lightweight design have not been fully explored (e.g. in the automotive industry). Another process feature, as it is widely implemented by industry, is the use of a tank filled with liquid resin that is open to the atmosphere through which the fibers are guided and thereby wetted out, the so-called open bath technique. This results in a process step with no in-line monitoring which is difficult to trace back in case of product non-conformity. The resin also changes its properties with time, such that a variability of product quality must be tolerated. Furthermore, the use of an open resin tank generates working place environmental and health issues, since some resin components are volatile and toxic.

The tightening of regulations by Occupational Safety and Health (OSH) agencies, the introduction of new resins of relatively short pot life (e.g. polyurethanes) to the pultrusion market, as well as the requirements of new applications (e.g. in the automotive sector) have started a trend that is expected to radically change the state of the art of the pultrusion industry. It is foreseen that the open bath impregnation method will be replaced by the use of pultrusion molds with integrated cavities into which the liquid resin is injected and thus wets the reinforcement fibers, or the retrofitting of standard molds by attaching such an injection and impregnation chamber upstream.

The design of such a die, especially the injection and impregnation cavity, is more complex than that of a standard die. The main reason is that the fiber stack must, in this case, be thoroughly impregnated with resin while being in a compact condition or while being compacted along a short impregnation cavity length to the die final cross section. Several designs have been proposed over the years in patents and publications. The development has been done in most cases by trial and error. Designs actually implemented by the industry are normally kept undisclosed as company's internal know-how.

Although pultrusion may be regarded as a simple manufacturing technique, it is actually characterized by multiple physical processes occurring concurrently within the mold: heat transfer between material and mold, resin curing reaction (coupled with changes in material state and release of exothermic reaction heat) and development of internal stresses and deformation in the material induced by the thermal history. The closed injection technique increases the physical complexity, as it shifts the critical impregnation step from a simple mechanical assembly in the open bath setup to a delimited cavity volume where liquid resin flows through the reinforcement stack.

The recent developments in processing with closed injection techniques have focused on achieving composite profiles with the same quality as obtained with the standard open bath method. However, such developments have not been accompanied by efforts to fundamentally understand the occurring physical phenomena and their interactions. A fundamental knowledge is crucial for the continuous improvement and the establishment of the closed injection technique as a new industry standard. The goal of this thesis is therefore to fill this gap and contribute to a better understanding for the physical processes taking place within pultrusion molds with closed injection and impregnation.

2 Objectives and outline of the thesis

The goal of this thesis is to get insight and a better understanding for the physical processes occurring within closed resin injection and impregnation pultrusion molds. All relevant physical and chemical processes leading to the formation of the composite profile take place primarily inside this mold. A liquid resin formulation is injected and flows through the initially dry fiber reinforcement stack, thus wetting it out. At the same time, the reinforcement stack is being gradually compressed until a desired fiber volume ratio is achieved in the curing section of the mold. Within this curing region, the material is heated up, initiating a thermosetting reaction. The curing process is characterized by changes in the physical state of the resin from liquid through gel to a solidified state, and by the release of heat from the exothermic reaction. The thermal history causes the development of internal stresses and deformation in the material due to two effects: thermal expansion and shrinkage due to curing.

This thesis is built upon experimental characterization and numerical solving techniques, employed to develop a tool that attempts to simulate the following phenomena:

- Flow of liquid resin through the reinforcement stack in a closed injection and impregnation cavity
- Heat transfer between the mold and the composite material
- Evolution of curing degree and viscosity along the pultrusion die

A review of the research published on this topic is presented in chapter 3. In general, previous studies have focused on one of the physical processes occurring in the processing, e.g. thermal simulation or the fluid flow within the inlet section. The present work pursues a holistic approach by simulating both phenomena with one integrated tool. Focus is given in the characterization and simulation studies to a novel resin system based in a two-step-curing reaction mechanism [1]. Although not a formulation typically applied in pultrusion processing, this resin system has a great potential for new applications with increased geometrical complexity. Furthermore, the first reaction step leading to a B-stage shows a behavior similar to two-component polyurethanes, which are of great interest in current pultrusion developments. The methods developed in this work can therefore be applied to other resin systems of high reactivity and short pot life upon mixing. It is discussed whether the holistic approach is expected to deliver more realistic results, for this particular resin system and/or in general pultrusion processing cases.

To investigate these phenomena by means of process simulation tools, it is important to use realistic material models. Therefore, a high value was set in this work on obtaining material parameters of resin (curing kinetics and development of viscosity throughout curing) and fiber reinforcement (compressibility and permeability) in processing-like conditions. The experimental techniques employed and the results obtained are discussed in the chapters 4 and 5. A set of processing data was also obtained from experimental trials. The trial setups and a qualitative analysis of processing conditions are given in chapter 6. In chapter 7, the developed simulation models are presented, simulation results are compared to experimental data, and parametrization studies are discussed. The goal of such studies is to evaluate the suitability of the developed models as a tool for the prediction of processing conditions and for mold design optimization.

The upcoming chapters cover the experimental and modeling efforts made to reach the thesis goals stated above.

Chapter 3: State of the art

This chapter includes a thorough literature review covering previous research relevant to the topic of the present thesis, as well as the state-of-the-art practiced by industry. An overview of the pultrusion process and its position within the composites manufacturing field is given. Characterization techniques of raw materials (fiber reinforcements and matrices) are also presented, especially those applied to the present study. Modelling efforts of these properties are described. Studies dealing with modelling and simulation of the pultrusion process are reviewed, and comparison are made between the work of different research groups.

Chapter 4: Resin characterization and modelling

In this section, the experimental work done on the chemorheological characterization of the studied resin system is described, i.e. the evolution of reaction rate as a function of time and temperature as well as the changes in resin physical state as curing progresses. Firstly, the resin formulation is presented along with applied experimental methods, namely DSC and rheology measurements. In the following subsections, results obtained from each of the methods are then presented along with the development of models for the prediction of the resin properties throughout the curing process.

Chapter 5: Fiber characterization and modelling

To get a better estimate of input parameters to the process simulation, methods for characterizing fiber reinforcements typically employed in pultrusion were developed and applied in this study. Fiber stacks composed of glass and carbon fiber rovings (unidirectional orientation) as well as glass continuous filament mats were characterized in terms of compressibility and in-plane permeability. Attempts are made to correlate the characterization results with models available in the literature. The limitations of the experimental techniques are discussed.

Chapter 6: Experimental trials with closed injection dies

Experimental trials with two different pultrusion dies with injection and impregnation chambers, namely a conical and a “tear drop” inlet geometry, are conducted. The objective of the trials is to obtain processing data useful for validating the simulation studies conducted in Chapter 7. The trial assemblies, their similarities and differences related to processing are described. Examples of processing data obtained from the experimental trials with both dies are presented and analyzed in terms of their significance to processing in this section. Qualitative correlation between processing parameters is also discussed. The distribution of fibers within the tear drop die impregnation region is evaluated by microscopic analysis.

Chapter 7: Modelling and simulation of the closed injection pultrusion

The development of models for the two pultrusion dies under investigation are presented in this chapter. The assumptions made for the computational domains, boundary conditions and other input parameters set in the commercial software package are described and discussed. A simplified in-house finite difference code is also developed and used to calculate the contribution of thermal expansion and curing shrinkage effects to the liquid pressure inside the die. The simulation tool calculates pressure, temperature, viscosity and degree of cure distributions within the mold cavity.

The simulation studies undertaken for the pultrusion dies with conical (2D model) and tear drop (3D model) geometries are presented. Simulation results are compared to processing parameters obtained from experimental trials. The simulation results for the pressure rise within the conical die are also compared to analytical models found in the literature. The effects of input and geometric design parameters on simulated processing conditions are evaluated by parametrization studies.

Chapter 8: Conclusions and outlook

The obtained results are summarized, and the applicability and usefulness of the developed simulation tool are discussed in this chapter. Suggestions for possible further work in this field are also discussed.

3 State of the art

In the following sections, a review of available literature relevant to the research approach of this study, as well as the state of the art practiced by the industry will be discussed. An overview of the pultrusion process and its position within the composites manufacturing field is given. Characterization techniques of raw materials (fiber reinforcements and matrices) are also presented, especially those applied and relevant to the present study. Modelling and simulation efforts applied to pultrusion processing are reviewed as well.

3.1 Pultrusion process overview

The class of materials known as fiber reinforced plastics (FRP) is a very heterogeneous group which have, as common constituents, stiff fibers (reinforcing material) embedded in a relatively compliant polymer matrix. Further classifications can be made in terms of the average length of the reinforcing fibers (short, long and continuous FRPs), the type of matrix (thermoplastic or thermoset) or manufacturing technique. In almost all cases, and particularly with thermosetting matrices, the composite material with its final properties actually originates with part production, i.e. with curing. The material properties are therefore dependent on the processing route.

Among the composites processing techniques, pultrusion is considered one of the most cost-effective – a feature counterbalanced by the limitation in the possible part complexity. A comparison of different manufacturing techniques available for the production of continuous FRPs is shown in Figure 3.1.

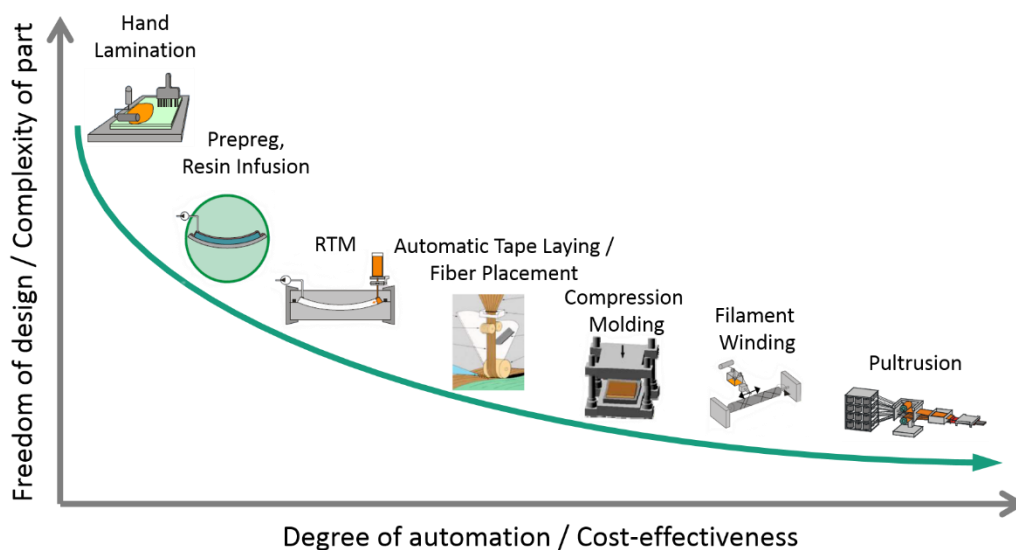


Figure 3.1: Comparison of composite manufacturing techniques, adapted from [2] [3]

The techniques shown are not intended to represent all available manufacturing routes. In fact, the field is characterized by a broad range of tailor-made processing variations and combinations of different processes. For example, efforts have been recently made in the combination of processes to overcome the limitations in freedom of design in pultrusion [1] [3].

Although a considerable amount of literature can be found describing pultrusion processing of thermoplastic matrices, the state of the art practiced by the industry does not yet reflect the research output. Furthermore, the term “thermoplastic pultrusion” has been used to describe processing techniques which are quite different from each other, depending on the state of the matrix (as monomer or polymer) prior to processing. Thus, further literature review will focus only on pultrusion with thermosetting matrices. The process, in its standard form, is described in the next section, and can be considered as a mature technology within the composites field, with first patents filed in the 1950s and first commercial products reported in the 1960s [4].

3.1.1 Standard pultrusion process

The pultrusion process allows the production of profiles of constant cross section. A typical production line consists of roving creels, racks for positioning and unwinding of continuous filament mat (CFM) layers or other planar textile bands, a resin tank, a pre-forming assembly composed of perforated plates and other guiding parts, a heated die, a pulling device and a flying cut-off saw (see Figure 3.2).

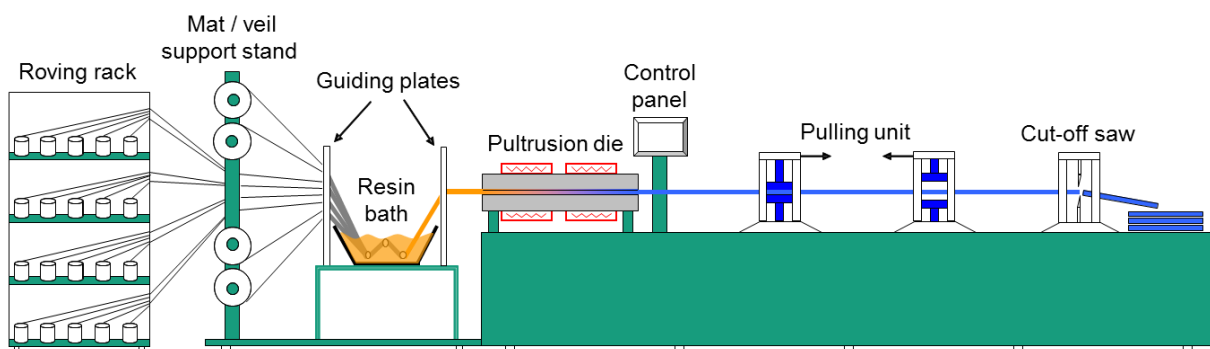


Figure 3.2: Schematic representation of the standard pultrusion process

Wetting out of the fibers is primarily achieved by pulling them through the tank filled with liquid resin (open bath impregnation), where the roving bundles are spread to allow for easier wetting within the tow. Subsequently, the wet fiber bundle is guided through a preforming

assembly used to position and collimate the reinforcing material to the desired cross section geometry just prior to entering the die. Plane textiles may also be pulled through the resin bath or wetted out when entering the die by the excess of resin carried by the rovings. By pulling the whole fiber stack into the die, the excess of liquid resin and air are squeezed out, so that pultruded parts of low void contents (typically between 1 and 2% vol.) can be produced.

By passing through a heated die, usually made of tool-steel, the curing reaction is triggered and the matrix goes from the state of liquid resin to gel and finally solid. The physical changes during curing are described in section 2.3.1. Heating is most commonly achieved by attaching electric heating plates to the die. Other methods include machining holes in the die where heating cartridges are fitted, or channels for heating oil circulation. In order to allow a gradual increase in resin temperature, more heating zones with different set temperatures can be placed along the length of the die. Temperature management of the die is considered an important processing aspect for producing good quality parts [4].

Another important processing parameter is the force required for pulling the material through the die. Given a steady state of production, an increase in pulling force may indicate some process instability, for example die clogging. Some research groups have proposed models for the pulling force, in which the total force needed to pull the material through the die is composed of contributions arising from different physical processes in specific sections of the pultrusion die. There is no broad agreement in the literature as to which of the physical processes has the major contribution in the pulling force. These studies will be reviewed in section 3.4.2.4.

Many pultrusion companies offer a range of “standard” profiles for which suitable tooling, i.e. pre-forming assembly, die and clamping pads for the pulling device, is already available. In addition to that, custom manufacturing of a particular profile geometry is also possible. The limitation of the profile complexity is usually given by the ability to stably preform and guide the material, especially plane textiles, to adequately fill the cross section. In this respect, the pultrusion industry has been strongly driven by proprietary know-how and staff experience in tooling design and manufacturing. General guidelines are not found in literature. In fact, for a given profile geometry, the preforming assemblies of two pultrusion companies may be rather different from each other.

The use of an open bath method for impregnation, resulting in poor process quality control as well as environmental and health issues has prevented pultrusion from entering high-end

markets and applications. Pultruded products have thus found applications mainly where the corrosion resistance (structural parts in exterior applications) and the dielectric properties of the material (as insulating parts in electrical assemblies) are of interest, rather than by exploiting their lightweight potential.

3.1.2 Closed injection pultrusion

Alternatively to using a resin tank to wet out the reinforcement material, the liquid resin can be directly injected into a mold of constrained volume, through which the reinforcement material is pulled and wetted out before the curing process sets on. Although in principle the pultruded profile coming out of the die is the same as in the case of open bath pultrusion, the wetting-out process is quite different. Intuitively, wetting out will be more difficult in the case of closed injection pultrusion, as the resin must flow through a more or less compacted reinforcement stack. The wetting-out quality is expected to be dependent on the die design, more specifically on the design of a so called injection and impregnation chamber. The advantages of closed technique are the possibility of processing resins of short pot life and the decrease of harmful volatile resin components in the working place.

Pultrusion processing with the operation of dies with injection and impregnation chambers is already practiced by the industry, although quantification is difficult. Companies which already market profiles based on 2-component polyurethane resins are compelled to implement some form of spatially constrained, usually closed impregnation method, due to the low resin pot life. Other companies, for example Fiberline (Denmark), have been known to use closed injection molds to produce standard profiles based on traditional polyester and vinyl ester resins [5].

Design details of such molds are not readily available in technical literature. Some patents have described injection chambers, for example Koppernaes et al [6] and Gauchel and Lehman [7]. Koppernaes has described a so called "tear drop" geometry, i.e. a conical constricting cavity, which can be implemented repeatedly in series along the die length. According to the patent, design of multiple chambers in series allows a more effective degassing during fiber wetting out. Gauchel has patented a mold geometry in which a conical constricting cavity is also available. However, in this design the resin is injected at a position along the die length where the fiber stack is already in compacted condition, i.e. the cross section corresponds to that of the profile. According to the patent, the suitability of this die design to processing is given for a small angle ($<1^\circ$) of the conical region. The argumentation for this is given on the basis of the relative permeabilities of rovings in longitudinal and

transverse orientations. This issue will be discussed further in section 3.3.2. Schematic drawings of both patent designs are presented in Figure 3.3.

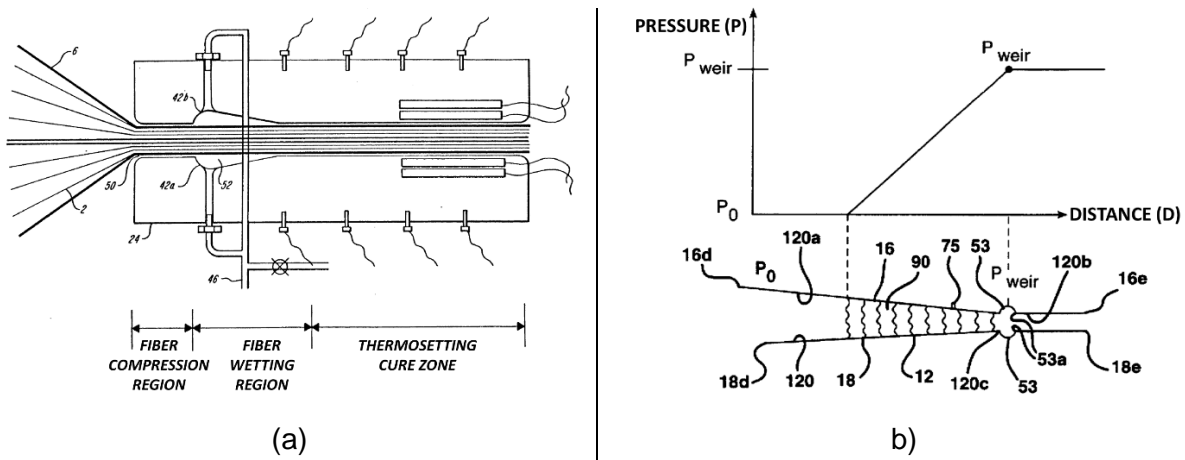


Figure 3.3: Die designs with resin injection chambers according to patents of (a) Koppernaes [6] and (b) Gauchel [7]

Brown et al. [8] describes in a series of patents a technique which could be called a “hybrid” between an open bath and a closed chamber (see Figure 3.4). By this method, the tows are fed to the impregnation unit composed of two chambers. The first chamber is similar to a bath, where the resin flows between the tows. The tows are evenly distributed within the cross section of the chamber, which is much larger than the end profile cross section. Tow distribution is defined by the hole pattern in the backing plate. Resin is constantly metered or poured through an opening to atmosphere on top of the chamber. The liquid level is maintained high enough so that all tows are submersed. A second chamber with a tapered cross sectional area follows, which leads to homogenous wetting within the tows, i.e. of individual filaments. The inventors argue that in the first chamber flow is driven predominantly by the Darcy’s law of flow through porous media (see section 3.3.2), while in the second chamber capillary flow becomes significant or even the predominant wetting mechanism.

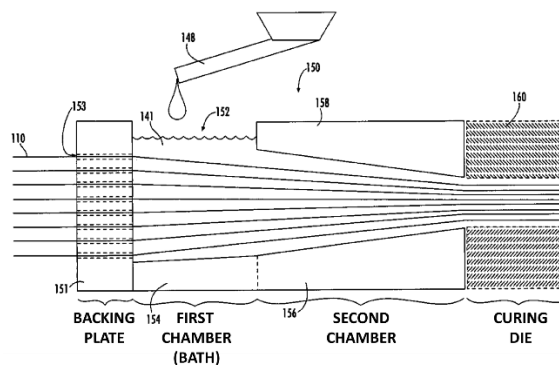


Figure 3.4: Impregnation chamber according to Brown [8]

Suitable dies may be designed as an integrated mold, i.e. an injection and impregnation region is machined from the same piece of tooling steel, or as separate mold parts which are mechanically fitted to each other. Both concepts have advantages and disadvantages. By the integrated design no joint faces are present in which resin could accumulate and which must be properly sealed. On the other hand, separate die parts allow a more efficient thermal insulation between the cold impregnation region and the hot curing section. Another advantage of the non-integrated approach is that standard pultrusion dies can theoretically be retrofitted to closed injection operation.

Dubé et al [9] described a prototype pultrusion line vertically assembled for the production of rods. The die has a short tapered section at the top, where the fibers are fed and the resin is metered by gear pumps. Some other experimental studies were published based on a tapered or conical die inlet in which the resin is directly injected [10] [11]. Li et al [12] presented experimental results for two different die inlet geometries, namely a tear drop chamber according to Koppernaes and a conical geometry according to Gauchel (see Figure 3.3). This work was done in cooperation with Engelen (Dow Chemical Company, Freeport, Texas).

Srinivasagupta et al [13] assembled a bench scale pultrusion line and described a die with an inlet section designed as a constant cross section of 5 mm height and 75 mm length, followed by a tapered section of 0.5° angle and 55 mm length. They compared experimental processing parameters with results obtained from simulation (see section 3.4.3).

More recently, Engelen [14] presented a die design for producing pultruded flat profiles with different thicknesses, with a fixture to bolt on three different injection chambers: a tear drop cavity, a dual cavity and a “wave” design, the latter one especially for spreading out a roving reinforcement stack.

3.1.3 Polymer Matrices for pultrusion

Most common matrices used in pultrusion are thermosetting resins. Thermosets reach their end properties only after curing takes place, i.e. a crosslinking reaction between different resin components of low molecular weight leading to three-dimensional networks of macromolecules [15]. Typical resins used in pultrusion are unsaturated polyesters (UP), vinyl esters (VE), epoxies (EP) and polyurethanes (PU).

UP and VE resins are typically formulated by oligomeric prepolymers (so called backbones) containing carbon-carbon double (i.e. unsaturated) bonds and diluted in styrene. The styrene functions as a crosslinking agent, by building polystyrene linear chains bonded to the backbones at the double bonds (and thus saturating these functional groups). The polymerization is initiated by organic peroxides, which split into free radicals when the resin reaches certain temperature levels. By selecting an appropriate mixing ratio of different peroxides, the reaction rate can be adjusted to occur smoothly, that is, without sudden large heat release rates leading to uncontrolled autocatalysis.

EP and PU resins are on the other hand typically two-component resin systems, in which the components are monomers reacting at a defined stoichiometry ratio. EP systems are most commonly based on diglycidyl ether Bisphenol A (DGEBA) resins and either an amine or anhydride as crosslinking hardening agent. Anhydrides are most commonly used in pultrusion due to their lower toxicity, thus allowing for an open bath wetting out technique. PU systems are composed of a polyol blend and an isocyanate which react by urethane polyaddition. By varying the functionality of both polyol and isocyanate, the matrix end properties can be adjusted over a large range from rubbery to rigid thermoset. By formulating a resin with difunctional polyol and isocyanate (with functional groups located in the ends of the monomer chains), a thermoplastic material can also be produced.

Other typical additives added to the formulation are fillers, e.g. calcium carbonate, added to lower material costs and improve surface quality, and internal mold release (IMR) agents, which effectively reduce the force necessary to pull the material through the die. There is no general agreement as to which mechanism is primarily responsible for the reduction in pulling force. In [4] it is argued that for a specific IMR based on aliphatic acid phosphate, acid groups bond to the metal surface while linear aliphatic groups provide surface lubrication.

A relatively new class of thermosets called Daron® turane has been developed by Aliancys, formerly DSM Composite Resins (Zwolle, NL). This hybrid resin system cures in two steps which can be set to occur at different temperature levels by means of appropriate catalyst selection. The first reaction step is a urethane polyaddition reaction, consisting of chain polymerization between isocyanate molecules and hydroxyl functional groups present in the resin backbone chains, similar to UP/VE prepolymers. The initially liquid resin goes through a gel state to a B-stage condition, in which the material is not tacky but still flexible (rubber-like consistency). This reaction step takes place already at room temperature, or in a pultrusion die controlled at temperatures between 80°C and 100°C. By increasing the temperature above 100°C a radical polymerization is initiated, leading to full curing of the matrix. This

second reaction step consists of cross-linking between the polymer chains and polystyrene. The application of such a two-step mechanism allows the combination of different processing techniques, for example to produce parts of more complex geometries than possible by pultrusion only [1].

3.1.4 Fiber reinforcements

Pultruded profiles are primarily reinforced in the longitudinal profile orientation by fiber rovings. Most common fiber types are glass and carbon, while niche applications with aramid and basalt are also known. Glass fiber direct rovings, mostly of the E-Glass type, are by far the most widespread reinforcement type used in the pultrusion industry, due to its very good price-performance ratio and electrical insulation properties. Carbon fiber rovings or tows are used for products where the application demands higher mechanical performance and higher weight savings, e.g. for automotive parts. While design constraints have hindered development of pultruded parts for the automotive industry, the cost effectiveness and the automation potential makes the process highly interesting for this market, which may introduce a shift in design concepts in the medium/long term.

One of the most important factors affecting the mechanical performance of a composite part is the bonding between fiber and matrix. This is achieved by the application of a sizing agent compatible to the matrix, which is uniformly spread over the surface of the individual filaments. While applied sizing chemistry is a largely proprietary technology undisclosed by fiber manufacturers, fiber types with standard sizing (silane based sizings in glass fibers and epoxy or polyurethane based sizings in carbon fibers) available on the market are known to form good bonding to typical resin systems used in pultrusion.

Processability is an important aspect for a successful pultrusion production, glass fibers being in general much easier to process than carbon fibers. Due to its more brittle nature, carbon fiber filaments can easily detach from the fiber bundle, and deposit at various contact regions of the processing line, for example in the resin bath or in the preforming assembly. Therefore, guiding elements in preforming assemblies used for processing of glass fibers can be manufactured from low priced materials (e.g. polyethylene), while care must be taken when processing carbon fibers; in the latter case, ceramic elements or metal with a polished contact surface are preferred over roughly finished parts.

3.2 Resin chemorheological characterization

The evaluation and prediction of resin properties as it goes through the curing process is crucial for defining processing conditions. Chemorheology is a term commonly found in literature to describe the physical changes occurring to a thermoset resin while curing, i.e. going from liquid state through gelation to solid state (infinite three-dimensional network polymer), in correlation with reaction kinetics and energetics. The resin viscosity in an initial unpolymerized or prepolymerized state changes as the matrix cures along the processing route, i.e. as a function of temperature and time. Temperature in the resin is influenced by release of energy from the exothermic polymerization reaction. The interaction of these processes is therefore of paramount importance to a better process understanding and for process simulation. A Time-Temperature-Transformation (TTT) diagram is useful to understand the cure behavior and physical properties of thermosets (Figure 3.5) [15].

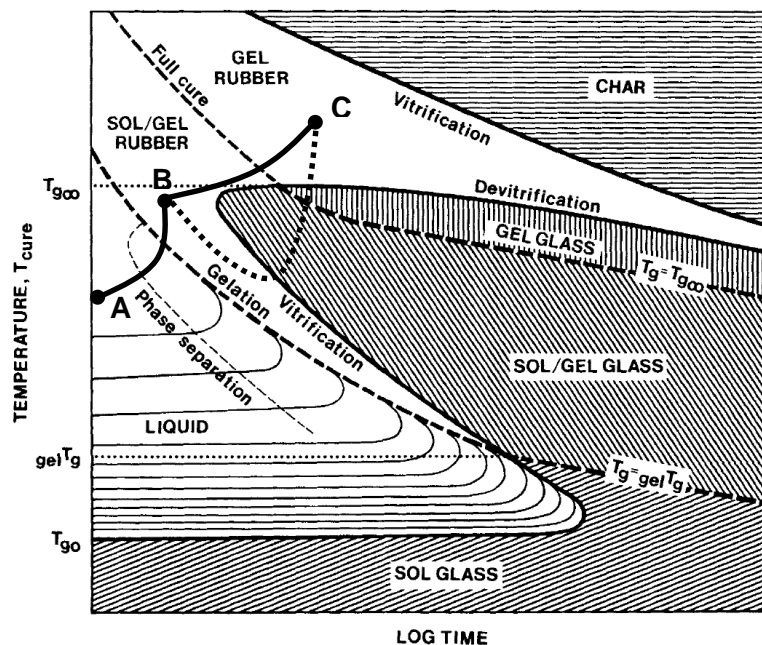


Figure 3.5: Schematic Time-temperature-transformation (TTT) diagram, adapted from [15]

By following a temperature and time path applicable to a processing method, one can ascertain the physical states the material goes through during the curing reaction. Particularly interesting in the case of the Daron resin focused on these studies is the correlation of the technological terms A-, B- and C-stages to the liquid, sol/gel, and gel states respectively. Accordingly, during the first curing step, the resin goes from liquid (A-stage) to a rubbery state (B-stage), represented by the line A-B in Figure 3.5. The resin goes through gelation, either at room temperature or by an increased temperature. By further increasing the temperature, the resin goes over the full curing line, reaching a rubber or glass state

depending on temperature being above or below the glass transition. The “gel rubber” in this case is however actually a highly cross-linked polymer network with some molecular movement of chain segments at a temperature above glass transition. Depending on processing history, the C-stage can be reached by one of the two lines connecting B and C, i.e. directly from a flexible B-stage (continuous line) or through a vitrified intermediate network (dotted line). It is expected that the processing history will have a significant impact on the final network morphology and thus on materials properties.

3.2.1 Reaction kinetics

Several empirical and some mechanistic models have been proposed to describe the dependence of the degree of cure α on time and temperature for different thermoset resins. Empirical models are generally simpler, assuming a global reaction order and providing no information on different reaction mechanisms which might occur concurrently during curing. Mechanistic models require characterization of the concentration of reactants, intermediates and products, which may be measured for example by means of FTIR. Reviews of applied methods and conducted studies were presented in [16] and [17]. Focus will be given here to empirical kinetic models which were derived for the resin systems applied to pultrusion and/or directly applied in pultrusion simulations. Most of these models are based on an autocatalytic model firstly proposed by Kamal and Sourour [18] and Kamal [19], which will be referred to as Kamal-Sourour model. This model has been shown to describe adequately the cure kinetics of both epoxy and unsaturated polyester systems:

$$\frac{d\alpha}{dt} = (k_1 + k_2\alpha^m)(1 - \alpha)^n \quad \text{Equation 3.1}$$

with

$$k_i = A_i \exp\left(\frac{-E_i}{RT}\right) \quad \text{Equation 3.2}$$

where k_i are Arrhenius terms with a corresponding pre-exponential factor A_i and activation energy E_i . The most widely used characterization method to obtain kinetic data is the Differential Scanning Calorimetry (DSC). For fitting of kinetic data, the degree of cure α at a certain time t is assumed to be directly proportional to the amount of heat released by the reaction up to time t (H_t) relatively to the total heat of reaction (H_R) [20].

$$H_t = \int_0^t \left(\frac{dQ}{dt}\right) dt \quad \text{Equation 3.3}$$

$$\alpha = \frac{H_t}{H_R} \quad \text{Equation 3.4}$$

$$\frac{d\alpha}{dt} = \frac{1}{H_R} \frac{dQ}{dt} \quad \text{Equation 3.5}$$

where (dQ/dt) is the heat flow directly measured by DSC. Kinetic data suitable for fitting of an empirical model such as shown in Equation 3.1 can be obtained by a series of isothermal or dynamic scans. While isothermal scans allow a more straightforward regression of data, insufficient accuracy in the initial section of the measurement is recognized as an issue for high temperature isotherms, since a significant heat might not be detected before thermal equilibrium is reached. It is therefore generally considered that dynamic DSC scans are more adequate to fit empirical kinetic models [16]. Methods to fit a series of dynamic scan data include the ASTM E698 standard for the regression of simple single reaction models, and the methods of Friedman [21] and Ozawa-Flynn-Wall [22] for more complex reactions better fitted with multistep models.

A number of studies on pultrusion modeling and simulation also included a kinetic model to predict degree of cure and temperature evolution along the pultrusion die. A list of models used in the different studies is shown in Table 3.1.

Price [23] and Aylward et al [24] were the first to include a reaction model to a numerical solution of the energy equation applied to a pultrusion model. They considered a simple 1st order reaction model with an Arrhenius term. Batch and Macosko [25] implemented a more complex mechanistic model including free radical initiation, chain propagation and radical inhibition mechanisms. They argue that such a model has the advantages of accounting for the concentrations of initiator and inhibitor on the resin formulation, as well as incomplete cure due to vitrification and diffusion-limited propagation. Han et al [26], Kim et al [27] as well as the research group from Prof. Lee at the Ohio State University (OSU) choose to use the Kamal-Sourour model. Other researchers used the well described kinetic parameters for an epoxy system derived by Lee et al. [20]. Prof. Vaughan's research group at the University of Mississippi (Ole Miss) has published many articles on pultrusion models, most of them including a nth order reaction model.

Table 3.1: Summary of kinetic models used in pultrusion studies

Model type	Equation(s) *	Resin system	References
First order	$d\alpha/dt = k(1 - \alpha)$	EP	[23] [24] [28]
Autocatalytic Kamal-Sourour	$d\alpha/dt = (k_1 + k_2\alpha^m)(1 - \alpha)^n$	UP, EP UP VE	[26] [27] [29] [30] [10] [31] [32] [33]
Autocatalytic + First order	$d\alpha/dt = (k_1 + k_2\alpha)(1 - \alpha)(B - \alpha), \alpha \leq 0,3$ $d\alpha/dt = k_3(1 - \alpha), \alpha > 0,3$	EP	[20] [34] [35] [36]
Mechanistic	See [25], p. 1231-1232 See [37], p. 1098-1099	UP UP	[25] [37] [38] [39]
n th order	$d\alpha/dt = k(1 - \alpha)^n$	EP	[40] [41] [42] [43] [44] [45] [46] [47] [48] [49] [50] [51]
Modified Kamal-Sourour	$d\alpha/dt = (k/\alpha_{max})\alpha^m(\alpha_{max} - \alpha)^n$	VE	[52] [53]

* k and k_i are Arrhenius terms in all equations.

3.2.2 Chemorheology

The derivation of a viscosity function in terms of time and temperature is also useful for process simulation, since one is concerned with the processing window in which the resin is flowable or at an optimum flowing state of low viscosity. The viscosity can be obtained from various measuring methods, a comprehensive list and discussion of different methods was presented in [16].

For thermosetting resins of initially relatively low viscosity and curing to an infinite three-dimensional polymer network, the disc-plate rheometer in oscillation mode is a viable measuring technique. By this method, the initially liquid resin formulation is placed between the static bottom plate of the rheometer and a moving disc. Depending on the fluid and the current physical state being measured, the disc can be made to rotate or oscillate with a very small amplitude, which may also be reduced as the viscosity increases in order to maintain a constant level of applied torque.

One of the limitations of this method is that non-newtonian behavior is difficult to quantify. Since the reaction takes place relatively fast, a frequency sweep over a large range of orders of magnitude cannot usually be performed for the material at a certain cure state, i.e. the material will change its physical state while the measurement in different frequencies takes place.

Non-newtonian behavior is however frequently observed in thermosetting resins. The modelling of viscosity as a function of temperature and degree of cure shall therefore be regarded as an approximation for the flowability assuming the material is being subject to shear rates of the same magnitude as set in the rheometer measurements.

Rheology measurements in oscillation mode can be used to evaluate flow behavior as the resin goes from liquid resin to cured matrix. In this type of measurement, a shear strain or stress sinusoidal function is applied to the oscillating upper disc, and the system response is measured. A viscoelastic material responds to the applied strain or stress function with a time lag. A predefined shear strain function may be applied, according to the following equation [54]:

$$\gamma(t) = \gamma_A \cdot \sin(\omega t) \quad \text{Equation 3.6}$$

Where γ_A is the strain amplitude and ω is the angular frequency in [rad/s]. The shear stress function is then defined as:

$$\tau(t) = \tau_A \cdot \sin(\omega t + \delta) \quad \text{Equation 3.7}$$

Where δ is the phase lag in [rad]. For viscoelastic materials, the phase lag will always be a value between 0° and 90° ($0 < \delta < \pi/2$ rad). An ideally elastic material responds without phase lag ($\delta = 0^\circ$) and an ideally viscous fluid with 90° phase lag. From these values, a complex shear modulus G^* can be calculated as:

$$G^* = G' + iG'' \quad \text{Equation 3.8}$$

$$G' = \frac{\tau_A}{\gamma_A} \cos \delta \quad \text{Equation 3.9}$$

$$G'' = \frac{\tau_A}{\gamma_A} \sin \delta \quad \text{Equation 3.10}$$

The complex shear modulus is composed of a storage modulus G' representing the elastic response of the material, and a loss modulus G'' representing the viscous response. G' is a measure of the stored energy during the shear process. G'' is on the other hand a measure of the energy lost during the same deformation process. The value $\tan \delta = G''/G'$ is called the loss or damping factor. From these values, the reciprocal contributions to the complex viscosity η^* can be calculated [55]:

$$\eta' = G''/\omega \quad \text{Equation 3.11}$$

$$\eta'' = G'/\omega \quad \text{Equation 3.12}$$

$$\eta^* = \eta' + i\eta'' \quad \text{Equation 3.13}$$

$$|\eta^*| = \sqrt{\eta'^2 + \eta''^2} \quad \text{Equation 3.14}$$

ω is the applied angular frequency in rad/s. According to the Cox-Merz rule, the modulus of the complex viscosity $|\eta^*|$ agrees relatively well with the apparent viscosity of viscoelastic materials for low shear rates [56].

Gelation is defined as the initial formation of an infinite molecular network. From this point on, the material will present a macroscopic elastic behavior, and be composed of fractions of the network (gel) and sol. The further reaction is normally diffusion-rate limited. Gelation occurs at a definite degree of cure for a given resin system [15]. A number of methods and standards have been proposed for the direct measurement of gel time, although most of these tests are intended as simple quality control checks [16]. A number of studies have evaluated the gel point by rheology measurements in oscillation mode, as the time when the storage and loss moduli cross each other. Winter [57] discussed the limits of validity of this crossover method. The standard ASTM D4473 [58] describes a cross-over point analysis for isothermal rheology measurements. According to Mezger [54], it makes little sense to refer to viscosity of the material after the crossing of the gel point. When $G' > G''$, the matrix behaves effectively as a gel without any discernible flow behavior.

A viscosity model can be obtained by fitting of viscosity curves from isothermal or dynamic experiments, in an analogous way as kinetic models from DSC measurements. A list of several proposed models is also presented in [16]. The model was used to fit experimental data in a study by Lee et al [20], and was subsequently applied in most studies related to

pultrusion [27] [30] [32] [35] [36]. In this model, which will be referred to as Lee model, the time variable is replaced by the degree of cure to a viscosity equation of the following form:

$$\eta = \eta_{\infty} \exp\left(\frac{E_{\eta}}{RT} + B\alpha\right) \quad \text{Equation 3.15}$$

where η_{∞} , E_{η} and B are empirical constants. Blaurock [29] used a step function by which the viscosity before gelation is a function of temperature only and goes to infinity upon gelation. Moschiar [39] used yet another model which accounted for gelation effects.

Castro and Macosko proposed another model suitable for representing the viscosity evolution of mixing-activated polyurethane resins [59] [60].

$$\eta = \eta_{\infty} \exp\left(\frac{E_{\eta}}{RT}\right) \cdot \left(\frac{\alpha_g}{\alpha_g - \alpha}\right)^{A+B\alpha} \quad \text{Equation 3.16}$$

where α_g is the degree of cure at the gel point. Four empirical constants must be fitted (η_{∞} , E_{η} , A and B) in this model. The degree of cure at gelation varies strongly according to the type of resin. Moschiar and Blaurock reported a gel point at very low conversions (0.017 – 0.04) for unsaturated polyester resins, while Castro and Macosko estimated the gel point at 0.65 – 0.85 conversion for the polyurethane formulations studied.

3.3 Reinforcement characterization

Fiber stacks for pultrusion are usually composed of roving and continuous filament mat (CFM) layers, lately so called complex reinforcements (composed of a combination of chopped strand mat and/or surface veil and woven or non-crimp fabric layers) have also become attractive depending on the application, as they have the potential to improve mechanical properties in directions other than the profile main axis of orientation.

In RTM, planar reinforcements are usually cut according to the part shape being molded and laid into the mold before closing and injecting the resin. These reinforcements are frequently bound together, e.g. by means of powder binders or yarns, in order to attain some degree of form stability. The pultrusion process, on the other hand, is characterized by the use of a multilayered laminate structure composed of roving layers aligned in the profile longitudinal direction and planar reinforcements. As a consequence of this laminate structure, it is important to precisely position the rovings in order to achieve a uniform fiber distribution

across the layer, i.e. avoiding resin-rich regions and other regions with very high fiber volume content. Positioning is usually achieved by means of threading the rovings through guiding plates with hole patterns specific to the profile cross section being produced.

3.3.1 Compressibility

The importance of assessing the compressibility of fiber reinforcements becomes apparent when one is concerned with a part design composed of layers of different reinforcement materials. In order to define a stack structure and/or a processing window, the compressibility of each of the fiber reinforcements must be known (i.e. the fiber volume content as a function of compaction pressure). Specifically, for the pultrusion process, one needs to estimate the number of rovings which are needed to fill a given cross section, according to the compaction pressure and the number and type of planar reinforcements defined for the profile.

Gutowski et al [61] analyzed the compressibility and permeability of a carbon fiber stack impregnated with oil. The model described by Equation 3.17 was proposed for the transversal stiffness of the fiber stack. The material behavior was reported to be well fitted by the model.

$$p_z = \frac{3\pi B}{\beta^4} \frac{\sqrt{\frac{V_f}{V_0}} - 1}{\left(\sqrt{\frac{V_a}{V_f}} - 1\right)^4} \quad \text{Equation 3.17}$$

where p_z is the stress or pressure applied in the direction transverse to the laminate plane. B is the bending stiffness of the fiber. β is a constant representing the span length to span height ratio for the fiber network, i.e. it represents the scale of fiber waviness for the simple case of a unidirectional laminate, V_a is the maximum possible fiber volume fraction which is usually between the limits for a square (0.785) and a hexagonal packing (0.907).

Kim et al [62] studied the compression and relaxation behavior of different dry reinforcement stacks, among them aligned roving stacks and random mats typically used in pultrusion. Unidirectional stack samples were prepared by winding one roving over a thin rectangular steel plate while keeping each new winding parallel to the previous one. The edge was then cut and the sample laid flat. A stack of 20 – 40 layers was then positioned to a rectangular testing fixture and compressed with linear displacement up to 8.6 MPa. Very similar

characteristic curves of pressure vs. fiber volume fraction for glass and carbon fiber rovings were observed.

Batch et al. [63] noted that the combination of different reinforcements to a single layup generally leads to a higher volume fraction for a given pressure than predicted from the volume fractions of the individual layers. This is caused by interactions of layers intertwining between each other by a so called nesting effect. They evaluated the force needed to compact a roving layer indirectly by pulling roving bundles through a tube and measuring the needed pulling force and assuming a certain friction coefficient.

3.3.2 Permeability

The concept of permeability of a porous media related to the resistance against fluid flow originated from geology and hydrology research, an empirical approach being proposed by Henry Darcy for the pressure driven flow through beds of sand considered as an isotropic permeable medium [64].

$$\mathbf{v} = -\frac{K}{\eta} \nabla P \quad \text{Equation 3.18}$$

where \mathbf{v} is the flow velocity, K the permeability of the porous medium, η the fluid viscosity and ∇P is the pressure gradient. The experimentally derived Darcy's law was later also derived theoretically from the fundamental equations of motion for Stokes flow by Whitaker [65], i.e. flow in very low Reynolds number regions, where viscous forces are larger than advective forces [66]. It has been widely adopted in the composites field to describe fluid flow through the fiber reinforcement, which is in its most general form considered an anisotropic medium. In this case the permeability turns to a symmetric tensor of second order. If one chooses a Cartesian coordinate system aligned to the principal orientations of the reinforcing material, i.e. 1 being the fiber orientation, 2 the transverse in-plane and 3 the out-of-plane direction, one can fully describe the permeability in terms of three principal permeabilities K_1 , K_2 and K_3 [67].

The permeability of fiber reinforcements is an important material parameter for fluid flow simulation and the purpose of better process understanding. The determination of the permeability is a widespread characterization technique of reinforcement materials for liquid composite molding (LCM) processes, e.g. resin transfer molding (RTM). There is a range of methods for determining permeability, depending on whether one is concerned with the permeability parameter in the planar or in the transverse orientation. For in-plane

permeability, experimental techniques can be divided into linear and radial flow, each one having intrinsic advantages and disadvantages. Furthermore, the permeability can be obtained from unsaturated or saturated flow. In unsaturated flow, a liquid is injected through the reinforcement while the flow front position vs. time is recorded. In saturated state, liquid constantly flows through the already wetted-out reinforcement, the permeability being determined from the absolute pressures at different positions and the volumetric flow rate. A straightforward analytical solution is available for data regression from the linear flow measurement. For the radial flow method, analytical solutions were proposed for obtaining the permeability parameters from direct observation of the flow front in the main axes at different times [67] [68] or from the times where the flow front reaches defined points in the flow region [69] [70]. It must be noted that for these analytical solutions to be valid, unhindered elliptical flow front must develop, where atmospheric pressure is assumed at the flow front perimeter. For saturated flow, an analytical solution from pressure data at different points in the flow region was also proposed by Han et al. [71]. In this case the solution can only be derived for a circular saturated flow region. For complex preform or cavity geometries, a numerical method can be applied to find the length- and crosswise permeability parameters [72].

Recent round-robin studies have concluded that the evaluation of the permeability is extremely dependent on the method and conditions. Permeability measurements on a specific carbon fiber fabric by different institutions presented scattering of the results of about one order of magnitude [64]. By strictly defining the testing technique and conditions such as fiber volume content, fluid type, viscosity and injection pressure, scattering was reduced to $\pm 20\%$ [73].

Of major interest to pultrusion is the permeability of a highly anisotropic fiber stack composed of unidirectional tows. Many researches have made attempts to model and/or experimentally determine the permeabilities in longitudinal and transverse direction to the tow orientation, some of which will be reviewed in this work.

A widely used model for estimating the permeability is the so called Kozeny-Carman equation, which was originally derived for granular beds of ellipsoid material, and has been assumed to be valid for fibrous porous media [74].

$$K = \frac{R^2 (1 - V_f)^3}{4k_c V_f^2} \quad \text{Equation 3.19}$$

where k_c is the Kozeny constant, R the particle radius and V_f the fiber volume fraction. Anisotropy is accounted for by using different values for the Kozeny constant which must be experimentally determined. Gebart [74] proposed a modification for the transverse equation to account for the fact that transverse flow effectively ceases upon reaching a theoretical maximum V_f when the fibers touch each other. Further, analytical models for predicting the permeabilities in both directions were derived. In longitudinal direction the derivation leads to an equation with a shape factor directly correlated to the Kozeny constant, while for transversal direction the following equation was proposed:

$$K_{\perp} = C_1 \left(\sqrt{\frac{V_{fmax}}{V_f}} - 1 \right)^{5/2} R^2 \quad \text{Equation 3.20}$$

where the parameters C_1 and V_{fmax} depend on the arrangement of fibers (quadratic or hexagonal). The analytical results were further supported by experiments in channel flow onto a non-crimp fabric (NCF). Results were found to agree with the model when the fiber radius in the equation is adjusted to an “effective fiber diameter”, which is about 4 times larger than the actual diameter. It was also observed that the experimental results for the permeability parameter were higher than published in previous papers, which was related to the fiber architecture (fiber tows in NCF fabric knitted together, leaving relatively large channels between them).

Westhuizen and Du Plessis [75] also derived a model for predicting flow parallel and perpendicular to fiber orientation. The model was compared to experimental results from other studies. It is interesting to note that in a technical paper [76] explaining aspects of Gauchel's patent [7], reference is made to the model of Westhuizen and Du Plessis. The authors argue that the effect of compaction on permeability is more pronounced in the longitudinal than in the transverse direction, that is the K_1 approaches K_2 as the fiber volume ratio increases. Actually this is not the case, as the difference remains at one order of magnitude and the degree of anisotropy represented by the ratio (K_1/K_2) even increases with increasing volume content, in the region of V_f considered. This becomes clear when changing the y axis on the graph to a logarithmic scale. Figure 3.6 (a) shows the graph as presented in [76], while in (b) the models of Gebart [74] and Westhuizen and Du Plessis (W&P) [75] are plotted together in logarithmic scale.

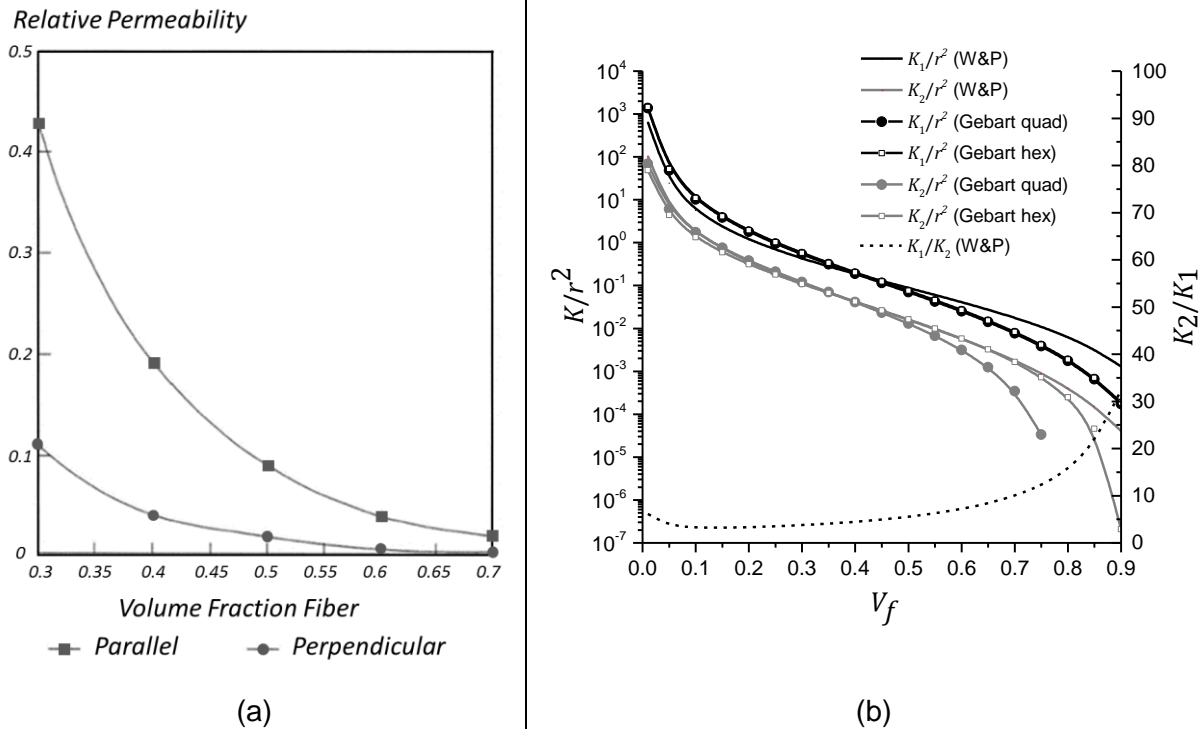


Figure 3.6: Curves of permeability of a unidirectional fiber stack in longitudinal and transverse direction: (a) as presented in [76]; (b) Comparison of W&P and Gebart models

A comparison between the curves reveals that the models diverge from each other in the range of fiber volume contents of rovings in pultrusion, which is typically between 0.5 and 0.7. Both models predict a difference of about one order of magnitude between K_1 and K_2 for this range of V_f .

Blaurock [29] measured the permeability in the longitudinal direction only for different fiber volume fractions. The testing assembly allows the fibers to be stretched on the edges. A Kozeny-Carman constant was fitted to the results. Ding et al. [10] used a similar approach as Blaurock, but the rovings were cut to a defined length and placed into a channel flow type testing assembly, i.e. they are not stretched. Measurements were also only performed in the longitudinal direction. Values for the transversal permeability were estimated from the model of Westhuizen and Du Plessis [75].

Bates et al. [77] measured only the transverse permeability with an out-of-plane experimental assembly. No detailed information is given about how the rovings are placed and/or stretched inside the mold. Scattering of the void fractions for a certain applied compressive stress suggests that this assembly might be highly sensitive to the laying of fibers in the mold.

Schell et al [78] determined experimentally the permeabilities in both longitudinal and transverse orientations for glass fiber bundles stretched by winding them around a frame which is then placed inside the permeability measurement cell. The cell measures by a linear technique, i.e. separate measures for longitudinal and transverse permeabilities are needed. Measurements are reported for fiber volume contents of 40% and 64%. (K_1/K_2) amounted to 4.9 and 2.2 for these fiber volume contents respectively.

3.4 Modelling and simulation

As any physical process, the composite processing can be modelled by the fundamental laws of conservation of mass, momentum and heat transfer. Specifically, in pultrusion, these fundamental governing equations, generally with simplifications according to the aspects being studied, are the basis for the numerical solution. Depending on the derivation approach, one can obtain the equations in integral (control volume approach) or differential (infinitesimal volume approach) form. Regarding the framework of analysis, one can derive the equations for a stationary volume element in space, leading to equations in the so called Eulerian framework or for a volume element travelling in space, obtaining equations in the Lagrangian framework. The equations that result from both frameworks are completely equivalent and can be also derived from one another. Anderson [79] pointed out that in some cases, in flows with very high speeds (especially when discontinuities are involved, for example in shock waves), a numerical scheme based on the integral form might be preferable due to results with better precision. In the following discussion, the differential form of the equations will be presented, as these are applied for the finite volume solution method implemented by the CFD code employed.

The continuity equation describes the conservation of mass in a system:

$$\frac{\partial \rho}{\partial t} + \nabla \cdot (\rho \mathbf{v}) = 0 \quad \text{Equation 3.21}$$

The momentum equation states that the rate of change of momentum in a fluid particle equals the sum of forces acting upon it. It is written in its most general form as:

$$\frac{\partial(\rho \mathbf{v})}{\partial t} + \nabla \cdot (\rho \mathbf{v} \otimes \mathbf{v}) = -\nabla P + \nabla \cdot \boldsymbol{\tau} + S_M \quad \text{Equation 3.22}$$

Where ρ is the density, \mathbf{v} is the velocity vector, $\boldsymbol{\tau}$ is the stress tensor and S_M is a source term of body forces acting from a distance, e.g. gravitational forces. Taking a Cartesian coordinate system, Equation 3.22 reduces, for example, for the x component:

$$\frac{\partial(\rho v_x)}{\partial t} + \nabla \cdot (\rho v_x \mathbf{v}) = -\frac{\partial P}{\partial x} + \frac{\partial \tau_{xx}}{\partial x} + \frac{\partial \tau_{yx}}{\partial y} + \frac{\partial \tau_{zx}}{\partial z} + \rho f_x \quad \text{Equation 3.23}$$

The governing flow regime in pultrusion can be considered as a Stokes or creeping flow, due to the relatively high viscosities involved and the short length scale of flow given by the porous medium.

The energy conservation equation is given by:

$$\frac{\partial(\rho H)}{\partial t} = -\nabla \cdot (\rho \mathbf{v} H) + \nabla \cdot (\lambda \nabla T) + \boldsymbol{\tau} : \nabla \mathbf{v} + S_E \quad \text{Equation 3.24}$$

where the energy is considered in terms of enthalpy H . λ is the thermal conductivity. This so called thermal energy equation is obtained from the more general total energy equation by neglecting the kinetic energy term (which is a reasonable assumption for low speed flows) and variable density effects (appropriate for liquids) [66]. For steady state flow regimes of low speed, i.e. with negligible viscous dissipation, Patankar [80] proposed further simplification of Equation 3.24 to:

$$\nabla \cdot (\rho \mathbf{v} H) = \nabla \cdot (\lambda \nabla T) + S_E \quad \text{Equation 3.25}$$

The energy source corresponds to the rate of heat generated by the exothermic reaction, and can be expressed as:

$$S_E = (1 - V_f)\rho H_R \frac{d\alpha}{dt} \quad \text{Equation 3.26}$$

The method proposed by Patankar for discretization and numerical solution has been widely used for solving pultrusion-related models. His method and other solving techniques will be briefly presented in the next section.

3.4.1 Numerical solving techniques

In a numerical procedure, one is concerned with finding the values of unknown variables at specific locations (grid points or nodes) within a calculation domain (which may be assumed, for example, as a two-dimensional area space or three-dimensional volume). For calculating the unknown variable in a grid point adjacent to another at which the variable value is known, one recurs to a simplified form of the related differential equation (e.g. Equation 3.26), called the discretization equation. In subdividing the domain into sufficiently small elements with associated grid points, the discretization equations can be chosen as simple algebraic equations.

Discretization methods have been traditionally divided into finite difference (FDM), finite element (FEM) and finite volume (FVM). Patankar noted, however, that a strict separation among methods might not be useful, and that his own developed methods have the appearance of finite difference formulations but incorporate ideas of the FE method [80]. All the three methods have been used for solving CFD problems. Much of recent research has focused on the application of unstructured grids to discretize complex domain geometries.

A particular advantage of commercial CFD software such as Ansys CFX over self-written code is the possibility of studying more complex geometries, and the higher flexibility in creating unstructured meshes for these geometries, without the burden of setting up algorithms able to properly solve the conservation equations over the discretized domain. ANSYS CFX uses an element-based finite volume method. The discretization and subsequent calculation is done over control volumes, defined from groups of mesh elements. The mesh elements are always three-dimensional in FVM; for simplicity however, the concept of the control volume is shown in Figure 3.7 in two-dimensional form [81].

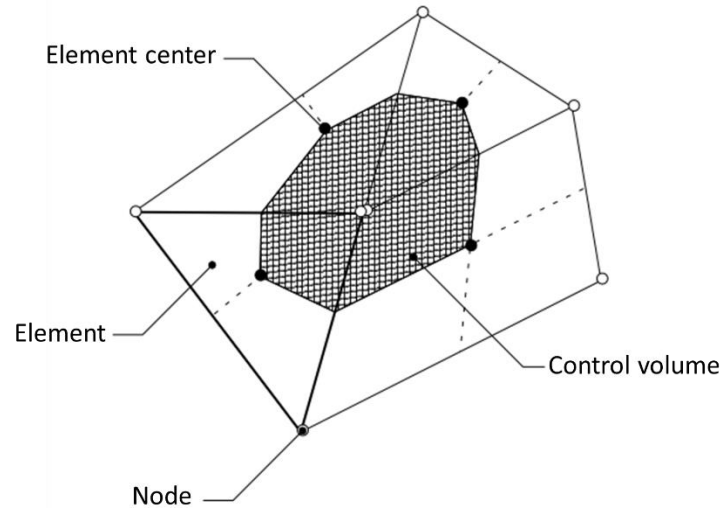


Figure 3.7: Representation of control volume formed by adjacent mesh elements [81]

All solution variables are stored at the nodes (mesh vertices). A control volume (the shaded area) is constructed around each mesh. By the FVM, the conservation equations of mass, momentum and energy described in the previous section are integrated over each control volume, generating volume (representing source terms) and surface (representing fluxes) integrals. These volume and surface integrals are then discretized to algebraic form, which are then solved for each control volume. The results for each control volume are then compared and balanced to the adjacent control volumes and/or boundary conditions by means of an iterative procedure, until a desired residual coefficient (representing an average of solution mismatches between control volumes) is reached.

3.4.2 Modelling and simulation of the pultrusion die

Since the pioneering work from Price [23], a number of researchers have dealt with the topic of modelling and simulating the pultrusion process. Different aspects and/or physical processes have been primarily considered in the studies, which can be assigned to one of the following categories:

- Thermo-chemical modelling
- Fluid dynamics modelling
- Thermo-mechanical modelling

The modelling and simulation strategy is strongly dependent on the main physical process being investigated. To define the physical process(es) relevant to the investigation, it is useful to examine a schematic representation of the pultrusion die and the phase changes occurring within it, such as presented by Starr [4]:

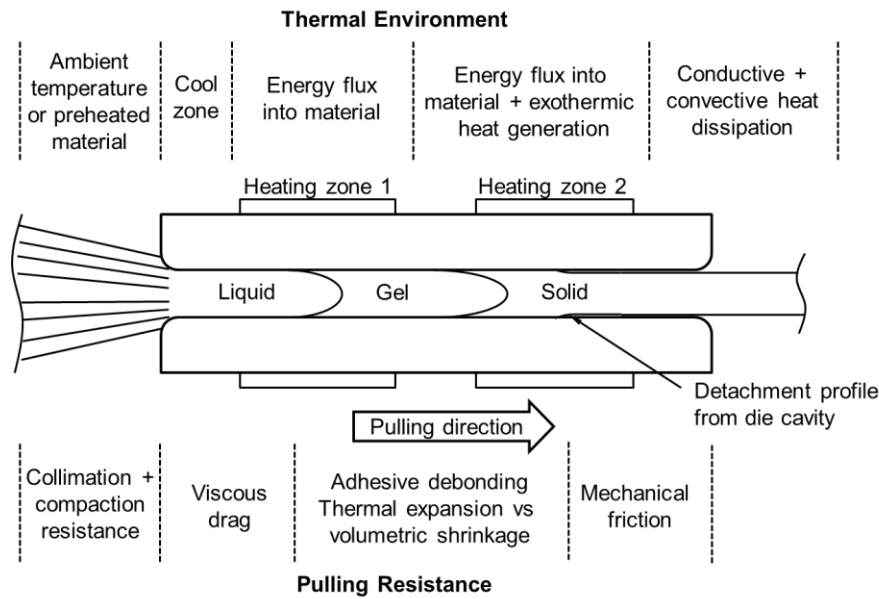


Figure 3.8: Schematic representation of pultrusion die including resin phase changes, thermal effects and effects related to pulling resistance, adapted from [4]

3.4.2.1 Thermo-chemical modelling

Price [23], Aylward et al [24] and Batch and Macosko [25] were primarily concerned with the thermo-chemical modelling, i.e. the prediction of evolution of degree of cure and heat generation due to the exothermic reaction along the die. They assumed a plug flow in which the resin travels with the same speed as the pulling speed of the fiber stack. Batch and Macosko argued that the assumption of plug flow is valid because the resin layer between fibers and die wall is very thin (1 – 10 μm), therefore the volume of drag-induced flow is negligible. In [24], the open source algorithm Finite Element Analysis Program (FEAP) was applied, and in [25], a finite difference scheme with an implicit time step solution by the Crank-Nicolson method was used. In both studies, the model was considered for a Lagrangian framework, i.e. the model consists of a thin slice of material advancing along the die as the time steps advance (see Figure 3.9 (a)). For each time step increase, the solving system calculates the new material state, e.g. for the energy balance, the exothermic heat evolution, degree of cure and temperature are obtained.

The numerical solution of the energy balance can be validated by a relatively straightforward technique of feeding a wire thermocouple within the fibers. In this way, the material temperature can be measured at different positions within the profile cross section and along the die length. It is a common feature of the exothermic reaction that the material will reach a exothermic peak temperature above the die set temperature; in this region the die metal volume will effectively act as a “heat sink” [4].

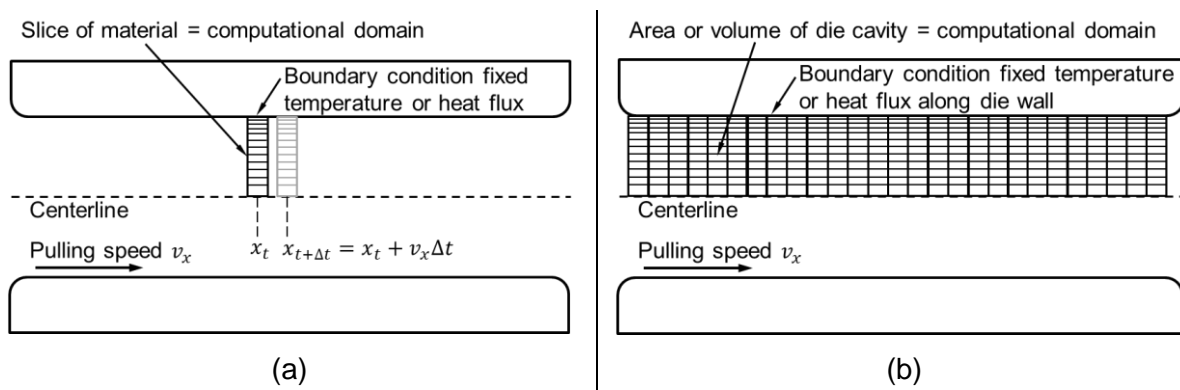


Figure 3.9: Discretization models of a pultrusion die. (a) Lagrangian framework with moving slice of material along the die length; (b) Eulerian framework with die cavity discretized into elements fixed in space

The majority of subsequent studies have applied a Eulerian framework, such as depicted in Figure 3.9 (b). One reason for this has certainly been the advances in computational capabilities, allowing even models with several thousands of nodes to run in personal computers. While both models might deliver similar results in respect of the thermo-chemical modelling, a transient approach has clear limitations if one is concerned with the fluid dynamics. Even if there are available methods for the linearization of the continuity and momentum equations in non-conservation form, a modelling approach such as in Figure 3.9 (a) will fail to catch any long range effect on the flow balances, for example, a boundary condition is not defined for the outlet in this case. This means that the iteration procedure becomes more complicated, counterbalancing the simplicity of the computational domain. Another drawback of the transient method is the limitation of die geometry to a constant cross section, thus preventing it to be used for studying geometric features such as a tapering of the die inlet or an injection chamber.

3.4.2.2 Fluid dynamics modelling

In fluid dynamics modelling, one is concerned with pressure and velocity fields of the liquid resin, i.e. the inlet and the straight cross section located immediately after the inlet. As a general rule, the die cavity is represented by a homogeneous porous domain through which the liquid resin permeates by pressure driven flow and at the same time is pulled along with the reinforcement (advection term). Considering a simplified 2D case of a profile being pulled through a pultrusion die like the one depicted in Figure 3.9 at constant pulling speed U , i.e. at steady state, the continuity equation (Equation 3.21) reduces to:

$$\frac{\partial(\phi v_x)}{\partial x} + \frac{\partial(\phi v_y)}{\partial y} = 0 \quad \text{Equation 3.27}$$

where ϕ is the porosity of the reinforcement stack. The momentum equations (Equation 3.22) in the pulling direction (x) and out-of-plane direction (z) simplify to:

$$v_x = U - \frac{K_1}{\eta\phi} \frac{\partial P}{\partial x} \quad \text{Equation 3.28}$$

$$v_z = -\frac{K_2}{\eta\phi} \frac{\partial P}{\partial z} \quad \text{Equation 3.29}$$

The research group at Ole Miss has done extensive work on this topic. The effect of processing parameters such as pulling speed, porosity and viscosity on the resin pressure rise was investigated in [82], [83], [84] and [85], while the effect on pressure of different inlet geometries, such as a radius, parabolic and conical tapering angle at the entrance was discussed in [85] [84] [86]. An interesting aspect of their experimental method was the measurement of pressure within the pultruded material; in an analogous method to the wire thermocouple, a fiber optic pressure probe was fed to the reinforcement fiber stack. Although the probe has a relatively large diameter (0.8 mm, die cavity thickness 3.18 mm) which might arguably produce a local disturbance in the flow, the authors presented a good agreement between predicted and measured pressure data. More recently, the research group has published studies dealing with closed injection pultrusion, which will be discussed in detail in section 3.4.3.

The pressure is usually the most important variable for practical purposes. It is generally accepted that the pressure increase arising from compaction of the fiber stack soaked with resin is the main drive for void reduction; the entrapped air can exit at the die inlet through backflow more easily than the resin, and this is a pressure-driven Darcy's flow. Another important aspect is the contribution of fluid resin pressure on the pulling force, which is arguably the most important experimental variable for process monitoring. Models proposed for the pulling force are discussed in section 3.4.2.4.

Some researchers have proposed analytical models for the pressure inside the pultrusion die. Kim et al [27] proposed an analytical model for pressure by assuming unidirectional flow in the pulling direction, justified by the permeability in transverse direction being much lower than in the longitudinal one. They derived a solution for the pressure gradient along the inlet portion:

$$\frac{dP}{dx} = \frac{U\eta}{K(x)} \left[1 - V_{fx} - \left(1 - \frac{\Delta v}{v} \right) \left(\frac{V_{fx}}{V_f} - V_f(x) \right) \right] \quad \text{Equation 3.30}$$

where U is the pulling speed, $K(x)$ is the longitudinal permeability, and V_{fx} is the fiber volume fraction as functions of axial distance. $\Delta v/v$ represents the resin volume change, given by the sum of thermal expansion and shrinkage due to curing effects:

$$\Delta v/v = \alpha_v \Delta T - \beta \Delta \alpha \quad \text{Equation 3.31}$$

where α_v is the thermal expansion coefficient and β is the coefficient of volumetric shrinkage of resin due to curing. A viscosity model such as given by Equation 3.15 was also applied.

Integration of Equation 3.30 gives a pressure distribution along the tapered inlet. By neglecting volume change effects in the inlet section and integrating, the following pressure distribution is obtained:

$$P(x) = \frac{U\eta}{K(x)} \left[1 - \frac{V_{fx}}{V_f} \right] x \quad \text{Equation 3.32}$$

Blaurock [29] derived a similar analytical model for the pressure build up in the inlet region. He also argued that besides liquid pressure build-up due to compaction and resin backflow, another contribution to pressure arise from a supporting effect of the fibers. He used Gutowski's model for the transversal stiffness of a fiber stack (Equation 3.17) to estimate this contribution. Ding et al [10] also proposed an analytical model for pressure rise in a tapered closed injection die (see section 3.4.3).

3.4.2.3 Thermo-mechanical modelling

Thermo-mechanical modelling has not been widely studied for the specific case of pultrusion, although issues of internal stresses and warping are known and generally assumed to be intrinsic to pultruded products. Recently however, extensive work by Baran has dealt with this topic. In his studies, the stresses developed due to processing, mainly due to thermal expansion and shrinkage, are evaluated and translated into internal stresses in the final product and/or warpage. He listed the main mechanisms which act during processing and generate internal stresses and distortions as:

- Different coefficients of thermal expansion (CTE) of the thermosetting resin and the reinforcements
- Different CTE between layers of different reinforcement materials and anisotropy within layer, that is, different CTE in the in-plane and out-of-plane directions
- Resin shrinkage during curing reaction
- Temperature and cure gradients inside the composite material, especially for thick parts
- Interaction between the heated die and the part

In [87], Baran presented a model for analyzing process induced stresses and distortions by sequential coupling of a 3D stationary thermo-chemical model (Eulerian framework) with a 2D transient mechanical model (Lagrangian framework) using two different solving methods: the control volume based finite difference (CV/FD) and the finite element with nodal control volume (FE/NCV).

The CV-FD model was implemented in MATLAB and was based on the model firstly proposed by Bogetti and Gillespie [88], [89]. In [88], they described a solving procedure for the temperature and degree of cure in a 2D field, in which fibers are aligned in one of the solving coordinate directions, the other being the through-thickness direction. By means of a coordinate system transformation technique, more complex geometries can be calculated, such as L-shapes and varying thicknesses. In [89], they presented an in-plane stress-strain calculation procedure based in a simplified solving method for temperature and degree of cure in the through-thickness direction only.

Johnston et al [90] presented a more generalized version of this method, in which the fiber orientation in each ply may vary relatively to the plane chosen for the calculation. In Figure 3.10 for example the ply i is oriented at an angle θ_i relatively to the plane $x'-z'$ assumed for the model. A transformation from the $x'-z'$ to the $x-z$ plane is made through the angle β for complex shape geometries. The method applies a plane strain assumption for the calculation of stresses and distortions in the out-of-plane orientation to predict effects such as spring-in.

In the model presented by Baran, the plane is a cross section of the pultruded profile, i.e. the fibers are oriented in the out-of-plane direction relative to the plane chosen for the stress-strain calculation. In [91], Baran expanded the mechanical model to a volume of 3D elements traveling through the die, thus being able to also account for stresses in both longitudinal and transverse directions. In [92] and [93] he modelled L-shape and rectangular profiles composed of rovings and CFM layers. In [94], he analyzed the impact of process induced stresses by transferring the results to a subsequent structural mechanics simulation.

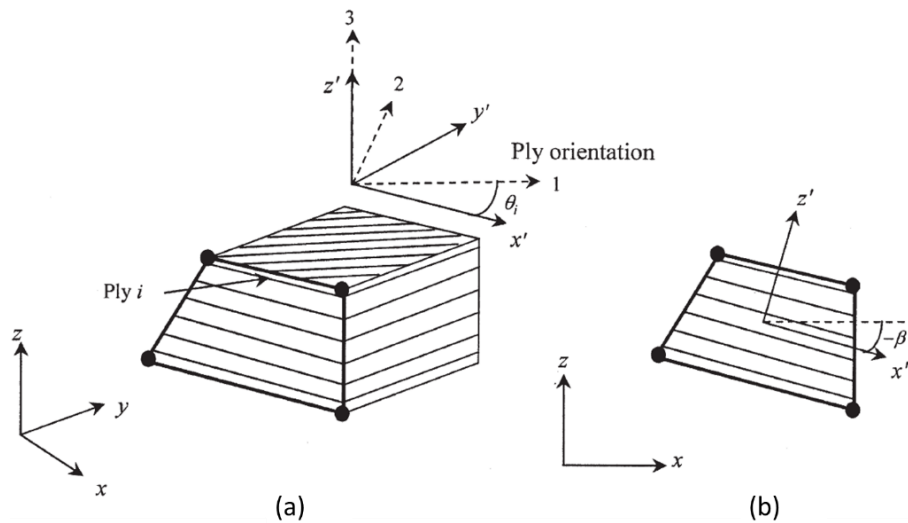


Figure 3.10: Composite part assumed for plane stress-strain model by Johnston et al [90].
 (a) isometric view showing ply orientation; (b) plane view showing principal plane directions and reference plane

3.4.2.4 Modelling of pulling force

Analysis of the force needed to pull the pultruded profile through and out of the die and the contributions to this pulling force arising from different sections of the process is arguably the most important aspect to understanding the pultrusion process. Some authors have also addressed this topic, reaching in some cases very differing results. In general, a combination of analytic and numerical solutions has been applied to sum up the different contributions to the pulling force.

Kim et al [27] described the pulling force as arising from two different sources. The first one occurs in the tapered inlet region from pressure build-up associated with compaction of the wetted out reinforcement material. The resistance in this region is the axial component of the force due to pressure against the mold wall. The other source arises in the constant cross section of the die, by the friction between the resin in liquid and gel phase, up to the point where the resin detaches from the die wall due to shrinkage.

The force per unit length in the opposite pulling direction in the tapered section due to compaction of the wetted out reinforcement σ_c is calculated from the pressure function (Equation 3.32) by:

$$\sigma_c = P(x) \sin \theta \quad \text{Equation 3.33}$$

Where θ is the tapering angle. Integration of Equation 3.33 over the tapered length gives the contribution of compaction of the reinforcement material to the pulling force. Kim argued that further pressure increase can occur in the straight portion of the die due to thermal expansion; therefore Equation 3.30 was also applied to the straight section. Another assumption was that a thin layer of resin exists between the bulk composite and the die inner wall; within this thin resin layer in the immediate vicinity to the wall gels faster, generating thus Coulomb friction directly proportional to the pressure, exerted over the wall. The pressure however, is smaller than predicted by Equation 3.30 due to a shielding effect caused by the same gelled layer. A fully implicit transient finite element method was used for the numerical calculations (see Figure 3.9 (a)). They compared predictions from numerical calculations with measured values of pulling force, finding good agreement to support the model.

Blackrock [29] presented a similar approach by calculating the contribution of a pressure function (see section 3.4.2.2) to the total pulling force. He also used the same assumption of a thin resin film between die wall and composite bulk, estimating its thickness at about 3 μm . He calculated for a given system the cumulated contributions to pulling force approximately as follows:

- 15% due to compaction of wetted out reinforcement material arising in the inlet (radius entrance)
- 5% due to shearing of the viscous resin layer arising in the liquid region up to the gel point
- 80% due to friction in the straight section of the die (compaction of reinforcement and pressure from thermal expansion), up to the point where the shrinkage effect due to curing excels the thermal expansion, i.e. the profile detaches from the die inner walls

Li et al [12] [33] did an experimental study on pulling force, applying different techniques. For example, they used a “mat tracer” method, i.e. feeding a small piece of CFM to produce local higher fiber volume content while it travels through the die. By doing comparing experiments with dies of different lengths, they supported the thesis of the negligible contribution of the downstream part of the die to the pulling force. They also found the pulling resistance in the liquid region to be independent of pulling speed. Finally, they used an especially designed testing assembly to characterize the friction coefficient of the resin in the gel and post-gel regions, deriving an analytical model as a function of temperature and conversion. They concluded that the larger resistance to pulling comes from the gel and post-gel zone up to the detachment point, due to a simultaneous increase in thermal expansion stress and

friction coefficient. They argued that the direct correlation between pulling speed and force is actually explained by an increase of the gel zone length with increasing speed. This is a direct contradiction of the resin film model proposed by Blaurock and Kim et al.

Carlone et al [95], on the other hand, concluded that the viscous drag in the liquid resin region was the main contribution to pulling resistance of a rod profile, while the compaction of material at the die inlet was found to have a negligible effect.

3.4.3 Simulation of the closed injection process

A number of research groups have already proposed models for the pultrusion process with some sort of closed injection and impregnation technique. The focus of these studies is usually on flow simulation especially in the injection zone in order to predict flow and pressure fields.

Kommu et al [35] and Voorakaranam et al [96] studied flow patterns for a die with a hole for injecting resin in the straight section, that is, without an injection cavity. Mustafa et al [36] used the same approach, but compared the results with tapered inlets of different taper angles.

Ding et al [10] evaluated a tapered die with a design according to Gauchel [7]. He solved the continuity equation with Darcy's law numerically using the CV/FEM technique to obtain a pressure field in the inlet section. Additionally, he proposed an analytical solution for the pressure by simplifying the model to one-dimensional flow, and deriving a pressure contribution from drag flow and a pressure flow induced by the resin injection. The numerical and analytical solutions were very close to each other and showed good agreement with experimental results as well.

Liu [97] [98] used a NV/FEM technique to model flow within a pultrusion die. The die was modelled with a constant cross section, and resin was injected through a single hole at a distance of 100 mm from the inlet. He also derived an analytical solution for one-dimensional flow over the entire die length; however, he did not consider any thermal expansion or shrinkage effects, such that the pressure follows a linear decay from the injection point to both inlet and outlet of the die.

Srinivasagupta et al [13] models included predictions of pressure at the die inlet, temperature along the die and pulling force for a specific die design with resin injection.

The research group at Ole Miss presented a number of numerical studies of a die with conical inlet geometry. Rahatekar [99] studied the effects of several parameters (pull speed, fiber volume fraction, resin viscosity and taper angle) on the fiber wet out. He employed a finite volume method as proposed by Patankar and introduced a fill factor to predict whether a particular region is properly wetted out with resin. In [100] he expanded his model to a multilayer reinforcement composed of mats and rovings. Jeswani [101] used the same model to study a design with multiple injection ports and different locations along the length of the tapered section. His goal was to obtain a prediction of wet-out for varying composite thicknesses and high pulling speeds (about 1.5 and 3.0 m/min). Ranga [102] investigated the effect of chamber length, taper angle and pulling speed on wet-out. Palikhel [103] compared a conical inlet attached to the die with the same inlet detached, i.e. with a gap between inlet and die. All of these studies lack comparison with real processing experiments.

Connolly et al [11] focused on flow simulations in the conical inlet region of the die using the commercial software Ansys CFX. The pressure at the resin injection nozzle predicted by the simulation was in agreement with measured values, the measured pressure near the transition from taper to straight die section was however much higher than predicted by the simulation, which was attributed to factors such as roving twist or resin/fiber interactions which were not represented in the model.

4 Resin characterization and modelling

In this section, the experimental work done on the chemorheological characterization of the studied resin system is described, i.e. the evolution of reaction rate as a function of time and temperature as well as the changes in resin physical state as curing progresses. Firstly, the resin formulation is presented along with applied experimental methods, namely DSC and rheology measurements. In the following Subsections, results obtained from each of the methods are then presented along with the development of models for the prediction of the resin properties throughout the curing process.

4.1 Materials and methods

A description of the resin formulation subjected to the characterization work is given in this section, including the several additives and their respective functions in the curing and/or pultrusion processing. Subsequently, the procedure applied for the measurements and the corresponding sample preparation are described.

4.1.1 Resin system

The resin system used in this work is a formulation based on a two-step-curing resin named Daron ZW 015864 (Aliancys, Zwolle, NL) (see section 3.1.3). The resin consists of a prepolymer diluted in styrene (solids content 63.5% – 66.5%) and premixed with an inhibitor. The inhibitor hinders unwanted polymerization during storage, thus prolonging shelf life.

The resin can be processed to a composite part through the combination of pultrusion and a post-forming step. Pultrusion is therefore, in this case, the means for producing a B-staged preform. The first reaction step (B-staging) progresses relatively slowly at room temperature, or may be accelerated by the addition of a catalyst. The second reaction step (radical polymerization) is initiated by the peroxide splitting into free radicals at a higher temperature level. Alternatively, the resin can be fully cured within the pultrusion die by setting the die to a higher temperature level, e.g. 150 °C. In order to undergo curing through the two-step processing route, the resin must be formulated by mixing of different components and additives, which are listed below:

- Di-isocyanate (MDI): the isocyanate groups react with hydroxyl functional groups present in the prepolymers backbones by polyaddition in the B-staging. This reaction results in the formation of a weakly cross-linked network, similar in consistency to rubber

- Catalyst: the catalyst accelerates the B-staging reaction to take place within the pultrusion die. Catalyst amount is adjusted so that B-staging is reached between 2 and 10 min at a temperature range of 80 °C – 100 °C
- Internal mold release (IMR): this is an essential processing additive for reducing adherence of the resin to the die inner walls during curing
- Organic peroxide: initiates the second reaction step by splitting into free radicals at a certain temperature level. The triggering temperature, typically between 100 °C – 120 °C can be defined by selection of an appropriate peroxide

In the initial screening it was found that the resin reactivity is extremely sensitive to the amounts of other components added, specially the ratio of catalyst and IMR. The IMR effectively slows down the reaction, so that by adding IMR, one has to increase the catalyst amount in order to obtain the same reactivity. The resin formulation shown in Table 4.1 was applied in all characterization investigations.

By separately premixing the A and B components, no reaction takes place. This is important since the first reaction step starts directly upon mixing of A and B, as usual with fast reacting polyurethane systems.

Table 4.1: Resin formulation applied throughout this work

Resin component	Parts per weight (ppw)
A Component	
Daron ZW 015864	100
Catalyst	1.0
IMR	2.0
B Component	
MDI	25
Peroxide	1.0

The resin system was characterized with focus on obtaining models for the cure kinetics, flow behavior and shrinkage evolution throughout curing. These models are used as input in the simulation studies. In the following sections, the characterization methods and the models obtained will be described in detail.

4.1.2 Differential Scanning Calorimetry (DSC)

DSC was applied as a method to detect the development of cure from liquid resin to fully cured thermoset matrix. Calorimetric measurements were performed with a Netzsch DSC204 F1 Phoenix. Dynamic scan measurements were carried out at different linear temperature ramps (0.5 K/min, 1.0 K/min, 5.0 K/min) from -20 °C to 185 °C. This was followed by cooling down to room temperature at 5 K/min and a second heating step to assess whether residual reaction takes place. It is inevitable that a small portion of the reaction is not captured by the characterization method. In order to keep this error as low as possible, efforts are made to obtain a precise mixing ratio while at the same time starting the measurement as soon as possible. For the sample preparation, the following procedure was applied:

1. Cooling down of the DSC furnace to +5 °C
2. Weighting of the A and B components in a precision balance (accuracy 0.001 g)
3. Mixing by hand for 30 s
4. Metering of 16 - 18 mg to the DSC pan by a high precision pipette (accuracy 1 µL)
5. Sealing the DSC pan and placing it into the DSC sample holder
6. Cool down to -40 °C at maximum cooling rate (approximately 50 K/min)

Steps 2 through 5 were conducted in all measurements in approximately 2 min. Three replicates were measured for each heating rate. Results show reproducible curves for all measured scans. Typical DSC curves obtained for the three heating rates measured are shown in Figure 4.1. Characteristic values obtained from the plot analysis are listed in Table 4.2. The onset is typically defined as the point of intersection of two tangents, one at the inflection point during the reaction and the other at the linear baseline, denoting start and end of the reaction, respectively. The peak is determined at the highest value within the reaction stage. The area is calculated between the DSC plot and the baseline defined by the tangent traced between a point in the flat region before the onset of reaction and another after the end of reaction.

4.1.3 Rheology measurements

Rheology measurements in oscillation mode were carried out to evaluate flow behavior as the resin goes from liquid to cured state. A MCR301 rheometer (Anton Paar GmbH) in the disc-plate configuration according to DIN 53018-1 was used for the measurements. The top disc has a diameter of 25 mm. The measurements were carried out under 1 Hz frequency (corresponding to an angular frequency of 6.28 rad/s) and amplitude of 0.16 mrad of

deflection angle (corresponding to a strain amplitude of 0.2 %). A controlled normal force of zero N is kept constant throughout the measurement, while the gap is adjusted. Dynamic scan rates of 1.0 K/min and 5.0 K/min were applied from 5 °C to 180 °C. The following procedure was followed in the preparation of samples for rheology measurements:

1. Cooling down of the rheometer chamber to +5 °C. Since the maximum cooling rate is much lower than in the DSC, the initial temperature is set as low as possible to hinder early stage reaction, but also preventing accumulation of condensed water from ambient air
2. Weighting of the A and B components in a precision balance (accuracy 0.01 g)
3. Mixing by hand for 30 s
4. Pouring of approximately 1 g to the center of the rheometer bottom plate
5. Lowering the upper disc close to the gap set for the measurements (1 mm)
6. Removal of resin excess at the disc edges
7. Start of measurement

Steps 2 through 7 were done in all measurements within 3 - 4 min. Due to the slower preparation procedure and the larger resin amount needed for the measurement, it is expected that a larger amount of the curing reaction has taken place at the time the measurement is started, as compared to DSC.

The values of storage (G') and loss (G'') moduli in shear are obtained from the measurements (equations 3.6 to 3.10). From these values, the apparent viscosity of the sample is calculated according to equations 3.11 to 3.14. In the following discussion, wherever the term viscosity is used, it actually refers to the modulus of the complex viscosity (see Section 3.2.2).

4.2 DSC measurement results

Typical measurements of heat flow plotted against the temperature are given for the applied heating rates in Figure 4.1. The two reaction steps can be clearly separated for all heating rates measured. The first flat peak represents the B-staging reaction, while the second sharp peak is typical of a self-accelerated polymerization, initiated by the splitting of the peroxide initiator into free radicals. In Figure 4.2, an example of the conducted plot analysis is shown with the characteristic values obtained from the measurement. The values obtained from measurements under the different dynamic scans are then listed in Table 4.2.

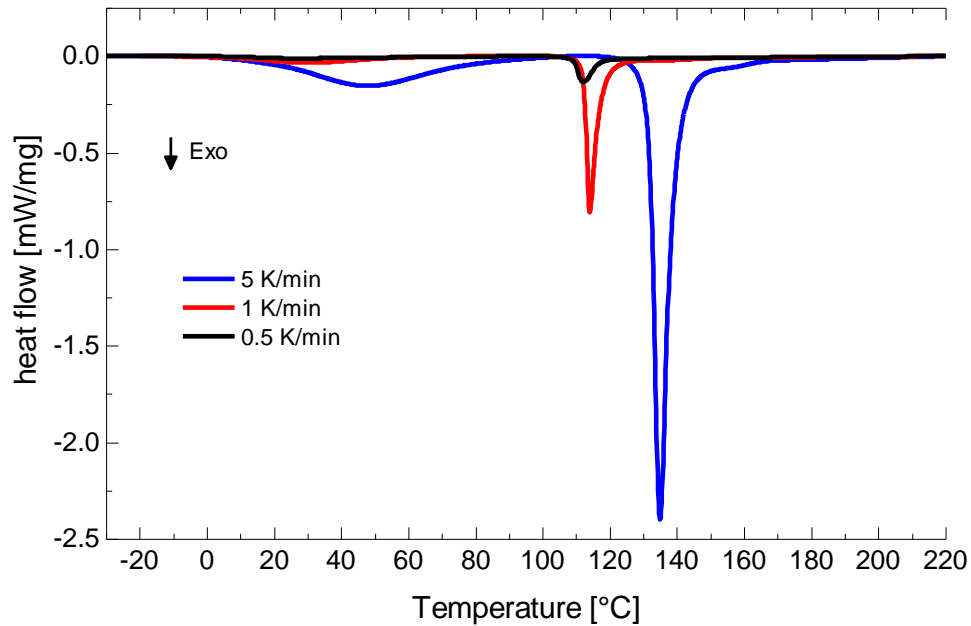


Figure 4.1: Heat flow data from DSC measurements at three different heating rates

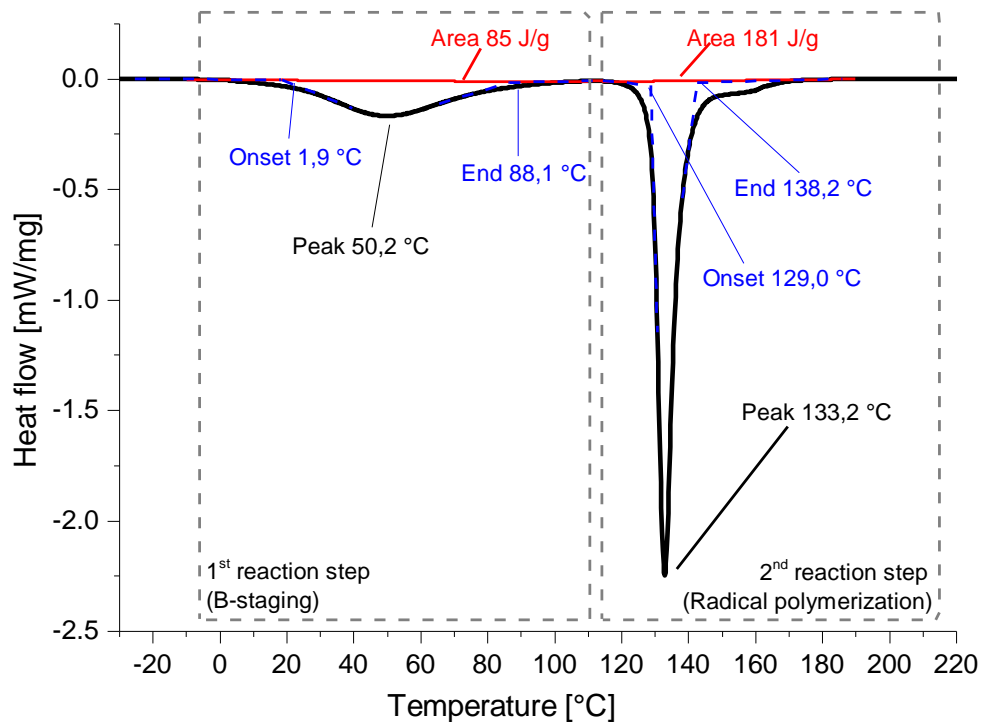


Figure 4.2: Analysis of DSC data from measurement at a dynamic scan rate of 5 K/min

The onset of the first reaction step occurs very early at approximately 0 °C. No clear dependence on the heating rate can be attested to the onset, in contrast to all other characteristic values. This is an indication of process variability arising from the sample preparation procedure described above. The almost immediate onset is in agreement with the observation of material behavior upon mixing by hand, in which the material starts to

develop heat shortly after mixing. Due to the preparation procedure, it is inevitable that a small portion of the first reaction is not caught by the DSC measurements. Since the measurements were found to be reproducible, the amount of reaction occurring prior to the measurement is assumed to be negligible. The first reaction step corresponds to approximately 30% of the total heat of reaction.

Table 4.2: Characteristic values of temperature and heat release for the two-step curing reaction under different heating rates

Heating rate	1 st reaction step (B-staging)				2 nd reaction step (Radical polymerization)				Total Area [J/g]
	Onset [°C]	Peak [°C]	End [°C]	Area [J/g]	Onset [°C]	Peak [°C]	End [°C]	Area [J/g]	
5,0 K/min	1.9	50.2	88.1	85	129.0	133.2	138.2	181	266
1,0 K/min	6.0	22.9	56.5	89	113.0	115.9	119.8	184	273
0,5 K/min	-2.9	18.7	46.9	81	103.9	108.1	111.0	165	246

4.3 Kinetic modelling

Fitting of data from DSC measurements was done with the software NETZSCH Thermokinetics 3.1. The software contains regression methods according to ASTM E698, Friedman and Ozawa-Flynn-Wall (see section 3.2.1). It is noted that the model developed in this study is purely empirical, i.e. it does not convey any of the reaction mechanisms which were qualitatively described in Section 3.1.3. The regression procedure within the software is well explained in [21]. An initial model composed of reaction steps is chosen for modelling a multi-step reaction mechanism. The type of model is chosen based on appearance of the DSC heat flow curves. A nonlinear least-squares fitting method is then applied for data regression and fitting of optimum parameters. Calculation of regression values is done by means of a Runge-Kutta method of 5th grade. Minimization of the sum of least square values is done by the Gauss-Newton method.

In the present case, fitting of data was attempted by setting two different models. A first approximation was done applying two reaction steps in series, in analogy to the two reaction mechanisms of B-staging and final curing discernible in DSC. The model is similar to the final three-step model described in Equations 4.1 through 4.4, considering only reaction steps 1 and 2. The fitting procedure executed by applying the two different reaction models leads to the results shown in Figure 4.3.

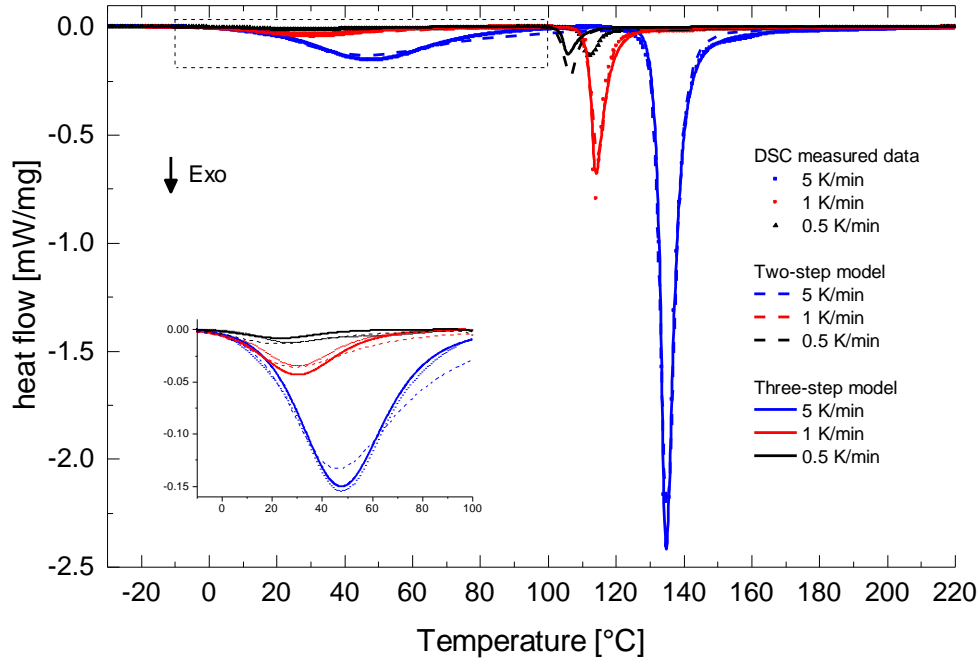


Figure 4.3: Original DSC data and data obtained from fitting to the two-step and three-step models

It can be seen that a generally good representation of measured data is achieved by the two-step model. However, the fit for both reactions present a discernible discrepancy from measured data, as seen by the differences in the peaks and at the end of the second reaction exotherm. Statistical values for the sum of least square residuals of 9.24 and correlation coefficient of 0.9887 were obtained. The addition of a third reaction step in the model leads to a better fitting of the reaction as measured by DSC. A sum of the least squares residuals of 2.94 and a correlation coefficient of 0.9964 were obtained for the three-step model. It can be concluded that a better representation of DSC data is achieved by the three-step in comparison to the two-step model. The final model applied throughout this study is therefore composed of three sequential reaction steps:



It should be noted that the model is purely empirical, i.e. the three reaction steps in the model do not imply three different reaction mechanisms taking place during cure. In fact, while step 1 describes the B-staging reaction, the radical polymerization is described by the simultaneously occurring steps 2 and 3. For each reaction step, a cure rate dependency function is fitted in terms of the respective reaction product in the following form:

$$\frac{d\alpha_i}{dt} = A_i \exp\left(\frac{-E_{Ai}}{RT}\right) \cdot f(\alpha_i) \quad \text{Equation 4.2}$$

where α_i is the amount of reactant which has converted into a product through reaction step i by time t , i.e. the degree of cure for that particular reaction step, which goes from 0 to 1. A_i is a pre-exponential factor and E_{Ai} the activation energy for the reaction step i . The following functions were found to fit well the respective reaction steps:

Reactions 1 and 2, n^{th} order reaction with autocatalysis

$$f(\alpha_i) = (1 - \alpha_i)^{n_i}(1 + Kcat_i \alpha_i), \quad i = 1, 2 \quad \text{Equation 4.3}$$

Reaction 3, n^{th} order reaction

$$f(\alpha_i) = (1 - \alpha_i)^{n_i}, \quad i = 3 \quad \text{Equation 4.4}$$

where n_i is the reaction order and $Kcat_i$ an autocatalytic factor for the reaction step i . Since the reaction is modelled as a sequence of reaction steps, the rate of reaction for a particular step depends on the conversion which has already been reached in the previous reaction step(s). This is done by multiplying the term α_i by the previous degree of cure α_{i-1} . The following reactions are then obtained for each reaction step.

$$\frac{d\alpha_1}{dt} = A_1 \exp\left(\frac{-E_{A1}}{RT}\right) \cdot (1 - \alpha_1)^{n_1}(1 + Kcat_1 \alpha_1) \quad \text{Equation 4.5}$$

$$\frac{d\alpha_2}{dt} = A_2 \exp\left(\frac{-E_{A2}}{RT}\right) \cdot (\alpha_1(1 - \alpha_2))^{n_2}(1 + Kcat_2 \alpha_1 \alpha_2) \quad \text{Equation 4.6}$$

$$\frac{d\alpha_3}{dt} = A_3 \exp\left(\frac{-E_{A3}}{RT}\right) \cdot (\alpha_2(1 - \alpha_3))^{n_3} \quad \text{Equation 4.7}$$

The overall degree of cure α is given by the weighted sum of the α_i terms.

$$\alpha = FR_1 \alpha_1 + FR_2 \alpha_2 + FR_3 \alpha_3 \quad \text{Equation 4.8}$$

The term FR_i is the fraction of the reaction step i relatively to the total reaction. Since the DSC analysis is based on the developed exothermic heat of reaction, FR_i is related to the contribution of reaction i to the overall degree of cure and to the total heat of reaction. The volumetric internal heat generation term \dot{q} is given by rearrangement of Equation 3.5.

$$\dot{q} = \rho H_R \frac{d\alpha}{dt} = \rho H_R \left(FR_1 \frac{d\alpha_1}{dt} + FR_2 \frac{d\alpha_2}{dt} + FR_3 \frac{d\alpha_3}{dt} \right) \quad \text{Equation 4.9}$$

The total heat of reaction H_R in Equation 4.9 is taken as the maximum value obtained in the DSC measurements (361 J/g). Table 4.3 lists the parameters obtained from fitting of the DSC data to the three-step model.

Table 4.3: Fitted parameters for final kinetic model according to Equations 4.1 to 4.7

Parameter	Reaction step 1	Reaction step 2	Reaction step 3
A_i [s^{-1}]	1.305×10^9	2.079×10^6	2.044×10^3
E_{Ai} [J/mol]	6.971×10^4	9.798×10^4	3.1×10^4
n_i	2.1709	0.9575	3.9037
$Kcat_i$	0.4956	1.253×10^5	-
FR_i	0.2877	0.2496	0.4627

The evolution of the degree of cure can be calculated for a given temperature cycle by integration of Equation 4.5 to Equation 4.7. The Thermokinetics software can perform such a calculation for a sequence of constant temperatures and linear heating or cooling rates. A plot for a series of isotherms is given in Figure 4.4.

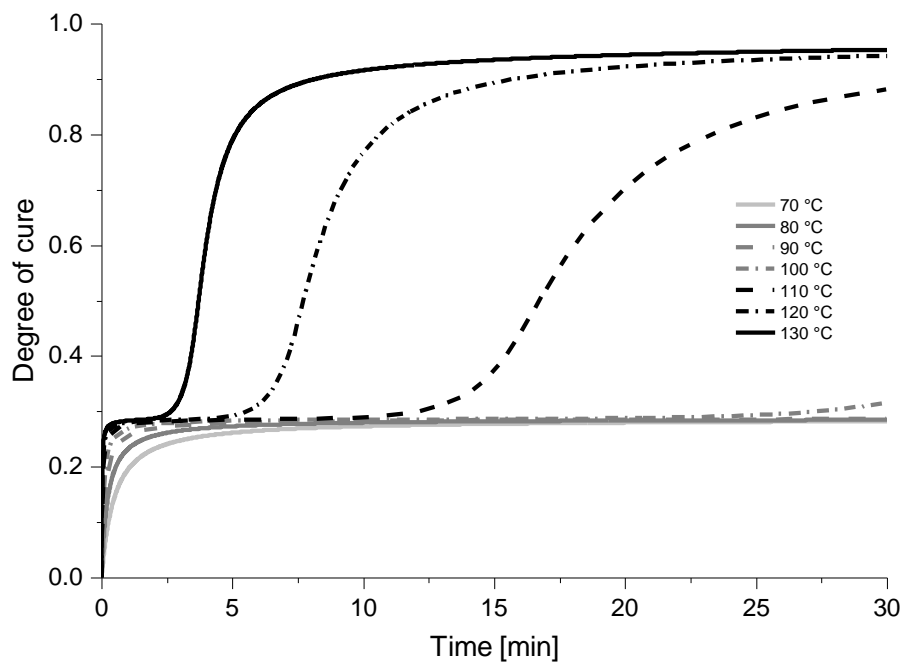


Figure 4.4: Degree of cure evolution for a series of isotherms between 70 and 130 °C

The plateau at a conversion of 0.29 ($= FR_1$) observed in the lower temperature isotherms depicted above corresponds to completion of the B-staging reaction step. Analysis of this plot gives insight into the processability of the studied formulation to a B-stage during pultrusion.

Assuming no substantial temperature increase due to the exothermic heat released in the first reaction step, one can evaluate for example a die temperature set point of 100 – 110 °C as safe for pultrusion processing, with a time span of approximately 10 min before the second reaction is triggered.

4.4 Rheology measurement results

For the modelling of the viscosity evolution throughout the curing, it is necessary to have a prediction of the degree of cure evolution parallel to the dynamic rheology scan. A considerable temperature lag between the set temperature of the measuring block and the real temperature of the sample was observed for the cooling step. Because of that, the temperature was measured independently by fixing thermocouples to the sample holder on the upper and bottom plates. A gap of 1.5 mm was kept constant throughout the measurements. The temperature evolution is shown against the rheometer temperature for a heating rate of 5 K/min in Figure 4.5. In order to obtain a better estimate of the degree of cure during a rheology measurement, cure simulations were conducted using the in-house finite difference algorithm (see Section 7.1.4). One of the simulations applied the temperature cycle measured in the center of the upper disc as the ambient temperature, the other applied the temperature at the center of the bottom plate for the curing cycle. The estimate of the degree of cure was then obtained as the average of the two curves resulting from the simulations. Results are shown in Figure 4.5.

An uneven temperature distribution can be seen by the difference between the temperatures at the disc bottom and top. The simulation results indicate that an incipient reaction already occurs prior to starting a rheology measurement. The absolute value of the degree of cure is estimated at 0.7% at the beginning of the measurement. Despite this low initial value, the reaction is already evolving at the beginning of the rheological test, resulting in a much faster evolution of both reaction steps compared to the predicted by the set temperature signal. The exothermic peaks of the measured and predicted temperatures at the top disc center are overlapping, indicating the accuracy of the FD-model. The measured temperature at the bottom is delayed in comparison to the temperature predicted by the model; this can be explained by the fact that the thermocouple was located directly above the heating unit (Peltier element), which forced the temperature to remain close to the rheometer set temperature. This continued until the bulk of the resin undergoes the radical polymerization. The heat release is then sensed at the same time by the top and bottom thermocouples.

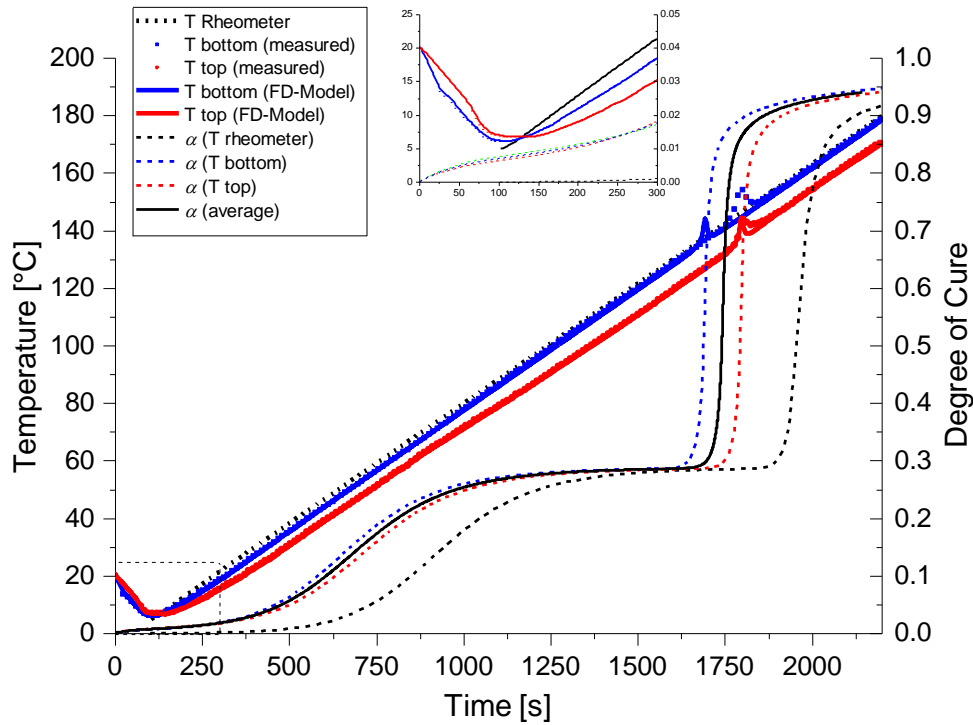


Figure 4.5: Temperature measurements in the rheometer sample region and degree of cure evolution for rheometer set and measured temperatures

In Figure 4.6 the curves of the degree of cure as predicted by the corrected temperature and by the rheometer set temperature are plotted together with the corresponding rheology measurement results under 5 K/min heating rate. The corrected curve is clearly a better estimate of the degree of cure, as it nearly overlaps with the onset of the radical polymerization step as captured in the rheology measurement by an increase in storage modulus. Figure 4.7 shows the plot obtained from a rheology measurement under a heating rate of 1 K/min.

As stated in section 3.2.2, the viscosity signal is plotted only for the reaction stage up to gelation, defined as the crossover between G' and G'' . This corresponds to a calculated apparent viscosity of 83.2 Pa·s for a heating rate of 5 K/min. This value lies in agreement with reported values for the modulus of complex viscosity upon reaching the gel point, of 50 Pa·s [4] and 100 Pa·s according to ASTM D4473 [54]. For the lower heating rate of 1 K/min, however, a much larger value was observed, indicating a strong dependence on the heating rate and thus also on the curing rate. The trend indicates that at a higher heating rate the polymer network “freezes” in a gel state faster than for lower rates. Furthermore, the temperature at which the cross-over occurs is higher for the faster heating rate, indicating a concurrent effect of heating and curing in the network formation. According to the calculated

degree of cure, gelation occurs just prior to reaching the B-stage plateau, which is coherent with the observed material behavior upon mixing.

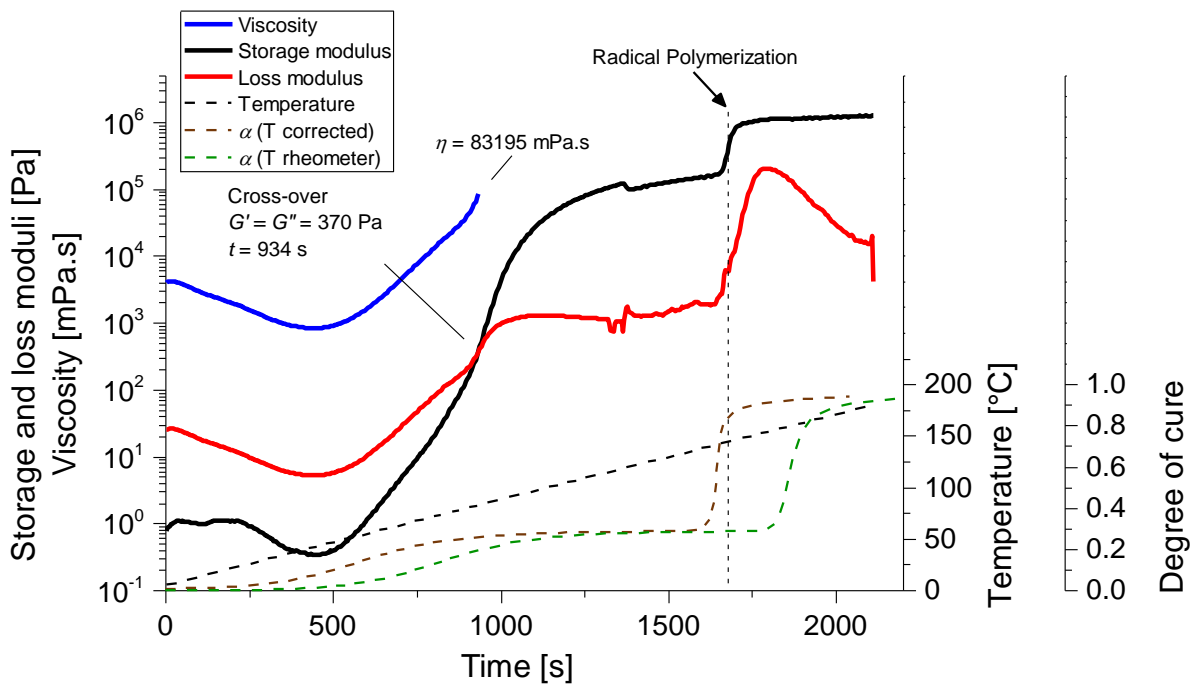


Figure 4.6: Results from a rheology measurement during cure at a heating rate of 5 K/min

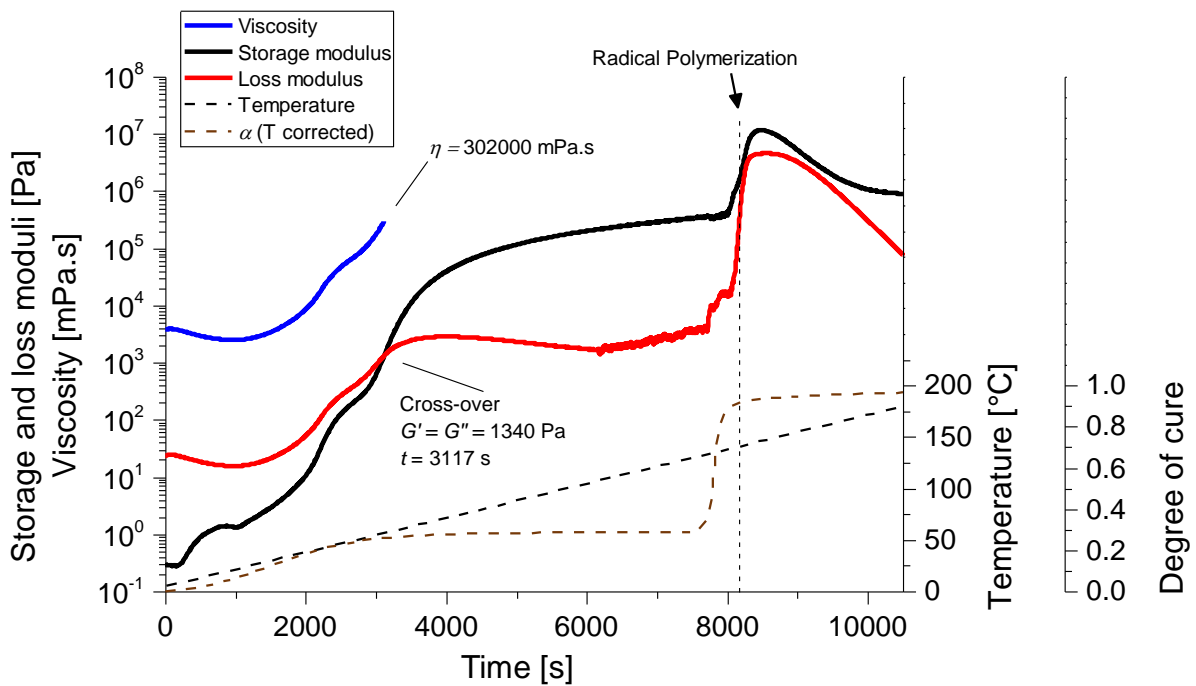


Figure 4.7: Results from a rheology measurement during cure at a heating rate of 1 K/min

The observed values for both heating rates are shown in Table 4.4. Three measurements were considered for each heating rate, and the average values were considered for evaluation. As already observed during DSC measurements, a better repeatability could be obtained for the higher heating rate. This is reflected in the higher standard deviation values calculated from the measurements at 1 K/min.

By further progression of curing, the sample becomes increasingly stiffer. This produces measurement errors related to stick-slip effects under predefined strain. These can be seen in the G'' curve, for example in Figure 4.6 after about 1300 s of measurement time. These effects can lead to complete loss of contact between disc and sample, as seen by a slight drop in the G' plot in Figure 4.6. Such type of error can be avoided by decreasing the strain amplitude as the material becomes stiffer.

A comparison of the curves of storage modulus and degree of cure reveals that physical changes, most possibly related to network formation, are taking place, which cannot be captured by the DSC technique. Reaching a plateau at a degree of cure level of about 0.28 indicates the presence of a stable B-staged material. Such a plateau is not seen in the storage modulus, but rather a further continuing increase in the signal. If the material is not experiencing any change in physical state, G' would be expected to drop due to softening of the material caused by temperature increase. Triggering of the second reaction step is, however, clearly seen in the simultaneous increase in both G' and degree of cure signals.

Table 4.4: Temperatures and calculated apparent viscosities at the cross-over between G' and G'' for different heating rates

Heating rate	Cross-over temperature [°C]	Cross-over viscosity [Pa·s]	Degree of cure (calculated)
5,0 K/min	81.7 ± 1.0	84 ± 6	0.257 ± 0.002
1,0 K/min	50.6 ± 2.2	794 ± 158	0.243 ± 0.007

4.5 Rheology modelling

The empirical procedure found in the literature (see section 3.2.2) was followed to find a viscosity model, similar to Equation 3.15, as a function of temperature and degree of cure. However, a straightforward regression is only possible by measurements of DSC and rheology done at a set of the same isothermal temperatures, i.e. temperature is taken as a constant and viscosity is plotted directly against the degree of cure in logarithmic scale to find the fitting parameters η_{∞} , E_v and B . Since dynamic measurements were carried out in this study, data regression was done directly from dynamic data of viscosity, temperature and

degree of cure. The software OriginPro was used for data regression. It can apply non-linear fitting of data to a user-defined equation. The software uses the Levenberg-Marquardt (L-M) algorithm to adjust the parameter values in the iterative procedure [104].

One problem encountered during the fitting process is the discrepancy of plot trends of the degree of cure and moduli, already discussed in the previous section. A zoomed plot of the initial region of Figure 4.6 up to reaching the gel point is shown in Figure 4.8. It can be clearly seen that the data cannot be well reproduced according to the Lee model (Equation 3.15). The viscosity follows an Arrhenius-type of relation to temperature, with temperature increase leading to a decrease in viscosity. Furthermore, the degree of cure is not monotonically increasing as the viscosity, but rather approaching a plateau after an inflection point at approximately 575 s. This leads to an inflection on the viscosity curve as calculated by the model, following the inflection on the degree of cure curve. The Castro-Macosko model (Equation 3.16) is considered to give a better representation of the actual viscosity evolution, as it goes to infinity when the material reaches gelation. The parameters η_{∞} , E_v , A and B were found by manual curve fitting. The reason for this is that the automatic fitting procedure available in Origin does not deliver good results; it does not weight values according to the order of magnitude, i.e. the curve is only well fitted for the higher viscosity values.

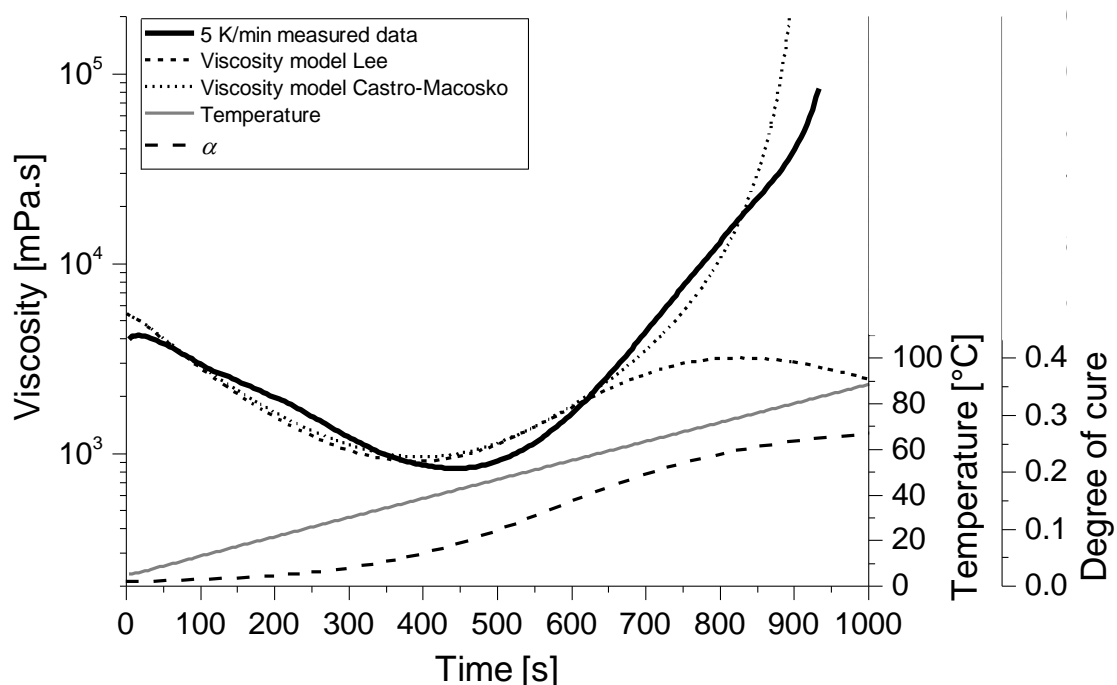


Figure 4.8: Zoomed plot of initial region of Figure 4.6 (heating rate 5 K/min) with viscosity data fitted by the Lee and Castro-Macosko models

The same curve behavior was observed in the measurements at the lower heating rate. The fitting procedure was done the same way according to the Castro-Macosko model. The final fitted parameters were found by averaging the parameters obtained for the two heating rates. Figure 4.9 shows curves for both measured heating rates together with curves obtained from the model according to the fitted parameters shown in Table 4.5. The model fits the viscosity evolution obtained from both heating rates reasonably well. A probable cause for the discrepancy might be the difference in mass of DSC and rheology samples. The relatively large amount of material subjected to a measurement in the rheometer may have a possibly inhomogeneous temperature distribution across the profile thickness. This would lead to an onset of reaction at the surface layer, while the bulk of the material is still heating up, thus leading to a more pronounced viscosity drop prior to curing. For the lower heating rate, the effect is opposite; a self-acceleration process in the bulk of the material might already take place, leading to a faster curing than predicted by the surface temperature.

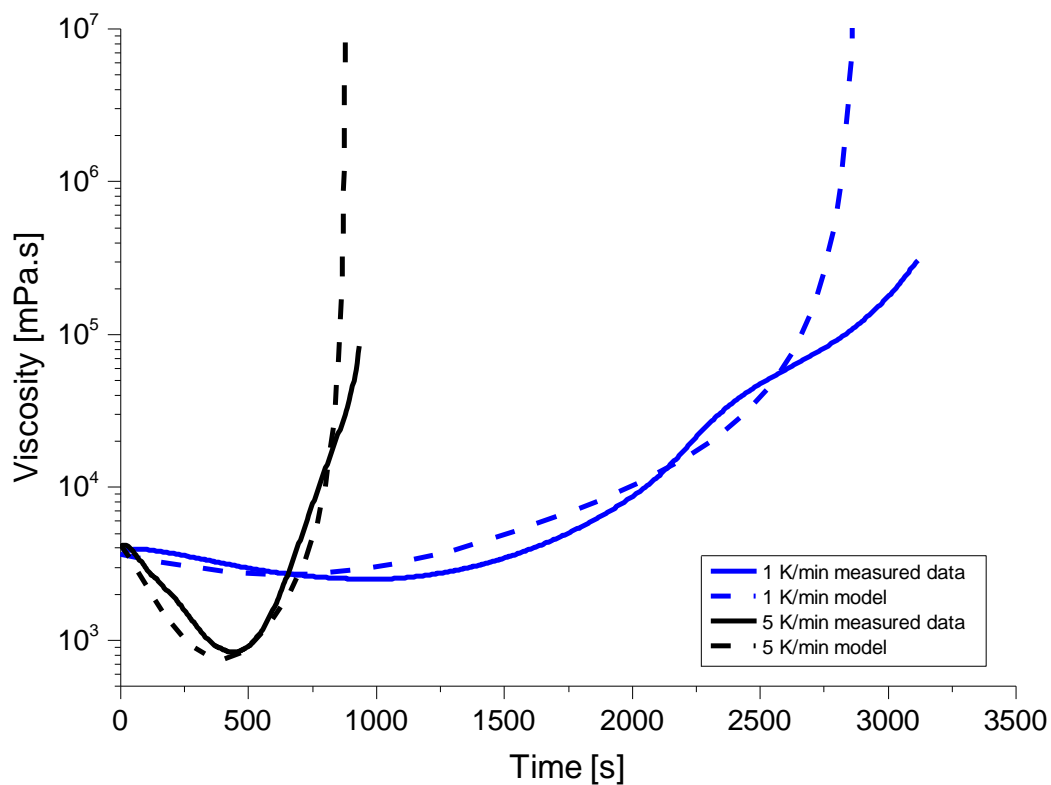


Figure 4.9: Fitted viscosity curves for all heating rates

Table 4.5: Fitted parameters of Castro-Macosko viscosity model (Equation 3.16)

η_{∞} [Pa.s]	E_v [J/mol]	α_g	A	B
8×10^{-8}	56750	0.25	4.65	-10.5

5 Fiber characterization and modelling

To get a better estimate of input parameters for the process simulations, methods for characterizing the fiber reinforcements employed in pultrusion were developed and tested in this study. Most literature dealing with simulation of the pultrusion process have used theoretical models for the estimation of permeability, e.g. from Kozeny-Carman or Gebart. These models were fitted to the materials under study to assess their accuracy.

5.1 Material and methods

A description of the different fiber reinforcement materials tested is given in this section. Subsequently, the testing molds and the testing procedure developed in this work are described.

5.1.1 Reinforcement materials

The following reinforcements were characterized in terms of compressibility:

- Glass fiber (GF) direct rovings 399A-AE, 4.800 tex (3B Company, Belgium)
- Carbon fiber (CF) rovings Sigrafil C30, 50k (SGL Group, Meitingen, Germany)
- Glass Continuous Filament Mat (CFM) 300 g/m² M8643 (3B Company)
- Glass Continuous Strand Mat (CSM) 300 g/m² Conformat N720 (Superior Fibers, LLC, Ohio, US)

Measurements were also performed on reinforcements layers wetted out with silicone oil (Korasilon® M 1000, Kurt Obermeier GmbH & Co. KG, Germany) with a dynamic viscosity of about 1 Pa·s at room temperature as soaking fluid. This value is within the range of viscosities of typical resin formulations used in pultrusion.

The same glass and carbon fiber rovings were characterized in terms of their permeability. Measurements were also conducted on CFM M8643 stacks. Silicone oil (Korasilon® M 100) with a dynamic viscosity of about 0,1 Pa·s at room temperature was used as permeating fluid.

The glass and carbon fiber rovings have coincidentally similar theoretical fiber volume content on a roving basis, in spite of the different densities, linear weight (usually given in tex, i.e. g/km) and fiber counts. The fiber volume content of a cross section filled with rovings is given by the following equation:

$$V_f = \frac{N_R \cdot LW}{A \cdot \rho_f} \quad \text{Equation 5.1}$$

Where N_R is the number of rovings and LW is the linear weight. The nominal and real values for the rovings tested are given in Table 5.1. The values of linear weight were measured by weighting of roving samples of 5 m in length. Six repetitions were performed for three different rovings of the same lot.

Table 5.1: Nominal and real values of linear weight and rovings tested in this study

Roving type	ρ_f [kg/m ³]	Nominal values		Real values	
		LW [tex]	LW/ρ_f [x10 ⁻⁶ m ²]	LW [tex]	LW/ρ_f [x10 ⁻⁶ m ²]
3B 399A-AE	2620	4800	1.832	4910	1.874
SGL Sigrafil C30 50k	1800	3300	1.833	3322	1.845

The different types of mats have the same main function of providing strength perpendicular to the pultruded product longitudinal direction. The Conformat N720 is also marketed as a mat providing a better surface smoothness. The two mats exhibit a different appearance, despite having the same area weight. The area weight tolerance was given at $\pm 10\%$. However, a much lower discrepancy ($\pm 3\%$) was found from several weighted pieces cut from the same roll.

5.1.2 Compressibility method

Knowing the compressibility of pultrusion reinforcements is especially important when designing a lay-up sequence for a pultrusion laminate. Many standard pultrusion profiles are composed of stacked sequences of CFM and roving layers. Each layer has a different fiber volume content, which is in part a function of the intrinsic fiber compressibility. Figure 5.1 shows this condition. For a given cross section thickness S , one (or more) CFM layer(s) with thickness S_M is a constituent of the profile. For the remaining cross section, a number of rovings (thickness S_R) must be chosen in order to achieve a profile with desirable mechanical properties and easy processability. The pressure P is the force per unit area needed to compress the fiber package to the geometrical constraint of the cross section given by the pultrusion die. The fiber volume fraction in each of the layers is a function of the mechanical pressure P and, in the case of multiple reinforcements, of the extent of the so-called nesting effect, which is understood as the intertwining of adjacent layers into each other at their interface.

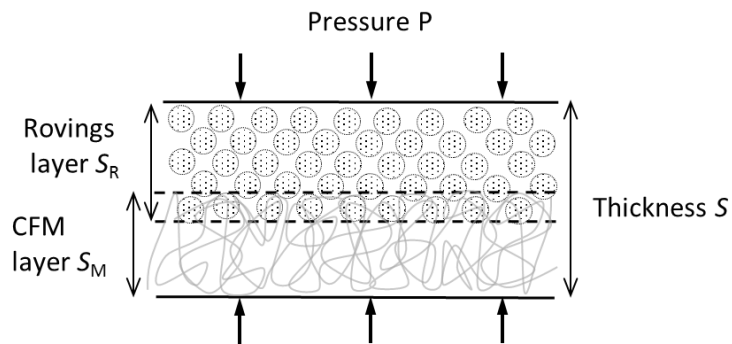


Figure 5.1: Schematic representation of a laminate cross section composed of a CFM and a roving layer

For measuring the compressibility, a mold with a cavity of 180 x 346 mm² was employed. The mold has lateral shear edges and both ends open to the atmosphere. This allowed a roving fiber stack to be positioned in a similar way as it would be in a pultrusion die, with the individual rovings stretched and in the parallel orientation. The mold was mounted to a universal testing machine.

The CFM layers were cut to cavity dimensions. Rovings were positioned by means of fixing a polyethylene guiding plate with threading holes typically used in pultrusion processing trials. The hole arrangement ensured a homogeneous distribution across the width of the cross section. This was done by a lateral shifting between holes of a column according to the pattern shown in Figure 5.2. This distribution is similar to patterns applied in the design of guiding plates for actual pultrusion processing trials. Pictures of the mold assembly with layers of rovings already in place are shown in Figure 5.3.

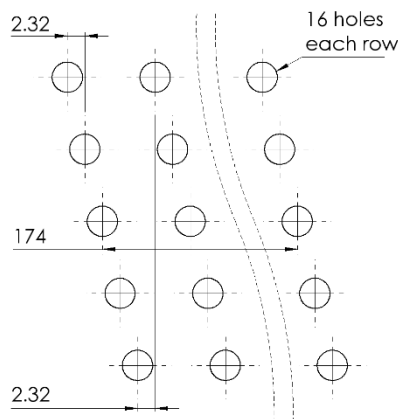


Figure 5.2: Hole pattern used in guiding plates for positioning of rovings in compressibility measurements

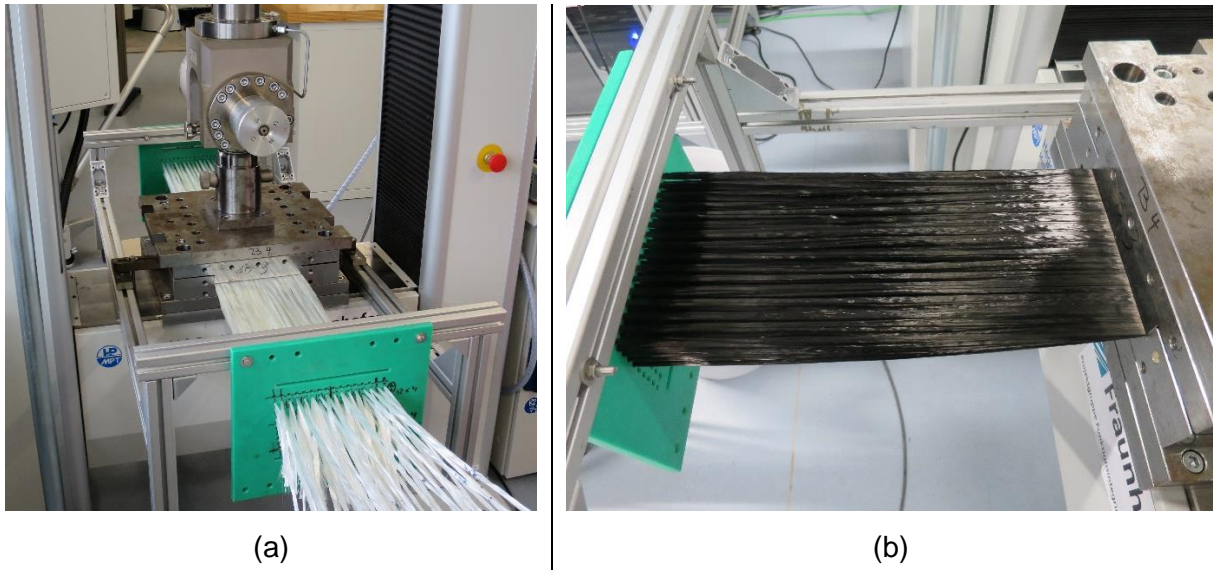


Figure 5.3: (a) Compressibility mold with glass fiber layer positioned for testing; (b) Compressibility mold during testing of a carbon fiber layer

The load program was controlled at a displacement rate of 1 mm/min up to a maximum compression load of 100 kN, which corresponds to 1.64 MPa compaction pressure. This was followed by a time span of 5 min during which the position was held constant. The applied force and corresponding displacement data were recorded. An example of a load-displacement curve is shown in Figure 5.4.

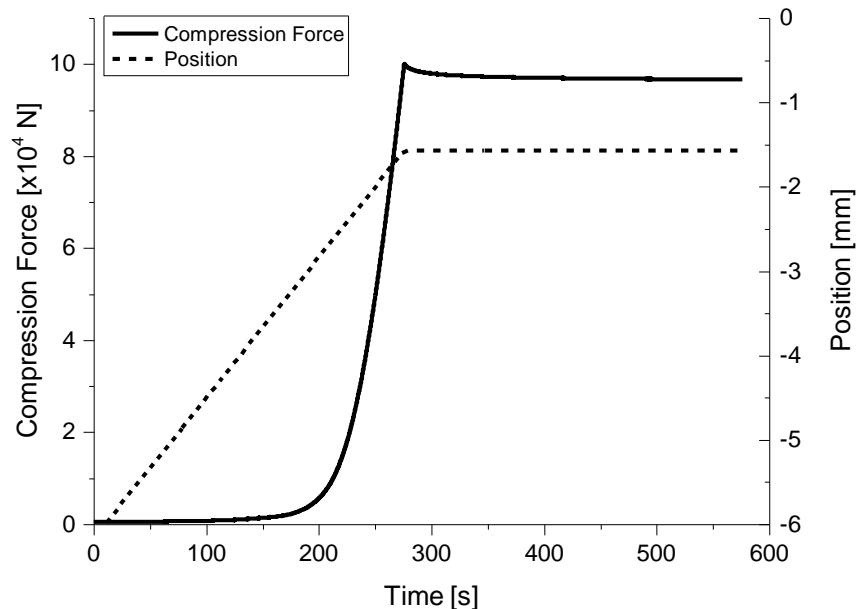


Figure 5.4: Example of curve load vs. displacement obtained from the compression measurement of a fiber roving fiber stack

The compliance of the assembly composed of the mold and testing machine was determined by performing a measurement without any reinforcement material. It was found that the mold deflected 0.84 mm at a compression load of 100 kN relative to its closed position without load. The real mold gap was then calculated by adding the displacement curve with reinforcement material and the mold compliance curve. The fiber volume content was obtained by using Equation 5.1 and substituting the cross section A by the mold width and the measured gap. The compaction pressure was obtained by dividing the compression load by the mold surface area. At least two repetitions by compacting new material were performed for each condition. Reproducibility was in general very good. In cases of deviating curves, a third measurement was performed. The stress relaxation behavior under constant displacement discernible in fiber reinforcements (see Figure 5.4) [62] was not included in this analysis.

5.1.3 Permeability method

The permeability of fiber reinforcements is the most important parameter for simulating fluid flow in composite processes. Most experimental studies on in-plane permeability have used cells designed for measuring reinforcements typically used in RTM (e.g. fabrics, non-crimp fabrics). Published studies focusing on flow simulation in pultrusion dies have usually applied a permeability value calculated from a theoretical model (see Section 3.3.2). To validate this assumption for reinforcement layers used in pultrusion processing, a method was developed for the experimental estimation of the permeability of a reinforcement stack in which the arrangement of rovings is similar to the processing configuration.

The mold for measuring the permeability had a cavity of 396 x 396 mm² and a central injection nozzle. The mold was made of steel to avoid deflections (and consequently local volume content variations), especially when applying the relatively high compaction pressures common in pultrusion. The mold was analogous to the compressibility mold, i.e. has shear edges for positioning and testing of a roving layer, and it was mounted to a universal testing machine. The rovings were also positioned by means of guiding plates with the same hole pattern shown in Figure 5.2.

For the permeability measurements, the cavity thickness was fixed by placing a stack of steel strips of defined thickness (distancing shims) laterally between the mold halves. The mold was then closed with the reinforcement material inside, such that the upper mold half (approximate weight 185 kg) prevented the material from shifting. When measuring a roving layer, the reinforcement stack was tensioned by means of clamping bars which were then

pulled away from the mold. Directly thereafter, a hole was cut through the reinforcement by a punching tool with diameter 10 mm directly over the outlet of the central injection nozzle. The central injection hole cut through the reinforcement was necessary to avoid flow gradients through the thickness. The testing machine then pressed the two mold halves until the distancing stack can no longer be moved, thus setting the cavity thickness. This preparation sequence is shown in Figure 5.5. The procedure gave excellent cutting results for CFM, fabrics and roving stacks, as seen in Figure 5.6.

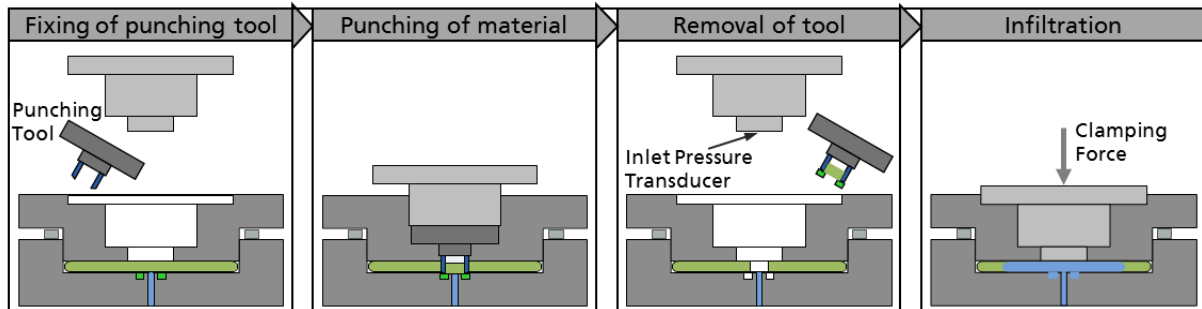


Figure 5.5: Procedure for punching a central hole through the reinforcement stack before infiltration

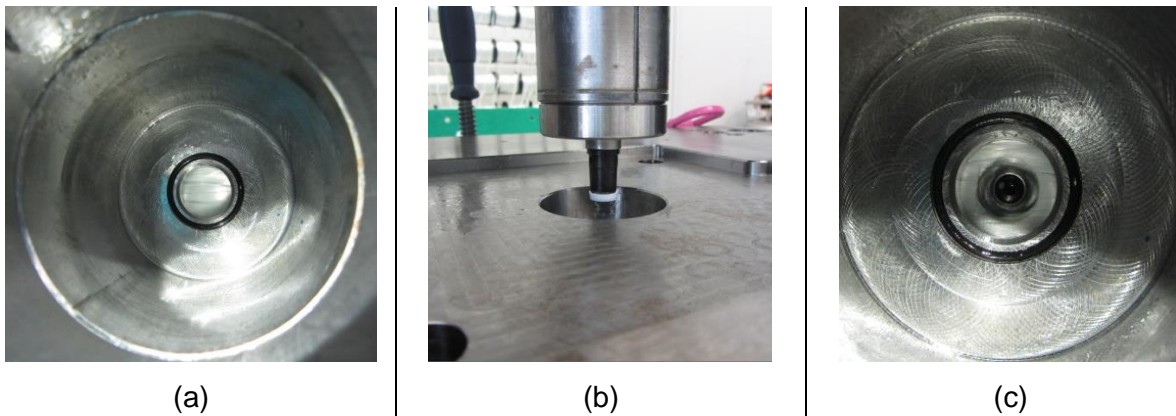


Figure 5.6: Cutting result into a roving fiber stack: (a) stack as seen from the top opening of the mold before cutting; (b) punching tool being lifted after cutting; (c) stack after cutting

Silicone oil was injected with constant pressure through the nozzle. Injection under constant pressure was achieved by a pressurized pot. The flow front was detected when reaching pressure transducers located at different positions within the cavity. Ten transducers were mounted to the mold. Pictures of the open mold are shown in Figure 5.7. The fluid was drained to a circular groove which defined the actual measurement cell as a circle with a diameter of 350 mm.

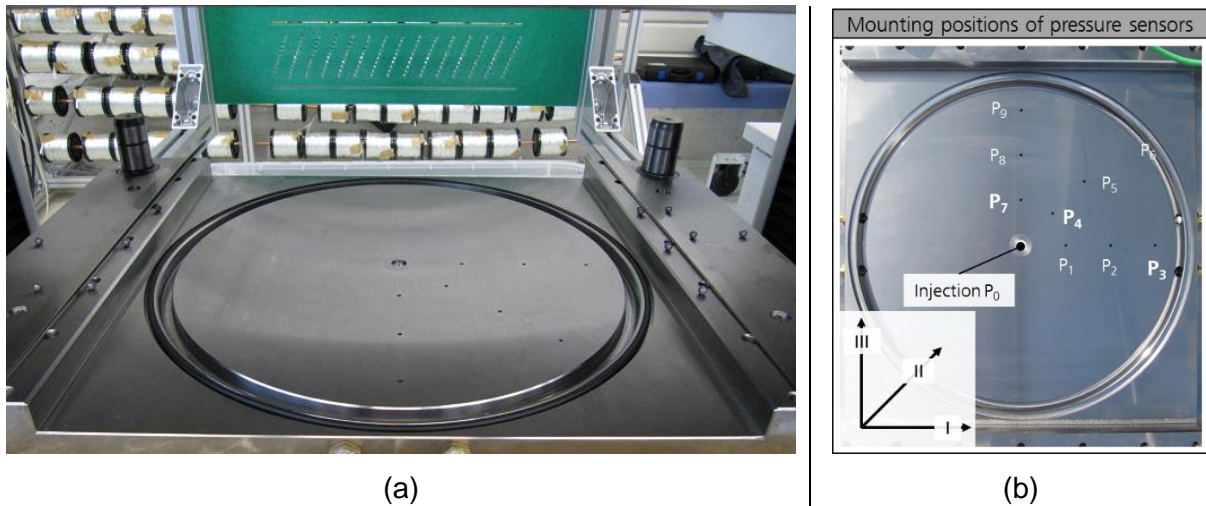


Figure 5.7: Permeability measurement cell: (a) open mold showing rovings guiding plate and side metal strips for fixing the cavity thickness; (b) top view of mold showing position of pressure transducer

The special sensitivity of the flow front detection method was previously assessed by comparing visual flow and transducer response, and was determined to be below 2 mm. This was the distance past the transducer location covered by the flow front when a pressure increase was detected [105].

5.1.3.1 Unsaturated flow condition

The suitability of the measurement mold and method was assessed by measuring the same glass fabric (Hexcel 01113) tested in a recent benchmarking exercise [64]. The analysis proposed by Weitzenböck et al [70] was employed to obtain the principal permeability parameters in-plane K_1 and K_2 , as well as the angle between the principal permeabilities and the axes of the coordinate system for unsaturated flow. The values found for K_1 (approximately $8 \times 10^{-11} \text{ m}^2$) and K_2 (approximately $2 \times 10^{-11} \text{ m}^2$) were within the range of values reported in the benchmark, thus validating the developed mold and method [106].

The permeability of CFM was measured for fiber contents of 17.1%, 21.9% and 24.1% vol. The fiber volume contents were chosen according to a compaction pressure range typically processed in pultrusion ($7 \times 10^4 - 4 \times 10^5 \text{ Pa}$). The material was cut from the roll to the mold dimensions and stacked to four pieces. The orientation relative to the roll was kept constant when stacking and laying into the mold (see Figure 5.13). A total of ten measurements were performed for each fiber volume. The injection pressure was set to 6 bar.

5.1.3.2 Saturated flow condition

To analyze measurement data according to the Weitzenböck method, it is necessary that at least one of the pressure sensors in the crosswise direction (P_7 in Figure 5.7 (b)) is reached before reaching the last sensor in the longitudinal direction (P_3). In this particular measurement cell, this means that data regression from unsaturated measurements is only possible if a maximum difference of one order of magnitude exists between K_1 and K_2 . This was not the case observed when measuring unidirectional roving layers.

Rovings were measured for the fiber volume contents listed in Table 5.5, defined by the adjusted cavity thickness. 300 roving ends were placed in the mold as shown in Figure 5.8. Compaction forces between 120 – 200 kN were applied to close the mold, depending on fiber volume content. The injection pressure was set to 1 bar for flow front measurements in the unsaturated state and then increased to up to 6 bar for saturated flow measurements. The inlet pressure was maintained until the system reached the steady state, i.e., no more pressure changes occurred.



Figure 5.8: Permeability mold with carbon fiber roving stack

A recurrent problem faced during measurements of roving stacks was that individual rovings which were cut (see Figure 5.6) shifted in position due to exerted fluid pressure. This effect narrowed the possible measurement window on rovings with this technique to approximately the range shown in Table 5.5. Shifting can be clearly detected during the measurement by an increase of pressure signals along the rovings in the longitudinal direction (P_1 , P_2 and P_3), and visually observed after the measurement. The effect was more intense when measuring stacks of carbon fiber rovings.

Regression of data from saturated measurements was executed by means of a procedure similar to that proposed by Arbter [72]. The absolute pressure values at different positions in

the cavity were used to determine the permeability in a saturated flow condition, i.e. in the equilibrium state. In order to find the permeability parameters, the steady-state flow was simulated in CFD software (Ansys CFX). The simulation model is shown in Figure 5.9.

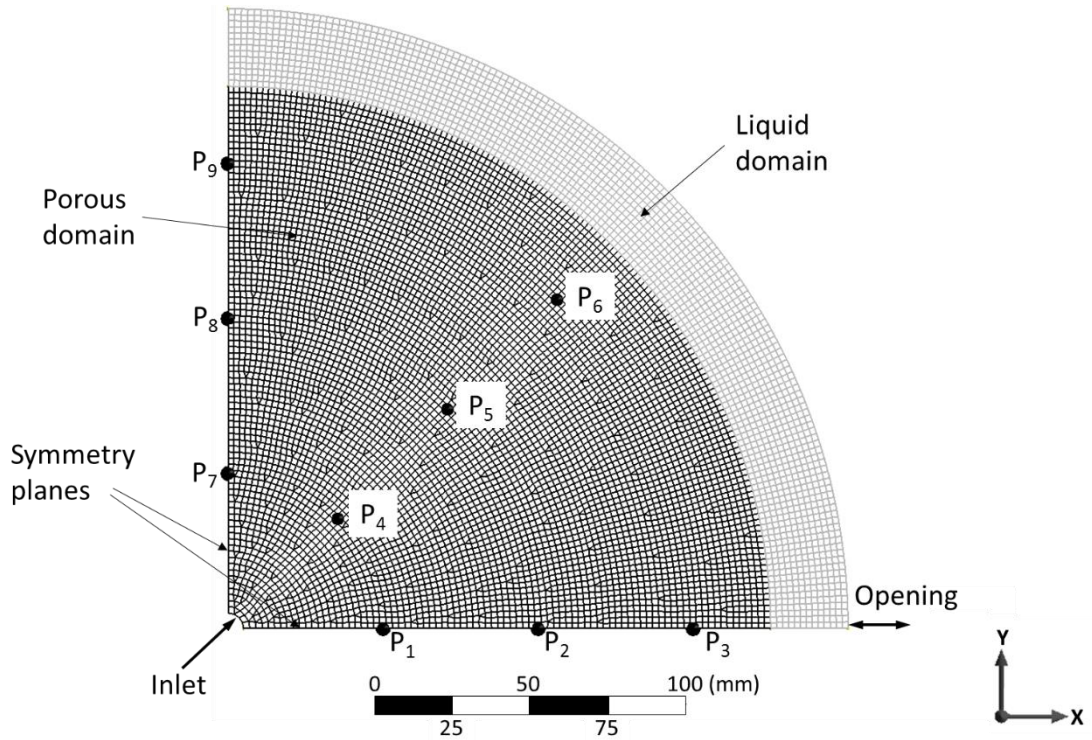


Figure 5.9: Simulation model for calculation of permeability parameters in saturated state

Initial permeability parameters were set as the initial values and the corresponding pressure field was then calculated. An optimization function was implemented to find K_1 and K_2 . The optimization function varied the values of K_1 and K_2 within a defined range and evaluated the minimum of the sum of squared residuals between three measured and simulated pressure values located in the principal axes x and y , and at an angle of 45° to the principal axes. Unless otherwise noted, the measured values of P_3 , P_4 and P_7 were taken as input values for the optimization function. The residual function was given by:

$$P_R = \min \left[\frac{1}{3} \sqrt{\left(\frac{P_{3,s} - P_{3,m}}{P_{3,m}} \right)^2 + \left(\frac{P_{4,s} - P_{4,m}}{P_{4,m}} \right)^2 + \left(\frac{P_{7,s} - P_{7,m}}{P_{7,m}} \right)^2} \right] \quad \text{Equation 5.2}$$

where the subscripts m and s denote measured and simulated values respectively. The optimization function minimized the averaged relative error between all pressure values measured and simulated. It was assumed that the directions of the principal permeabilities coincide with the reference axes, i.e. of $K_1 = K_x$, $K_2 = K_y$. This was a necessary assumption for this calculation method, and it was considered reasonable for a unidirectional fiber stack.

5.2 Compressibility measurement results

Measurements on rovings were performed in three different roving counts to evaluate the effect of the overall layer thickness on the compression behavior. Measurements on CFMs were performed on single and double layers to assess if a significant nesting effect could be detected. A mat/roving/mat laminate structure typically processed in pultrusion was tested to evaluate potential nesting effects. A list of the conducted tests is shown in Table 5.2. Curves of compaction pressure vs. fiber volume content for glass and carbon fiber roving layers are shown in Figure 5.10.

Table 5.2: Reinforcement layers configurations tested for their compressibility

Type of reinforcement	Number of specimens	Sample condition
GF Rovings	80 / 120 / 160	Dry
CF Rovings	80 / 120 / 160	Dry
CFM M8643	1 / 2	Dry / wetted out
CSM N720	1 / 2	Dry / wetted out
CFM - GF Rovings - CFM	1 - 80 - 1	Dry / wetted out
CSM - GF Rovings - CSM	1 - 80 - 1	Dry / wetted out

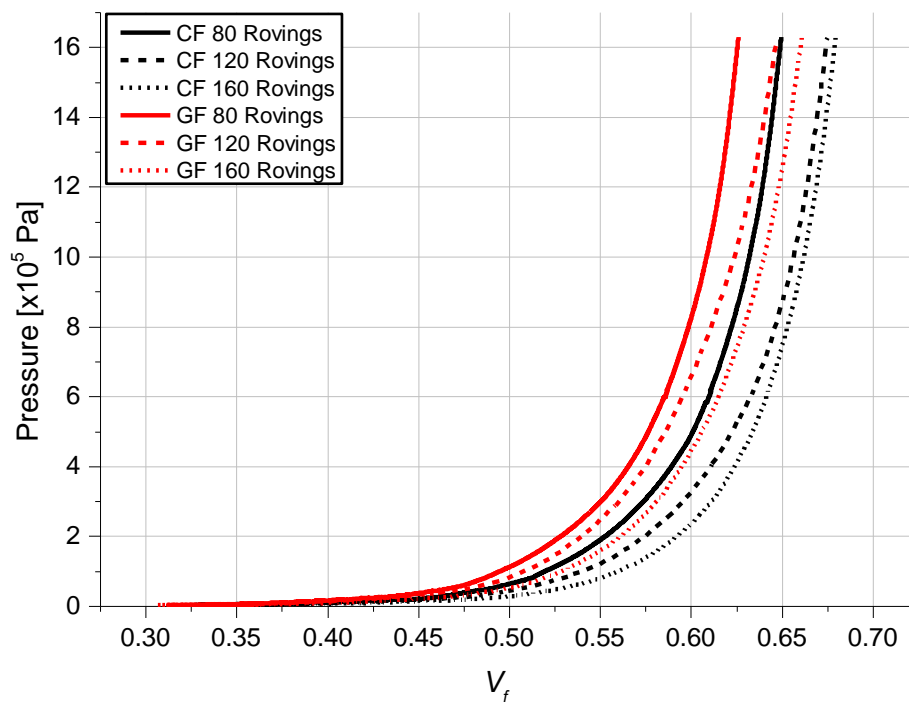


Figure 5.10: Curves of pressure vs. fiber volume content for fiber stacks composed of glass (GF) and carbon (CF) fiber rovings with different fiber counts

The compression behavior of rovings can be described as relatively insensitive to variations in the applied mechanical pressure, i.e. the stack is rather incompressible. This is due to the fact that fibers are already in a parallel orientation. A small variation in the number of rovings ends being fed to the pultrusion die can have a significant impact on processing stability. This implies that adding or removing a few rovings will have a significant impact on the mechanical pressure exerted by the die over the fiber stack. If the fiber volume content is too low, resin deposition is likely to occur in the die, if it is too high, pulling the bundle through the die will not be possible.

The compressibility of the roving stack was found to be dependent on the roving count. A larger number of rovings resulted in a higher fiber volume content for the same compression pressure applied. This was valid for both glass and carbon fibers. This can be explained by an increasing nesting effect of fibers intertwining within each other as the fiber stack gap increased.

The carbon fiber rovings were found to be more compressible and reach higher fiber volume content than glass fiber stacks for the same compaction pressure. This is probably due to different material conditioning and packaging. Carbon fibers are delivered twistless and spread-wound in cardboard rolls; glass fiber rovings, on the other hand, are delivered in packages from which the roving is pulled from the inside. This inevitably brings a periodic twist along the roving length. The carbon fiber filaments thus have a more parallel orientation within the roving, allowing for increased compaction.

Experimental data was fitted by the model proposed by Gutowski [61] (Equation 3.17). The values shown in Table 5.3 were used to calculate the bending stiffness of glass and carbon fibers. A value of 0.35 was used for V_0 in all cases. The fitted parameters β and V_a are shown in Table 5.4.

Table 5.3: Material parameters and calculated bending stiffness of fibers

	Carbon fiber	Glass fiber
Young's modulus [Pa]	2.4×10^{11}	8.2×10^{10}
Filament diameter [μm]	7	24
Area moment of inertia [mm^4]	1.89×10^{-9}	2.61×10^{-7}
Bending stiffness [N.m^2]	4.53×10^{-10}	2.14×10^{-8}

Table 5.4: Fitted parameters for roving fiber stacks according to the Gutowski's model

	Roving count	β [mm]	V_0	V_a	R^2
Carbon fiber stack	80	1.08	0.35	0.880	0.999
	120	1.27	0.35	0.878	0.997
	160	1.32	0.35	0.877	0.999
Glass fiber stack	80	2.54	0.35	0.871	0.998
	120	2.81	0.35	0.872	0.989
	160	3.09	0.35	0.872	0.996
CFM 3B M8634	-	0.80	0.10	0.977	0.999
CSM SF N720	-	0.03	0.05	89.57	0.999

The correlation coefficient values R^2 indicated that a good fit was obtained in all cases. In fact, good fitting results can be obtained for a range of pair values of β and V_a . The values shown in Table 5.4 were obtained by setting V_a to a narrow range while β was fitted. According to the theoretical framework proposed by Gutowski, the model assumes transverse fiber rearrangement during compression. This could result in a higher maximum possible fiber volume fraction V_a , or in a larger span length to span width ratio β . It is reasonable to assume that both effects occur simultaneously; rearrangement of fibers during compression may lead to changes in the packing distribution (between a square and a hexagonal array). It also leads to changes in the density of available contact points or scale of waviness within the beam network, which are described by the value β . According to this reasoning, it is expected that compressibility will be affected by the compression speed applied.

Constraining the value of V_a is, therefore, an arbitrary decision, as was noted by Gutowski. Nevertheless, it helps to evaluate the effect of roving count on the value of β . For a thicker fiber stack, the bulk of the material will have more rearrangement freedom during compression in comparison to a thinner fiber stack, thus resulting in a larger β . The values also indicated a larger waviness of glass in comparison to carbon fiber stacks.

Curves of compaction pressure vs. fiber volume content for the random glass fiber mats are shown in Figure 5.11. CFM and CSM, in contrast to roving layers, are generally more compressible, i.e. a variation in compression has a more pronounced effect on the fiber volume content in comparison to a roving layer. This property is effectively applied in pultrusion processing to extend the processing window by balancing variations in the roving layer. It is also noteworthy that the compressibility of the two apparently similar materials is

very different. The CFM from 3B reached a volume content of approximately 0.3 while the CSM from Superior Fibers reached approximately 0.21 for the same maximum compaction pressure of 1.64 MPa. The nesting effect was also more pronounced in the 3B CFM, as can be seen by the difference between the curves for single and double layers.

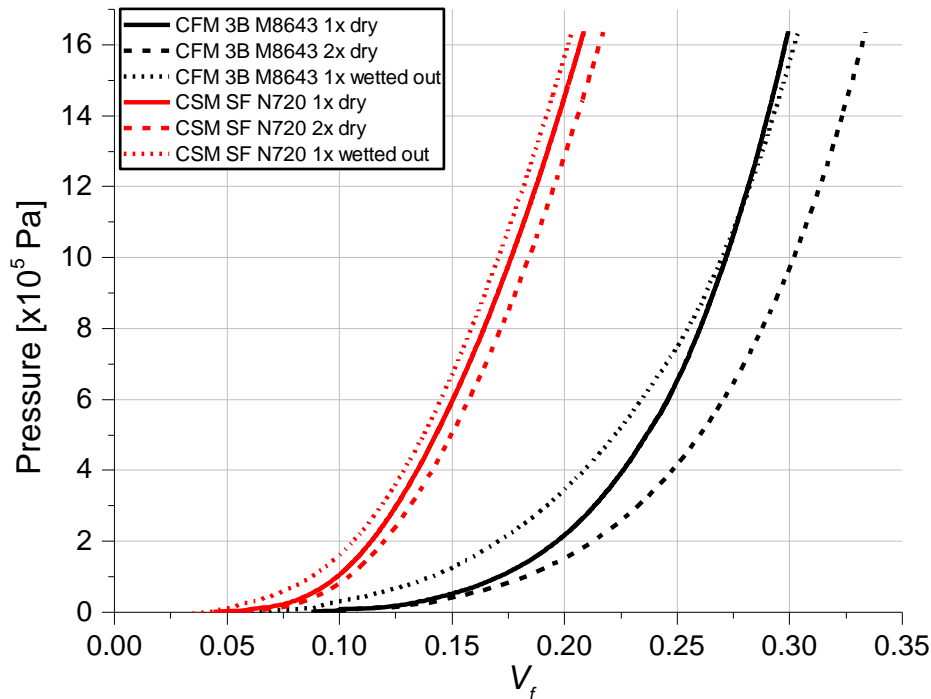


Figure 5.11: Curves of pressure vs. fiber volume content for single and double layers of glass fiber continuous mats

The fitting procedure was also applied to the mats. Fitted parameters are also shown in Table 5.4. Since the goal was to obtain a straightforward procedure for determining a reinforcement layup given the mechanical pressure and thickness, only the curves for single layers of the two mats in dry condition were fitted. In the case of mats, setting a value of V_a according to fiber packing makes little sense. Therefore, both V_a and β were fitted without any range constraints.

The nesting effect present in a multilayer laminate can also be evaluated by comparing the measured curve of laminate thickness (s) vs. compaction pressure (P) for a mat/roving/mat stack and the added curves of the same layers (see Figure 5.12). Due to nesting, there will be an error of about 5% – 10% in the cavity thickness (and consequently in the average fiber volume content) when using the single curves of the materials to calculate the multilayer laminate structure. In practical terms, a lower number of rovings will be determined than actually needed to achieve the same laminate thickness at the given compaction pressure.

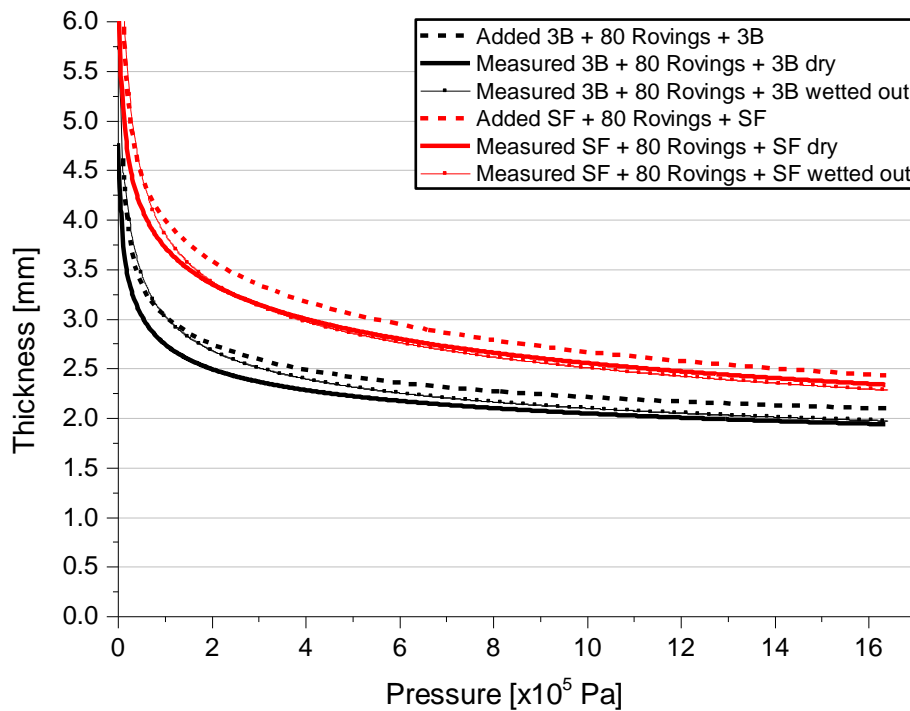


Figure 5.12: Curves of pressure vs. layer thickness for mat/roving/mat stacks

The effect of wetting out the reinforcement was also investigated. For low pressures (0 - 0.1 MPa), the curve for wetted reinforcement was close to the theoretical curve of added layers. That means that at this pressure range, wetting-out of reinforcement compensated the nesting effect. For the pressure range up to 0.6 MPa, the compressibility curves of the wet-out and dry reinforcement became close to each other, as the compaction pressure effectively squeezes out the soaking fluid. In this pressure range, the error incurred by adding up the layers must be considered. It should be noted however, that a dependence between profile structure and the deviations discussed above was expected, for example in the case of a thick laminate (over 4 mm) in which more than 2 layers of CFM are present, or when working with a resin of different viscosity.

When designing a reinforcement layup, one must know beforehand a suitable range of mechanical pressure, which must be experimentally determined. According to experience from pultrusion experiments in the pultrusion lab at Fraunhofer, typical compaction pressures for a mat-roving-mat stack range from 0.5 to 4.0 bar. Higher pressures will cause tearing of the mats [107]. As an example, for a compaction pressure of 2.4 bar and a laminate thickness of 3.0 mm, a glass fiber roving layer would consist of 118 rovings, if the top and bottom mats are 3B M8643, or 73 rovings in combination with SF N730 mat layers. This calculation example illustrates the significant impact of the chosen reinforcement on the layup design.

5.3 Permeability measurement results

Results obtained from unsaturated flow measurements within CFM stacks and saturated flow measurements within unidirectional roving stacks are presented in this section. The results obtained from measurements on rovings are compared to predictions from a theoretical model, and the validity and limitations of the developed characterization technique are discussed.

5.3.1 Continuous filament mats

The permeability measurement results for the CFM stacks are shown in Figure 5.13.

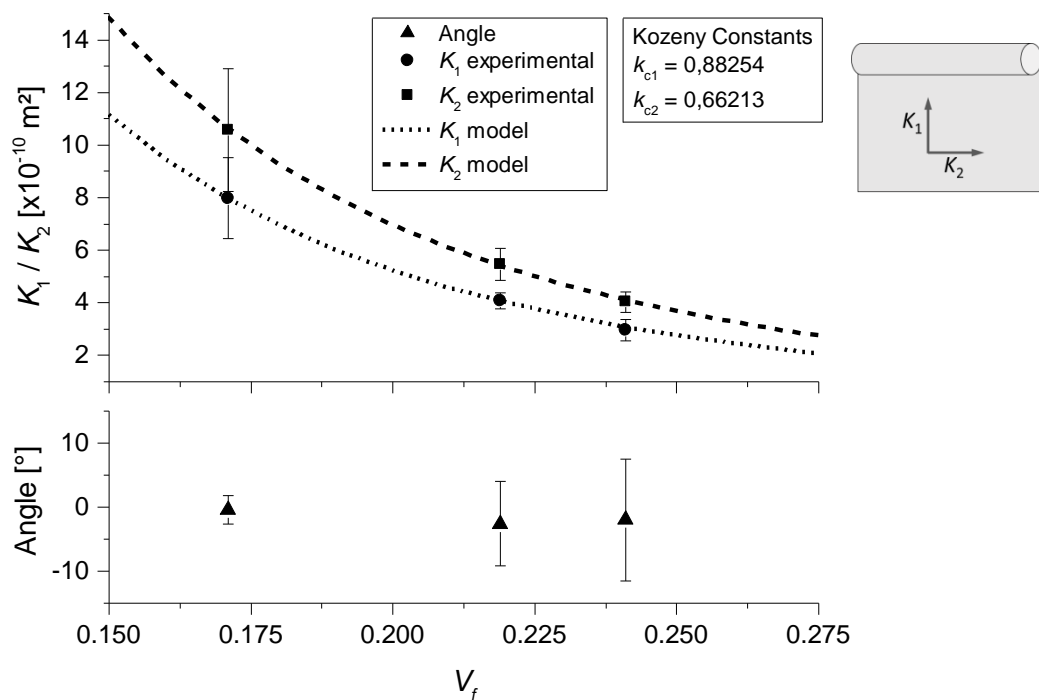


Figure 5.13: Results of permeability measurements on CFM stacks. Top: permeability parameters in the plane directions; bottom: calculated angle between the principal permeabilities and the reference plane directions

It is interesting to note that with increasing fiber volume content, the accuracy of the measurement clearly improves for both K_1 and K_2 . One possible explanation for this behavior might be the fact that for lower volume contents, the fluid flows not only through the bulk region of the mats, but also to some extent between the mat and the mold walls. These local variations may be suppressed when the fiber stack is subjected to a higher compaction pressure, resulting in flow only through the porous material.

On the other hand, the scattering of the determined angle between the principal permeabilities and coordinate system increased with increasing fiber volume content. This might arise from the inherent fluctuation of specific weight in CFM materials. A specific weight with $\pm 10\%$ fluctuation is typically declared for this kind of material. These local variations may result in scattering on the orientation of main permeabilities between the measurements. In contrast to the general assumption that CFM is an isotropic material, a subtle, though discernible anisotropic permeability was observed, with the permeability in the transverse direction relative to the roll winding direction higher than in the parallel orientation.

The experimental data was fitted to the Kozeny-Carman model (Equation 3.19). The fiber radius was set to $12\ \mu\text{m}$, a typical value of glass fibers. The fitted curves are shown in Figure 5.13. This allowed the prediction of the permeability of a CFM layer given a particular laminate and compaction pressure. It must be stressed once again that these results are intrinsic to the particular M8643 CFM material only.

5.3.2 Roving stacks

Measurements of roving stacks showed a higher degree of anisotropy than predicted by models such as proposed by Gebart [74], and experimentally determined by Schell et al. [78]. These studies presented, for a bundle of parallel oriented fibers, a difference between the longitudinal and the transverse permeabilities of around one degree of magnitude. Such a difference lies within the limits of the measurability by the method of Weitzenböck et al. [69] and the mold configuration. Higher degrees of anisotropy, however, resulted in the testing fluid reaching the third pressure transducer in the longitudinal direction before the first transducer in the transverse direction. This flow behavior prevented an analysis of the unsaturated flow condition.

For the saturated flow, it was necessary that a steady state was reached, in which the pressure distribution over the measurement region no longer varied with time. Typical pressure distributions such as shown in Figure 5.14 were obtained. It can be seen that a long time was needed to reach steady state; after setting the pressure to 4,4 bar at the inlet, more than 1.5 h were needed for the fluid to reach P_7 , and steady state was reached after 3.5 h. The inlet pressure was then increased to 6.0 bar after 4.2 h of measurement, to obtain another pressure distribution for the same fiber volume content.

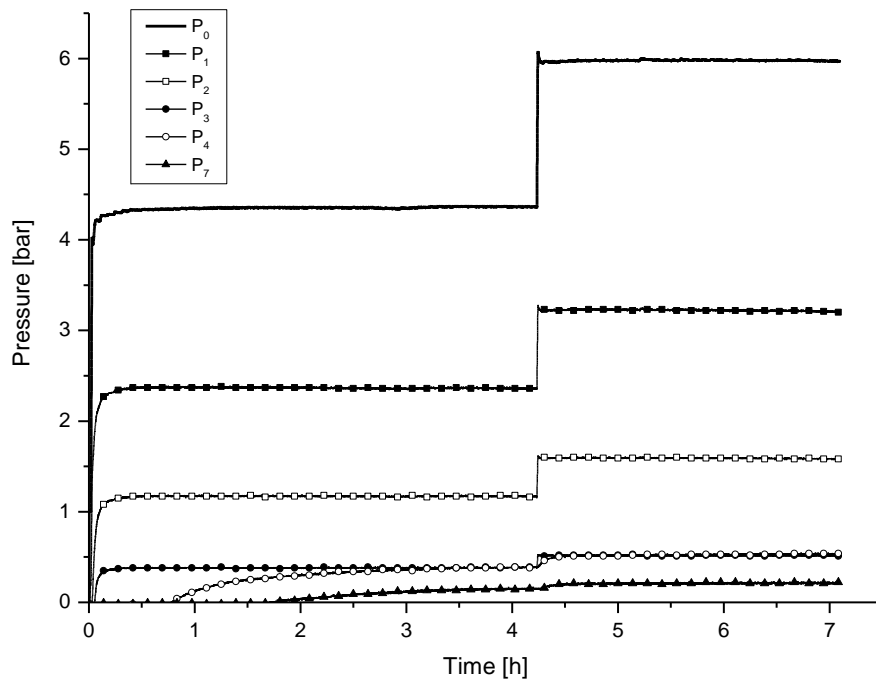


Figure 5.14: Pressure distribution inside the permeability mold during a measurement of a glass fiber stack with 65,4% vol. in saturated flow condition, refer to Figure 5.7 (b) for pressure locations

The permeability parameters were obtained by an optimization function implemented in the Ansys CFX Workbench (see Section 5.1.3.2). A comparison between pressure measurements along the x -axis and y -axis and the curves obtained from the simulation procedure is shown in Figure 5.15, corresponding to the two pressure levels at steady state in Figure 5.14. It can be seen that the predicted curve along the x -axis approached the measured value only for the sensor P_3 , since the values of P_1 and P_2 were not considered in the optimization function. One of the reasons for this decision was that pressure measurements close to the injection nozzle, where pressures were higher, were more susceptible to errors due to local fiber shifting. Furthermore, from the pressure sensors located along the y -axis and along the diagonal (direction II in Figure 5.7 (b)), only P_4 and P_7 were reached by the fluid and showed a pressure signal.

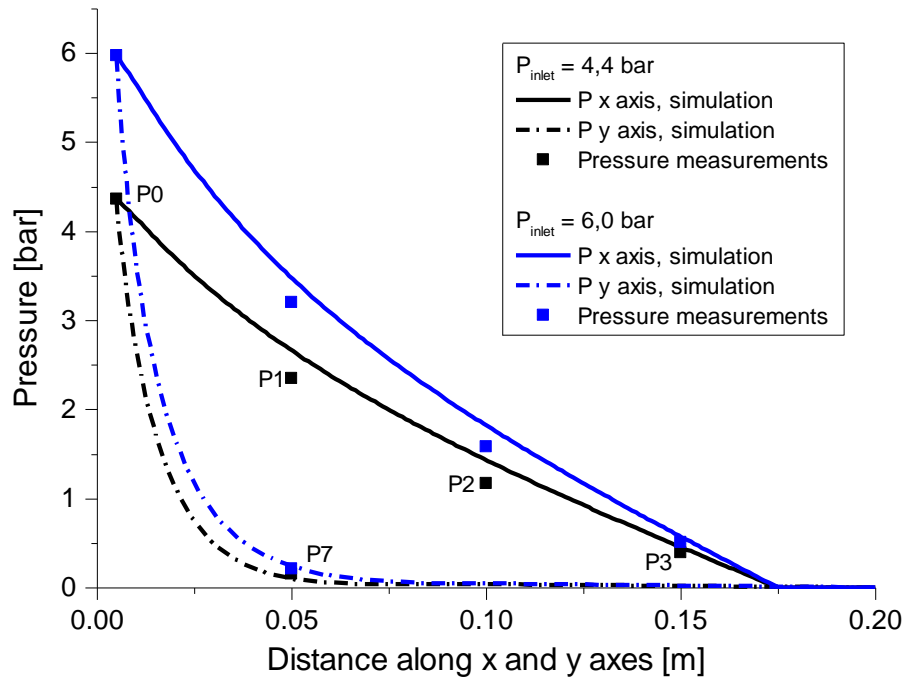


Figure 5.15: Comparison between measured pressures and curves predicted by simulation

The results obtained are listed in Table 5.5. For the glass fiber stacks, six measurements were evaluated for each fiber volume content. For each of them, the optimization procedure was conducted to obtain a value of K_1 and K_2 . The P_R value shown is an average from the residuals calculated in the optimization procedure. Measurements performed on carbon fiber stacks showed no response from pressure sensor P_7 . The optimization was then conducted using only the measured values of P_3 and P_4 . For the 62,4% vol. case, only two measurements led to a steady state and could be evaluated because of repeated fiber shifting. Therefore, no standard deviation is shown for this measurement point. The results were compared with the predicted permeabilities according to the Gebart's model [74] (Equation 3.19 and Equation 3.20). The results of the glass fiber stack measurements are shown in Figure 5.16, and for carbon fiber stacks in Figure 5.17.

Table 5.5: Results of permeability measurements on roving stacks

	V_f	K_1 [m ²]	K_2 [m ²]	P_R
Glass fiber stack	0.595	$(4,8 \pm 0,1) \times 10^{-12}$	$(5,4 \pm 0,9) \times 10^{-14}$	0,16
	0.654	$(2,4 \pm 0,1) \times 10^{-12}$	$(2,5 \pm 0,8) \times 10^{-14}$	0,17
Carbon fiber stack	0.624	$1,4 \times 10^{-12}$	$2,0 \times 10^{-15}$	0,13
	0.655	$(7,0 \pm 3,9) \times 10^{-13}$	$(1,6 \pm 0,6) \times 10^{-15}$	0,24

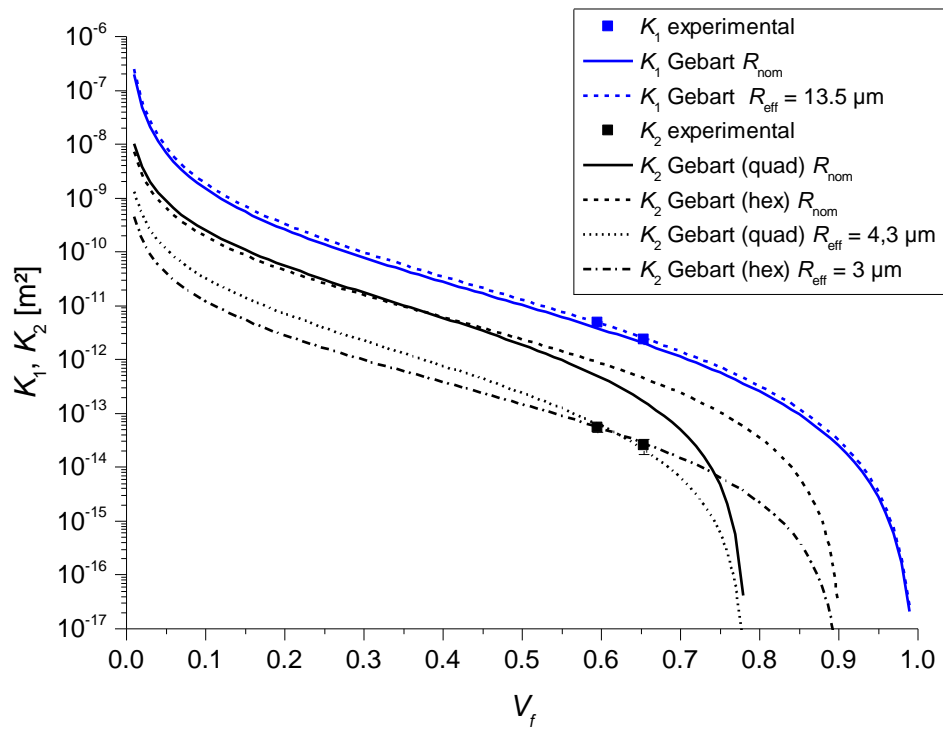


Figure 5.16: Comparison between permeability results on glass fiber stacks and values predicted by Gebart's model

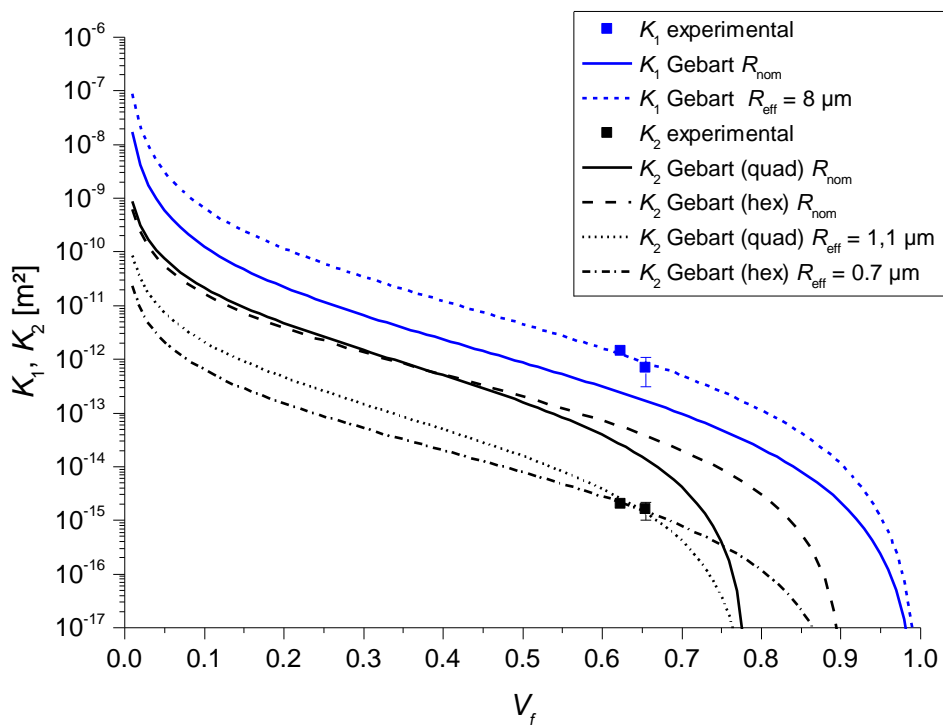


Figure 5.17: Comparison between permeability results on carbon fiber stacks and values predicted by Gebart's model

The results of the longitudinal permeability K_1 from measurements on glass fiber stacks showed a good agreement with the values theoretically predicted. As proposed by Gebart,

an “effective fiber radius” was chosen to superpose the model curve to measured data. Only a minor correction relatively to the nominal radius of 12 μm was needed for this case. The discrepancy in the carbon fibers case was slightly larger. For the longitudinal permeability, the measured permeability was higher than the model prediction for the carbon fiber nominal radius of 3.5 μm .

For the transverse permeability, a much larger deviation of up to one order of magnitude from the model was observed for the glass fibers. It should also be noted that, in the fiber volume content region considered, the model predictions considering a quadratic and a hexagonal fiber packing diverge from each other. This resulted in different effective fiber radii needed to superpose model and measurement results and consequently in different predicted values in the lower fiber volume region.

The large discrepancy in the transverse permeability might be due to an imperfect parallel orientation of the fibers. Stacked rovings created regions with higher volume content, which effectively prevented transverse flow. Twisting and undulations are characteristic and clearly discernible in direct glass fiber rovings, which might contribute to obstruction of the flow. Furthermore, these characteristics made a perfect stretching of the fibers more difficult, accentuating the problem of fiber stacking. Nevertheless, the measurement assembly reproduces to a large extent a typical configuration of a pultrusion die in-feed. The experimental results obtained are thus considered to be representative of flow conditions through a roving layer prevailing in pultrusion processing.

The method developed here has, nevertheless, limitations regarding the measurement of a unidirectional fiber stack. The measurable fiber volume content region was very narrow between a lower limit where fiber shifting in the cut region is unavoidable, and an upper limit where no pressure is detected in the direction transverse to the fiber orientation. The extrapolation of results to lower fiber volume fractions shown in Figure 5.16 and Figure 5.17 should, therefore, be considered with caution. The method was time-consuming due to the large amount of rovings threaded prior to each measurement. Furthermore, an analytic solution would be preferred over the optimization approach, e.g. according to the method proposed by Han et al [71], which was not possible with the method and material considered due to the very low volumetric flow rate of the permeating fluid. The analytic solution would allow a proper error propagation analysis and therefore a strict quantitative evaluation of the method. In the presented stage of development, the method is only suitable for a qualitative assessment of permeability.

6 Experimental trials with closed injection dies

To compare experimental data to processing simulation results, a series of trials was conducted using two pultrusion dies with closed injection and impregnation chambers. One of the dies had a design based on the description contained in Brown's patent [8]. This die design is referred to as conical. The other die had a design according to Koppernaes [6] and is referred to in this study as tear drop.

The pultrusion machine used for the trials was a model Px500-10T (Pultrex Ltd., Essex, UK), corresponding to the current state of the art. The pulling device consisted of a pair of alternating pullers. Each puller was fixed to a linear track and coupled to an electro-mechanical gear based on a ball screw mechanism, which could precisely control the linear speed. The hub of each puller was approximately 50 cm. The material being processed was pulled by one of the pullers until close to the end of the hub, when the second puller then clamped the profile and traveled at the same speed of the first one until the latter one reached the end of the hub and released the profile.

The mixing and metering machine (model type Nodopur VS, Tartler GmbH, Michelstadt, Germany) was a system designed for processing of two-component polyurethane resins of low to medium viscosity. The system had two separate tanks for storing the two resin components. The metering was done by gear pumps with volume flow meters at their discharges. The pump throughput was continuously controlled by a proportional–integral–derivative (PID) controller according to the measured volume flow. Gear pumps have the advantages of very precise metering and of pumping constant throughputs regardless of the counter-pressure at the discharge (up to a certain limit given by the gear motor).

Trials were conducted with each die by processing unidirectional fiber stacks composed of carbon and of glass fiber rovings. Rovings processed were the same grades characterized in Section 5, i.e. glass fiber direct rovings 399A-AE 4.800 tex and carbon fiber rovings Sigrafil C30 50k. The resin formulation processed was the same described in Section 4, that is, the Daron ZW 015864 resin formulated with curing agent, catalysts and processing additives.

The die was heated by means of electrical heating plates. The temperatures were controlled by thermocouples located in the die body, drilled close to the inner cavity. Processing temperatures were adjusted to partially cure the material to reach a B-stage condition in the pultrusion die. The set temperature was equal for all heating zones in a particular trial.

The processing parameters varied were the pulling speed and fiber volume content. Processing data recorded throughout the trial included:

- Pulling speed (real time speed)
- Pulling force
- Temperature at different positions along the length of the metal die
- Power input to the electrical heaters (percentage value of nominal output)
- Pressure in the liquid region of the die
- Pressures at the discharge of the resin mixing and metering unit (injection pressure)
- Resin mass flow rate

Additionally, the temperature within the processed material was measured by letting a wire thermocouple to be pulled together with the fiber bundle over the entire die length. This allowed for getting a temperature profile as the resin (partially) cures along the die. A summary of the conducted trials is presented in Table 6.1.

Table 6.1: Summary of conducted pultrusion processing trials

	Trial number									
	1	2	3	4	5	6	7	8	9	10
Pultrusion die *	C	C	C	C	C	C	TD	TD	TD	TD
Fiber stack **	GF	GF	GF	CF	CF	CF	GF	GF	GF	GF
Pulling speed [m/min]	0.3	0.3	0.3	0.5	0.3	0.3	0.5	0.3	0.3	0.3
Fiber volume content [%]	0.64	0.6	0.57	0.64	0.64	0.6	0.64	0.64	0.6	0.64
Set Temperature [°C]	100	100	100	100	100	100	100	100	100	80

* C = conical; TD = Tear Drop

** GF = glass fibers; CF = carbon fibers.

6.1 Description of trial assemblies

In this section, both dies applied during the experimental trials are presented, in terms of their working principle, mechanical assembly, temperature management by means of cooling and heating plates, and integration of temperature and pressure sensors. Their similarities and differences related to processing are also briefly described.

6.1.1 Conical die

The pultrusion die with conical injection and impregnation chamber consisted in fact of a standard die, i.e. a die with a straight inner cavity of constant cross section, in this case a flat sheet of 90.0 x 4.0 mm². The die length was 1220 mm. The conical injection chamber is mechanically aligned and fixed to the main die. The chamber had 500 mm of length, and a tapering angle of 1°. A guiding plate was bolted directly to the inlet of the injection chamber. Its primary function was to uniformly distribute the rovings over the cross section. By separating them, it also facilitated flowing of resin between rovings in the cross-wise direction. The resin formulation was injected through four nozzles (two located each at the top and bottom) at a distance of 200 mm from the chamber inlet. An opening to the atmosphere located at 110 mm from the chamber inlet (center, opening length 50 mm) allowed for observation of the flow front. This design had proven to give good results on the processing of reinforcements stacks consisting of rovings only. A schematic representation of the die assembly is shown in Figure 6.1.

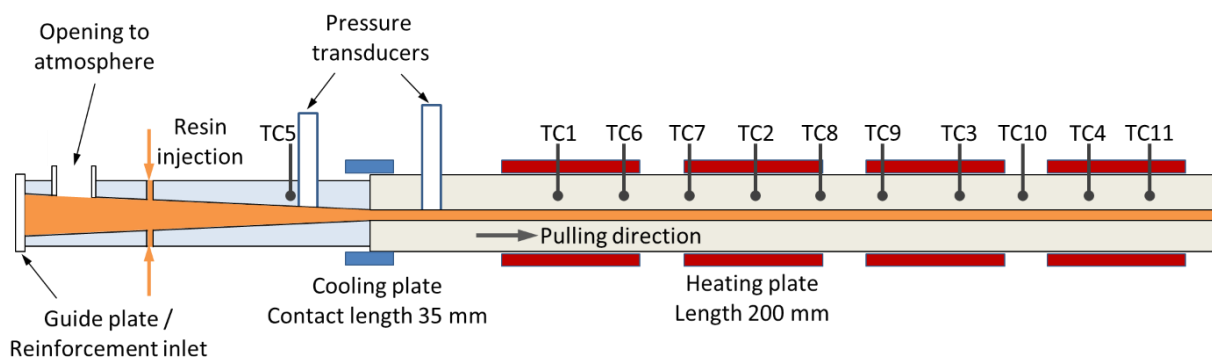


Figure 6.1: Schematic representation of die assembly with conical inlet geometry

A particular advantage of this design over the tear drop is that no stagnation regions with long resin residence time are formed. On the other hand, processing of profiles with more complex reinforcement layups may be more challenging, depending on the type of reinforcements and stacking sequence [1].

Two pressure sensors (Dynisco SPX2292, measurement range 0 – 70 bar) were located near the end of the conical section and at the beginning of the straight section. These sensors had a relatively large membrane surface (diameter of approximately 23.5 mm) and are thus appropriate to measure an average pressure while in contact with the fiber stack.

A total of eleven thermocouples measured the temperatures along the die. Four of these were used as control values for the set temperatures in four heating zones located along the

die main body (TC1 to TC4). Each heating zone consisted of one electrical heater fixed at the top and one at the bottom of the die. The nominal power of heating cartridges in each plate was 1000 W, and the contact area was 200 x 80 mm². A pair of cooling plates was fixed at the top and bottom at the junction between the tapered chamber and the straight die. The die and the injection chamber did not have the same thickness, therefore the contact length of the cooling plates was reduced (see Figure 6.1).

6.1.2 Tear drop die

The die with tear drop geometry evaluated in the trials was designed and manufactured as a die specific for closed injection pultrusion, i.e. the injection and curing sections are milled from a single piece of tool steel. The inner cavity in the straight section had dimensions of 180 x 2.45 mm². The inlet had a length of 100 mm and the same cross section as the curing section. It was followed by a conically constraining injection and impregnation region with 320 mm length and tapering angle of 1.2°. This corresponded to a maximum cavity height of 8.0 mm at the position 116 mm (distance from die inlet), where the resin was injected. Injection was done through three nozzles at the bottom and another three nozzles symmetrically arranged at the top side of the die. The total die length was 1318 mm. A guiding plate was also used for positioning the rovings prior to entering the die; however, it was not attached to the die as in the conical die assembly, but fixed at a distance of about 400 mm from the die inlet. The hole configuration was like the sketch shown in Figure 5.2.

As stated previously, this die design is susceptible to stagnation regions with long resin residence times. Stable operation over several hours is highly dependent on a proper die design which avoids such stagnation region and at the same time assures thorough wetting out of reinforcements. Furthermore, it is dependent on resin reactivity. This design was found to be suitable for processing of standard resin formulations with long pot life at room temperature such as vinyl ester [12].

Similarly to the conical die, pressure transducers were mounted in the die, located near the resin injection points and at the beginning of the straight curing section. During operation, the pressure value at the first transducer was an important monitoring parameter that indicated whether the chamber was full of liquid material. To ensure that the chamber was full at all times, the flow rate was adjusted such that an excess of resin flowed out of the die inlet.

Nine thermocouples measured the temperatures along the die. Three of these were used as control values for the set temperatures in three heating zones located along the die main

body (TC1 to TC3). Each heating zone consisted of two electrical heaters (same type employed for the conical die) fixed side by side at the top and two at the bottom of the die. A pair of cooling plates was fixed at the top and bottom at the end of the tapered section. A sketch of the trial assembly is shown in Figure 6.2.

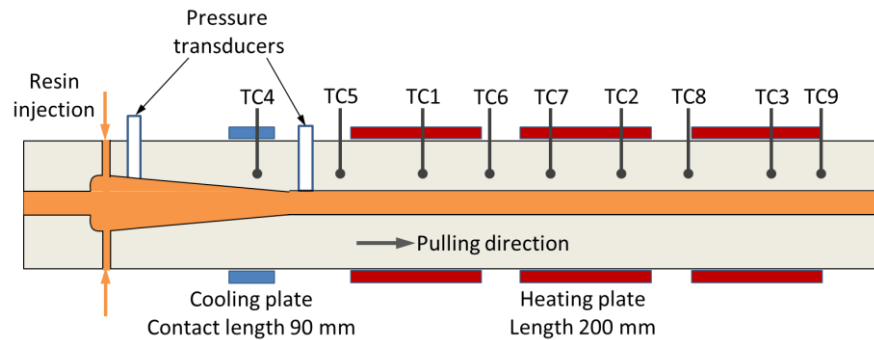


Figure 6.2: Schematic representation of die assembly with tear drop inlet geometry

6.2 Experimental data

Examples of processing data obtained from the experimental trials with both dies are presented and analyzed in terms of their significance to processing in this section. Qualitative correlation between processing parameters is also discussed. The focus is given to data relevant for comparison and validation of the simulation studies conducted in Section 7.2. A summary of data obtained for the different trial configurations (see Table 6.1) is given in Appendix A.

6.2.1 Conical die

Temperature profiles along the die are shown for the trial configuration 1 (see Table 6.1) in Figure 6.3. The exothermic heat generated by the B-staging reaction leads to an increase in temperature above the set temperature of the heating zones up to approximately 115 °C between heating zones 1 and 2. This can be observed both by the signals of the wire thermocouples as well by the value of the monitoring thermocouple located at the x-position 870 mm. A slight difference in the temperature development can also be seen between the profile center and surface. By comparing both curves, one can conclude that the overall reaction heat generation is moderate; otherwise, an increase in the center temperature above that of the surface would be observed.

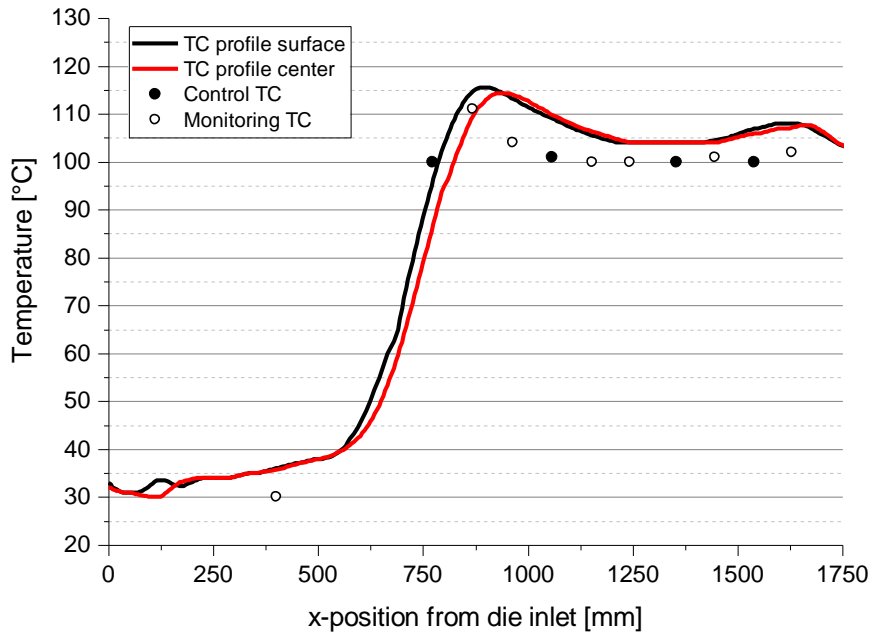


Figure 6.3: Temperature profiles in the conical die assembly (trial configuration 1) obtained from wire thermocouples fed through the die and from thermocouples positioned in the die

No significant difference in the temperature profiles was observed when processing carbon fiber rovings instead of glass fibers. Variations of fiber volume content did not result in differences in the temperature profiles either. By increasing the pulling speed to 0.5 m/min, a lateral shifting of the curves along the x-position took place, while the maximum temperature reached remained at a similar level.

During all trials, no completion of the reaction to a fully cured material was observed. Whether the temperature development led to an incipient radical polymerization cannot be determined from the experimental trials and product appearance alone. According to the prediction shown in Figure 4.4, the second reaction step initiates after approximately 5 min at a constant temperature of 120 °C. However, the prediction by the Thermokinetics software does not take into account the mass and local temperature increase in the material. A spatial or volumetric simulation is expected to give a better estimation of the real material state by the end of the pultrusion process in this case.

The individual temperatures of the control and monitoring thermocouples were kept stable at the values shown in Figure 6.3. This was due to the high specific heat capacity of steel. The power input to the electrical heaters is logged by the machine as a percentage of the nominal heater power. These values are shown in Figure 6.4 as an example for the same time span

of 20 min during which the data shown in Figure 6.3 was obtained. The signals of the thermocouples 1 through 6 are also plotted.

The temperatures of the control zones were constant at approximately 100 °C at all zones, and the temperatures of the thermocouples 5 (located at the injection chamber) and 6 (exothermic peak located after the thermocouple 1) were also at a constant level. The power input values, on the other hand, varied over time. The calculated average values over the time span are indicated in the graph. The heat needed to trigger the reaction was transferred solely by zone 1. Zone 2 was only sporadically turned on, which was due to the heat generated by the reaction and subsequent heat build-up between zones 1 and 2. Towards the downstream portion of the die, zones 3 and 4 were again contributing with a net heat input to maintain the set temperature after the exothermic reaction heat generation had subsided.

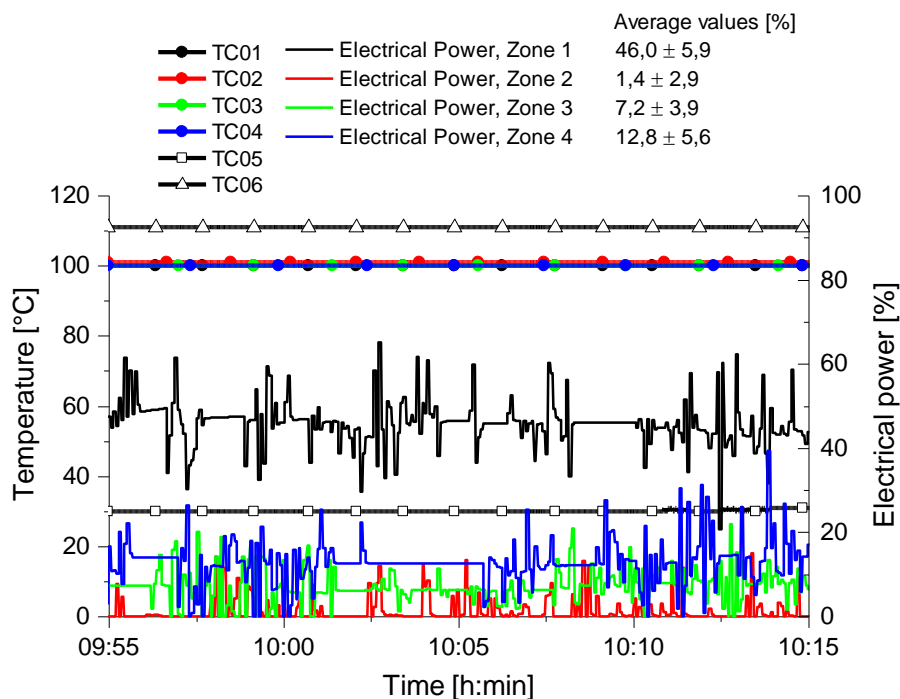


Figure 6.4: Thermocouple signals and power input to the electrical heaters over a 20 min time span during trial configuration 1

The signals of measured pulling force, pulling speed and liquid pressures are shown in Figure 6.5. In contrast to the temperature signals, these processing parameters undergo to some extent strong variations over time, in particular the pulling force and the pressure transducer 2 (located at the beginning of the straight die section). In comparison, the pressure measured by the transducer 1 (in the tapered die inlet) showed smaller absolute variations, although the perceptual variation of all signals lied around 10%. The resin was

injected at a low pressure (0.4 bar). An injection pressure was only recorded when the metering unit was pumping resin. The injection was thus intermittent, because the minimum flow rate was too large relatively to the throughput needed for the specific combination of die cavity, fiber content and pulling speed.

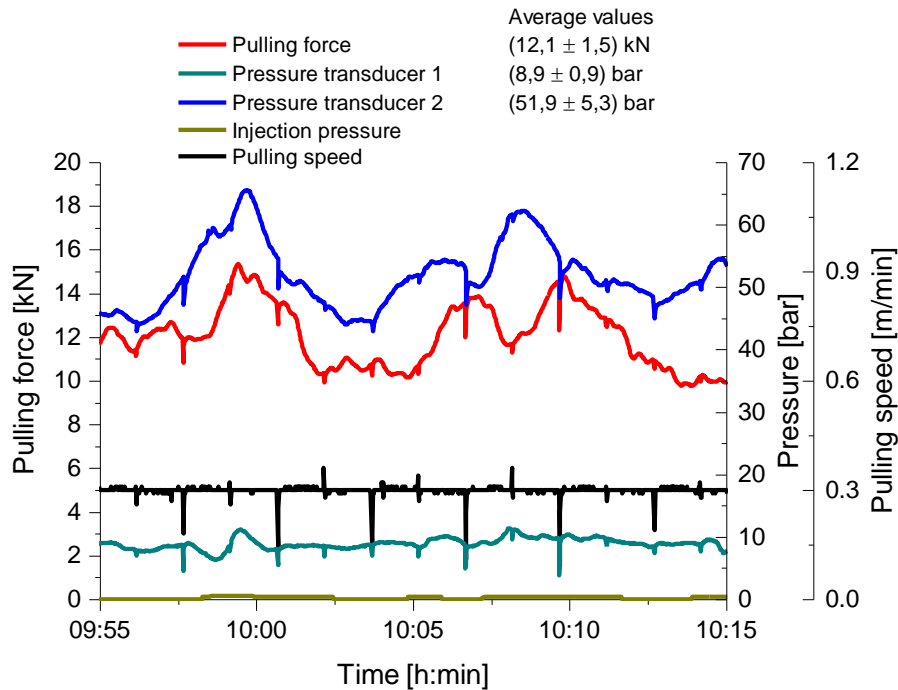


Figure 6.5: Plots of measured pulling force, pulling speed and liquid resin pressures over a 20 min time span during trial configuration 1

Short drops in the pulling speed occurred periodically, which also caused corresponding drops in the pulling force and pressure signals. This is due to the pulling mechanism composed of alternating pullers, and is related to the handover of one puller to the other. Furthermore, a correlation existed between the level of pulling force and the pressures measured in the liquid region, especially the peak pressure at the conical-straight transition region. This suggests that the pulling resistance in the processing trials was caused, to a considerable amount, by the pressure of liquid resin over the die walls, which can be expressed by Equation 3.33.

The large variations observed in the signals in Figure 6.5 are to some extent caused by the intermittent injection. The resin injection was manually turned on and off, by observing the flow front position at the opening to the atmosphere. The variation in the flow front position could already cause a pressure variation. Another hypothesis for the fluctuations could be a deformation of the die inner cavity due to the high pressures developed in the process. With increasing pressure, the deformation would be accentuated in terms of cavity expansion,

resulting in a counter effect of lower fiber content and pressure release. This undesirable effect has been observed in the industry by direct measurement of the die outer dimensions during processing, and by variations in the product thickness. This phenomenon has been referred to as a “breathing die” and can be reduced or eliminated by designing a more massive die body.

6.2.2 Tear drop die

The resin processed in this study had a short pot life typical of polyurethane reactive systems which are activated upon mixing (see Section 4). The pot life at room temperature, i.e. the time up to which the resin can be processed, was approximately 15 min. During long trials (over 4 hours) with the tear drop die, a deterioration of profile quality was observed, which is attributed to clogging of the chamber. This was accompanied by an increase in the injection pressures needed due to obstruction of the chamber and injection lines. After a long trial, the chamber was completely obstructed by B-staged material (see Figure 6.6). This particular die design is therefore unsuitable for this combination of processing conditions and the fast curing resin formulation applied in this study; a design optimization would be necessary for a potential application in series production.

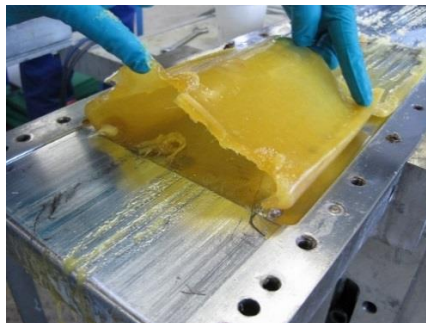


Figure 6.6: Tear drop chamber filled with B-staged resin after a trial

Figure 6.7 shows temperature profiles during trials with the tear drop die assembly under the trial configuration 9 (see Table 6.1). Some differences can be stated in comparison to the temperature profiles developed in the conical die (Figure 6.3). During the resin heating up, the thermocouples mounted in the die measured the same value as the profile itself. The exothermic peak temperature was also lower at approximately 112 °C. This is explained by the fact that the die body thickness was smaller than that of the conical die, therefore leading to a faster heat transfer into the processed material and also faster dissipation of generated reaction heat. The difference between the signals of the wire thermocouples fed through the profile center and surface was also less accentuated, which is due to the smaller profile thickness.

Surprisingly, the cooling of the injection and impregnation region seems to be more effective in the tear drop than in the conical die assembly. This can be seen by comparing the beginning part of the temperature profiles in Figure 6.3, in which a temperature increase is already measured at the very beginning and in Figure 6.7, in which the temperature remains approximately constant up to an x-position of 400 mm. Since the tear drop has an integrated injection and impregnation cavity, one would expect heat conduction to the upstream section of the die. However, the larger contact area of the cooling plate (see Figure 6.1 and Figure 6.2) and the smaller die body mass result in a more effective heat dissipation in this die.

The difference in the die body mass can also be ascertained by the small fluctuations in the temperature signals over time shown in Figure 6.8. Similarly to the observations made for the conical die, a heat accumulation between heating zones 1 and 3 took place in this trial assembly, where the reaction rate reached its maximum. Therefore, the heating zone 2 did not contribute substantially with heat input to the die.

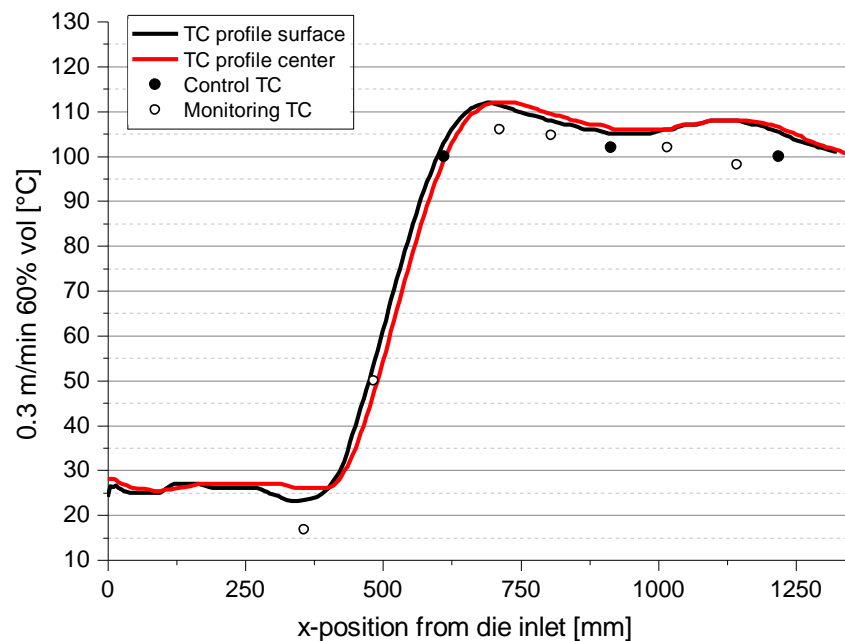


Figure 6.7: Temperature profiles in the tear drop die assembly (trial configuration 8) obtained from wire thermocouples fed through the die and from thermocouples positioned in the die

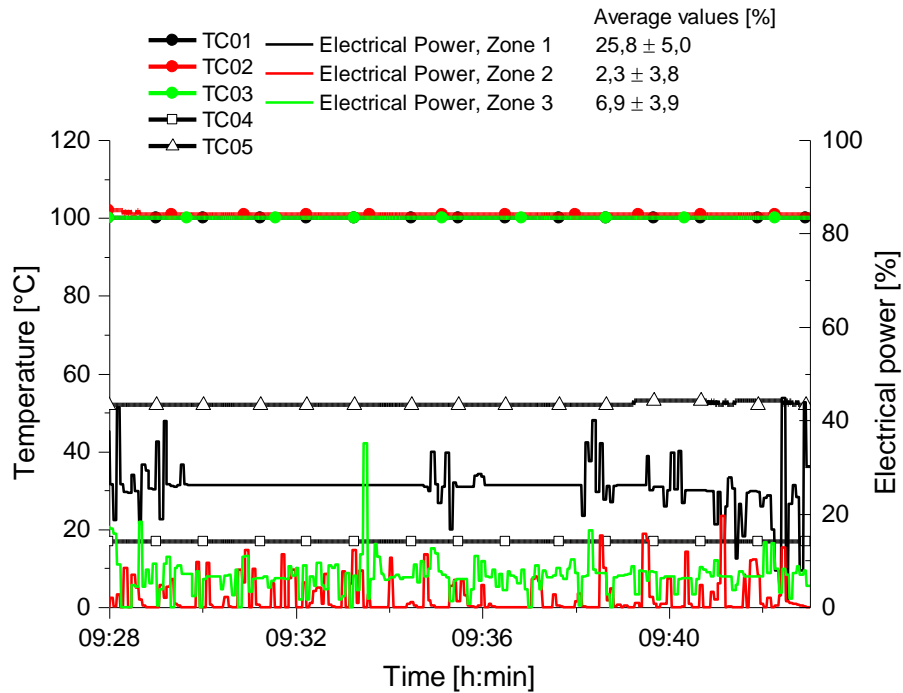


Figure 6.8: Thermocouple signals and power input to the electrical heaters over a 20 min time span during trial configuration 8

Figure 6.9 shows the plots of pulling force, pulling speed and liquid resin pressures for the trial configuration 8. Some fundamental differences in the processing can also be seen by comparing the signals with the analogous signals measured for the conical die assembly (Figure 6.5). The pulling force level is considerably lower, despite the larger cross section. The pressure needed to pump the resin into the die is apparently higher than the pressure measured by the pressure transducer mounted near the injection nozzles. However, since the signal progression is the same for both plots, they may be regarded as equal. The difference can thus be considered as the head loss needed to pump the resin through metering system, mixing head and discharge tubes.

The pressure level at the tapered-straight transition region was lower than obtained in the trials with the conical die assembly. This might be due to the design geometry itself, but possibly also to a larger impact of deformation of the die inner cavity. The pulling force signal progression did not correlate directly with the pressure signal (in comparison to Figure 6.5), indicating a lesser contribution of the liquid resin pressure to the pulling resistance in this trial assembly.

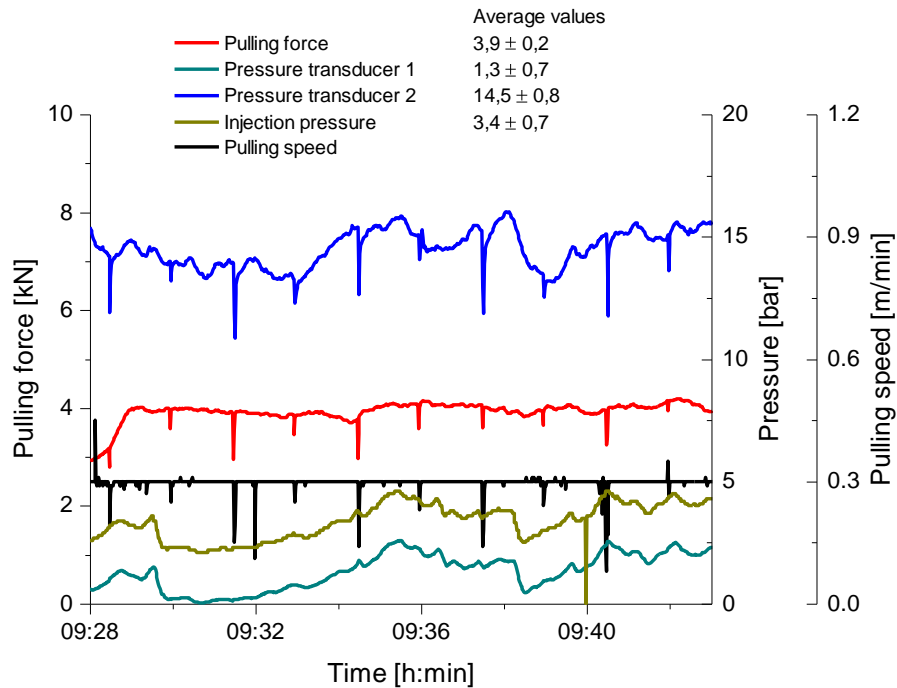


Figure 6.9: Plots of measured pulling force, pulling speed and liquid resin pressures over a 15 min time span during trial configuration 8

6.2.3 Distribution of fibers within the tear drop injection chamber

In contrast to the conical die, the distribution of the reinforcement fibers in the injection and impregnation chamber of the tear drop die could not be geometrically determined or approximated by the die assembly design. After passing through the inlet region, the fibers are stretched while in a region with much larger volume filled with resin. The stretching is a result of the pulling action exerted by the machine and the resistance produced by friction when passing through the guiding plates and die inlet. The actual thickness (distribution) of the fiber stack in the injection chamber is unknown. This is an important input parameter for simulation purposes, as the thickness defines the porosity and thus the local permeability within the stack.

To evaluate the fiber distribution within the injection region, samples of the whole region were obtained by purposely shutting down the process. The pulling process and the injection were stopped at the same time, and heating plates were fastened over the chamber to induce curing of the resin. The result was a block of cured resin with a similar form of the tear drop chamber, with the embedded fiber stack. Samples were obtained with glass and carbon fiber stacks, both with a nominal fiber volume content of 64 %. Pictures of the samples are shown in Figure 6.10.

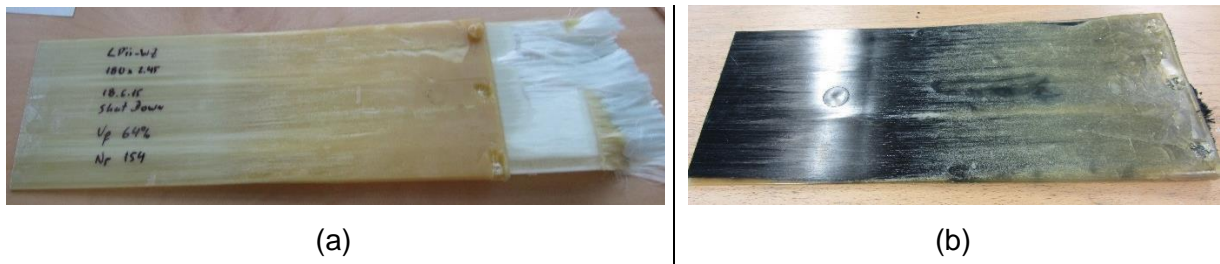


Figure 6.10: Samples obtained from a sudden process shut down of the tear drop die. (a) Glass fiber stack; (b) carbon fiber stack

The fiber distribution within the tear drop region was evaluated by means of optical microscopy. Samples were cut from the block to obtain visible areas parallel and normal to the pulling direction. The mapped regions are highlighted in Figure 6.11.

When cutting the samples, it could be observed that wetting out of glass fibers is good even in the region closed to the inlet nozzles. In contrast, the sample with embedded carbon fibers (Figure 6.10 (b)) was formed by a skin of matrix surrounding a predominantly dry fiber stack. Wetting out occur gradually, with fibers properly impregnated only near the end of the tapered region. For this reason, many of the cut samples with the embedded carbon fiber stack could not be analyzed.

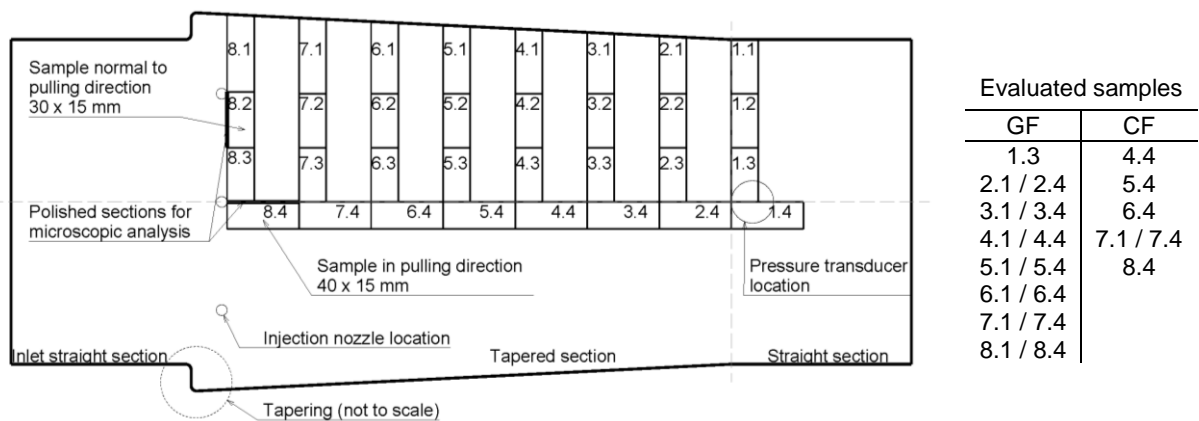


Figure 6.11: Top view sketch showing the mapping of sections for microscopic analysis from shut down samples. The right side table indicates which samples were actually evaluated

Figure 6.12 shows an example of a cross section sample with a glass fiber stack. For the dimensional analysis, the region delimited by the embedded stack was hand marked and the picture was superposed to a chart with scales adjusted to the picture. The red marking lines were then interpolated and the bottom line subtracted from the top line to find a thickness curve along the width. Finally, the mean value and standard deviation were calculated from

the thickness values. The analysis of the sample pictured in Figure 6.12 is shown as an example in Figure 6.13. Additionally, the area delimited by the fiber stack and the total area was measured. The ratio between these areas was found to correlate well with the average of the ratios between stack and total heights.

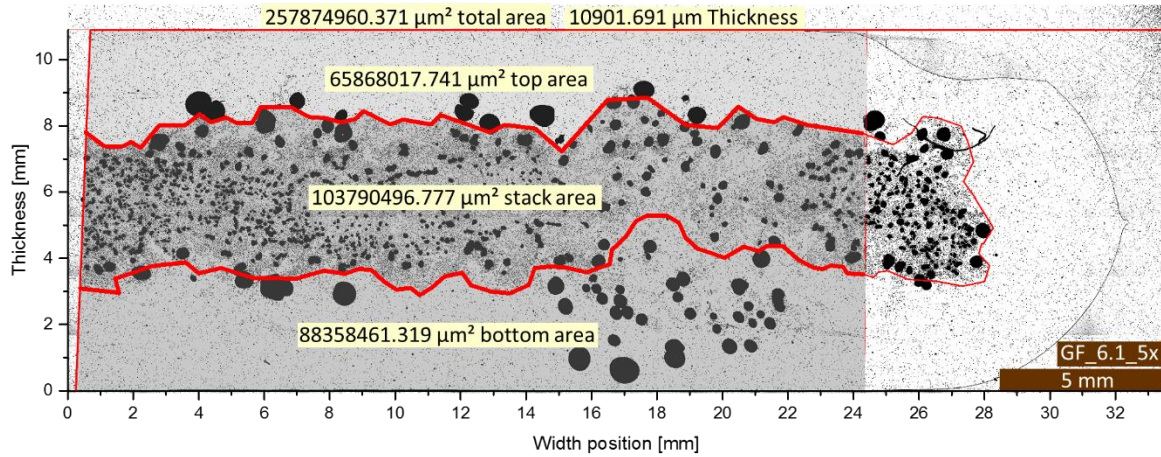


Figure 6.12: Example of a cross section sample of the injection and impregnation region embedded with a glass fiber stack

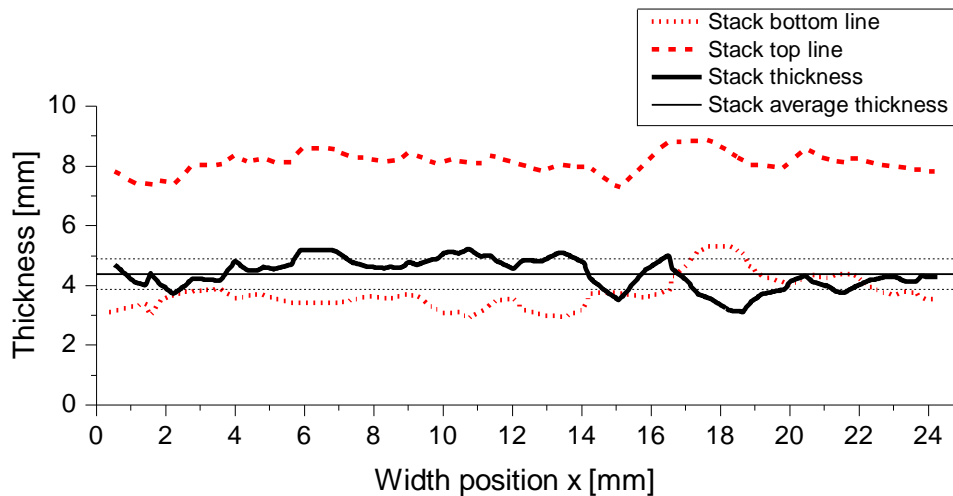


Figure 6.13: Analysis of thickness curves obtained from the cross section sample shown in Figure 6.12

Figure 6.14 shows an example of analysis undertaken on the longitudinal samples. The tapering angle was measured from the sample contour. Measurements of stack and fiber-free regions were made in different positions. In contrast to the cross-section samples, no average is taken in this case, since each position corresponds to a different cross section.

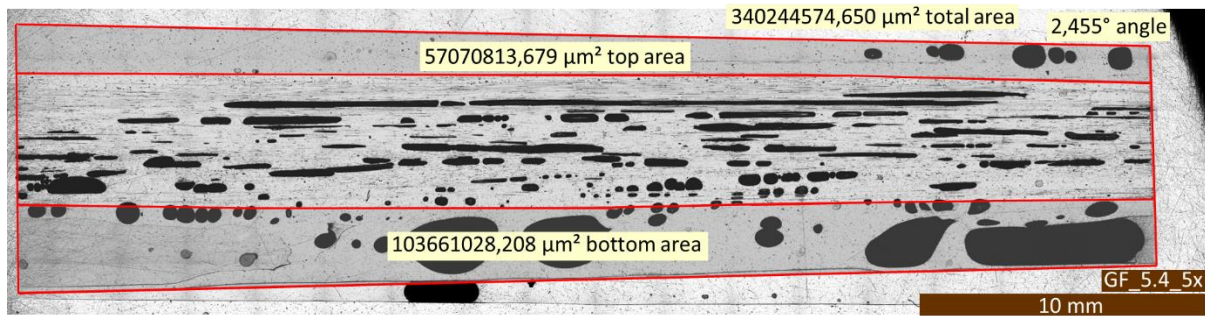


Figure 6.14: Example of a longitudinal sample of the injection and impregnation region embedded with a glass fiber stack

The results for the microscopic analysis of the samples embedded with glass and carbon fiber stacks are summarized in Figure 6.15. From observation of the different samples, it can be stated that the fiber stack lies stretched with a nearly constant thickness over the free volume region of the injection chamber. This was observed by the average values of cross section samples embedded with the glass fiber stack, represented by the blue points, and by most of the values taken from longitudinal samples (red points). The constant thickness prevails up to the x-position where the die tapering has the same thickness as the fiber stack. From this point on, the fiber stack was compressed along the tapered cavity similarly to the conical die.

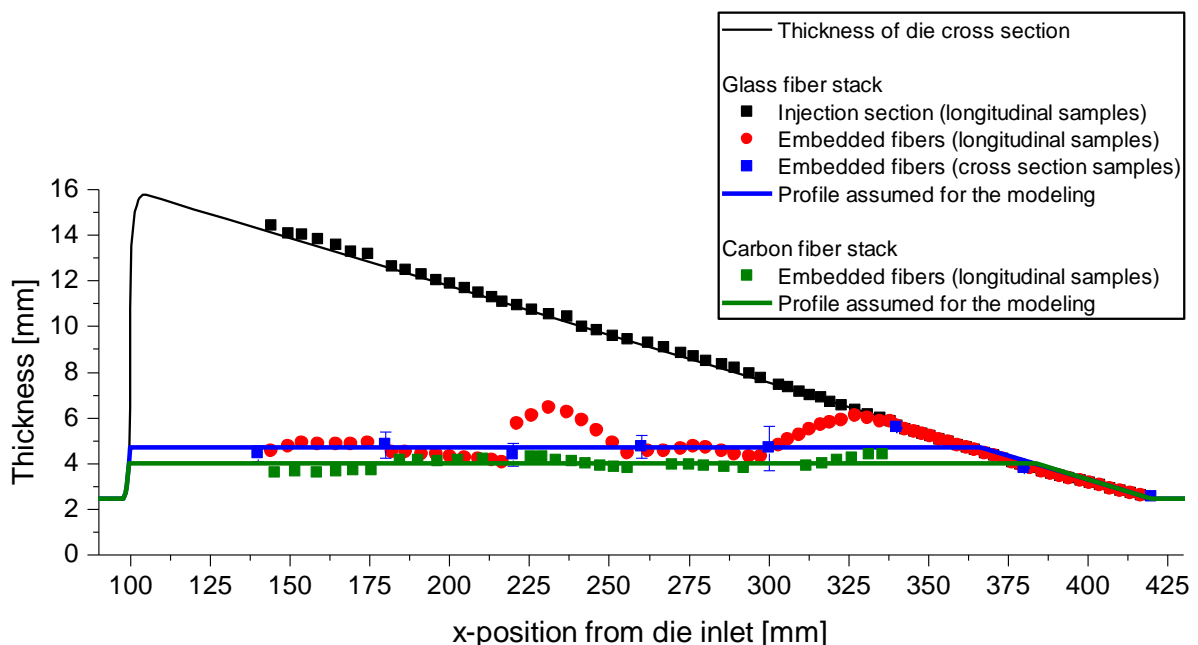


Figure 6.15: Results from microscopic dimensional analysis on longitudinal and cross section samples embedded with a glass fiber stack

The thicknesses measured for the injection region with the embedded glass fiber stack (black points) agreed well with the nominal values according to the die design (black line), indicating that no significant shape distortion occurred during the curing and/or sample preparation process. On the other hand, samples with carbon fiber stacks showed very different thicknesses because of the largely dry fiber stack surrounded by the cured matrix. For these samples, a correction for the measured thickness of the fiber stack region was done, so that the sum of thicknesses is equal to the nominal die thickness. The green points shown in Figure 6.15 represent the corrected values of the embedded stack.

For modelling purposes, a constant thickness in the free volume injection region was assumed. The thickness was calculated from all values obtained from cross section samples (blue points) as (4.7 ± 0.8) mm. Although gradients in the fiber agglomeration within the stack can be seen in the micrographs, for simplification the thickness was assumed as having a constant fiber volume content of 34.1 %. For the carbon fiber stack, an average thickness of (4.0 ± 0.2) mm was calculated, corresponding to a fiber volume content of 39.5 %. The blue and green lines in Figure 6.15 represent the thickness profile assumed in the model development (see Section 7.1.3.2).

7 Modelling and simulation of the closed injection pultrusion

The development of simulation models useful for the analysis of processing phenomena within closed injection pultrusion dies is described in Section 7.1. Aspects of the geometric design, meshing of the simulation domain and implementation in the preprocessor environment are discussed. The material models developed in Sections 4 and 5 are also fed to the simulation model as input parameters. The development of a simulation code used to predict pressure variations in the straight die section due to thermal expansion and curing effects is described, as well as the strategy for coupling the two different simulation models. In section 7.2, results of several simulation runs used to predict different physical phenomena are presented and discussed.

7.1 Modelling of the closed injection pultrusion

Based on the dies presented in Section 6, two models are developed in this section and applied in the simulation studies (Section 7.2). The models include the geometrical design of each die, which is spatially discretized into a mesh, its boundary conditions and other constraints. A 2D geometry simplification was chosen for the conical die and a 3D model was developed for the tear drop die.

The commercial software package used in the simulation studies, Ansys CFX 14.0, is built upon a finite volume discretization method. In contrast to the finite element method, the domain discretization in plane (2D) elements is not possible, i.e. the mesh elements and domains are always volumetric. To overcome this limitation, one can build a quasi 2D model as a very thin layer and set the side boundaries as a symmetry condition.

After designing the geometric model, the quasi 2D or 3D volume is spatially discretized by dividing it into volume elements. The mesh in a quasi 2D model is set to have one element thickness. Mesh resolution is a very important aspect in the spatial discretization process, in which a balance must be found between obtaining fast enough simulations with the available computational resources and realistic simulation results. This is typically done by comparing simulation results obtained from meshes with different element sizes.

Another important aspect of the discretization process is mesh quality. In the Ansys CFX best practice guidelines, some recommendations are given for grid generation. Whenever feasible, a so-called structured mesh, i.e. a regular grid with ordered elements, e.g. hexahedrons, should be implemented. Sharp angles in tetrahedral and pyramid elements

should be avoided. Highly skewed faces and elements are unacceptable because the equations being solved assume that the cells are relatively equilateral/equiangular. The meshing application included in the Ansys Workbench was used to generate all meshes in this study. It provides several indexes of meshing quality. In this work, the skewness was monitored to assess mesh quality. The skewness value determines how close to ideal, i.e. equilateral or equiangular, a face or element is. It is therefore also correlated to the orthogonal quality. Table 7.1 lists the values of skewness and the corresponding element quality. Quality grids have an average skewness value of approximately 0.1 for 2D and 0.4 for 3D. In 3D grids of complex geometry, a small percentage will generally be in the fair range and even a few poor cells may be accepted [81].

Table 7.1: Classification of element quality according to the skewness values

Value of Skewness	0	0 – 0.25	0.25 – 0.5	0.5 – 0.75	0.75 – 0.9	0.9 - 1	1
Element quality	Equilateral	Excellent	Good	Fair	Poor	Bad	Collapsed

The geometric design is subdivided into different volumetric regions, which are then assigned to different domains. In the simulations conducted in these studies, three types of domains are applied:

- Solid domains, in which only the energy equations are solved, and may be typically discretized to coarser meshes
- Liquid domains, where flow of liquid resin is calculated, together with the energy balance
- Porous domains, where the flow of resin through a porous medium (the fiber stack) is solved

There are two alternatives for calculating flow in porous media in CFX [81]. The first one is to apply a fluid domain together with a model for momentum loss, which accounts for the effects of porosity. This is named the superficial velocity formulation in CFX. The second option is a full porous model, in which all governing equations are changed, and thus the solid material properties and interactions between liquid and solid parts of the domain, e.g. heat transfer, are calculated. The latter model was applied throughout this work.

Besides the assignment of domains, the model definition in the preprocessor includes the setting of boundary conditions and material parameters. The boundary conditions are specific for each die design and are discussed in Section 7.1.3. The material parameters obtained from the models developed in Sections 4 and 5 are applied in the model definition.

The porous model supports the definition of two permeability parameters: one in the streamwise and one in the transverse direction. The streamwise direction can be defined by any vector direction in the Cartesian space. In this work, the streamwise direction, i.e. the main direction of flow is defined as coincident with the x-axis. This is also the pulling direction. Consequently, the permeability along the x-axis is set as K_1 and along the y- and z-axis are equal to K_2 (see Section 5.3.2).

The curing reaction is implemented by means of an additional variable (the degree of cure α) in Ansys CFX. It is treated by the solver as a non-reacting scalar component that is transported through the fluid [81]. Two source terms in the liquid part of the porous domain are associated with this additional variable: the source of α itself, described by Equations 4.5 through 4.8, and an energy source given by Equation 4.9.

With the calculated local degree of cure, the local resin viscosity can be obtained from Equation 3.16 and the parameters listed in Table 4.5. However, the software becomes unstable when a high viscosity value is set, since its solving algorithm was developed for the computation of turbulent flow of low viscosity liquids and gases. To overcome instability issues during the calculations, the viscosity is defined as the minimum between the value calculated by Equation 3.16 and 10 Pa·s.

7.1.1 Geometric design

The existing pultrusion dies were designed in the Ansys Workbench CAD tool (DesignModeler) in a simplified form containing the geometric parameters relevant for the subsequent simulation studies. The advantage of using the integrated CAD tool is the possibility of easily defining design parameters which can be later parametrized and automatically updated during sequential simulation runs. Two different approaches were chosen for the different dies with the purpose of analyzing the reasonability of increased model complexity in contrast to the results obtained. The design simplification included the use of symmetry and the appropriate elimination of features such as small radii to reduce the overall size and complexity of the mesh.

7.1.1.1 Conical die

For the conical die, a thin layer model was designed with the same geometric parameters as the die used in the trials (see Section 6.1.1). The layer thickness was set to 0.3 mm. Only

half of the geometry was designed considering the die symmetry along the die centerline. A symmetry condition was therefore set to the bottom surface of the model. The geometric model is shown in Figure 7.1, in which the four existing domains are shown up to the beginning of the straight curing section. The metal die region was set as a solid domain. The injection nozzle was set as a fluid domain. The region through which the fibers are pulled was set as a porous domain.

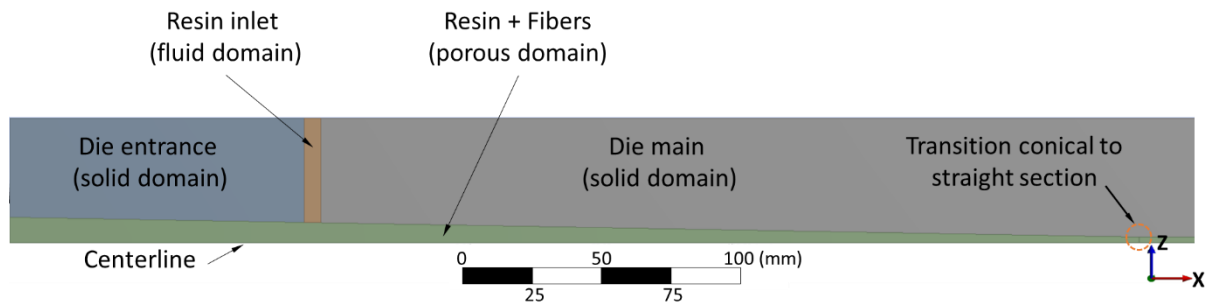


Figure 7.1: Geometric quasi 2D model of conical die (curing section not shown entirely)

The model was parametrized so that changes could be easily made in geometric design. To study increasingly complex material models, two geometric designs were set. The first one had a conical length L (see Figure 7.5) of 410 mm, i.e. the region upstream of the opening to the atmosphere (see Figure 6.1) was excluded from the domain. The second one reproduced the whole actual length of the inlet chamber. The set geometric parameters for the second model of the complete die described above are listed in Table 7.2.

Table 7.2: Geometric parameters set in the conical die design

Geometric parameter	Default value
Composite thickness [mm]	2,0
Length of the conical section [mm]	500
Angle of conical section [°]	1
Nozzle diameter [mm]	6
Inlet nozzle x-position [mm]	200

The surfaces at the top of the die where the cooling plate and electrical heaters were located were also defined during the design phase. Values of heat fluxes were set to these surfaces during the model setup (see Section 7.1.3).

7.1.1.2 Tear drop die

A 3D geometric model was developed for the tear drop die. From observations made during the trials, the short resin pot life associated with the specific chamber design led to stagnation regions of relatively long residence time, where resin locally gels (see Section 6.2.2). As processing time progressed, the chamber became gradually filled with gelled matrix. A fluid flow simulation within a 3D volumetric field is expected to deliver a better representation of such stagnation regions, in comparison to a quasi 2D model like the one developed for the conical die.

A 3D model representing $\frac{1}{4}$ of the die was designed as shown in Figure 7.2, according to die symmetry. All main dimensions were designed as the actual die (see Section 6.1.2). The only simplification made was the exclusion of edge radii existent at the entrance section, i.e. at the die inlet and at the transition from the entrance to the tapered section, and at the outlet. Similarly to the procedure adopted when designing the conical die, the cooling and heating zones were assigned to surfaces delimited by the top surface of the solid domain.

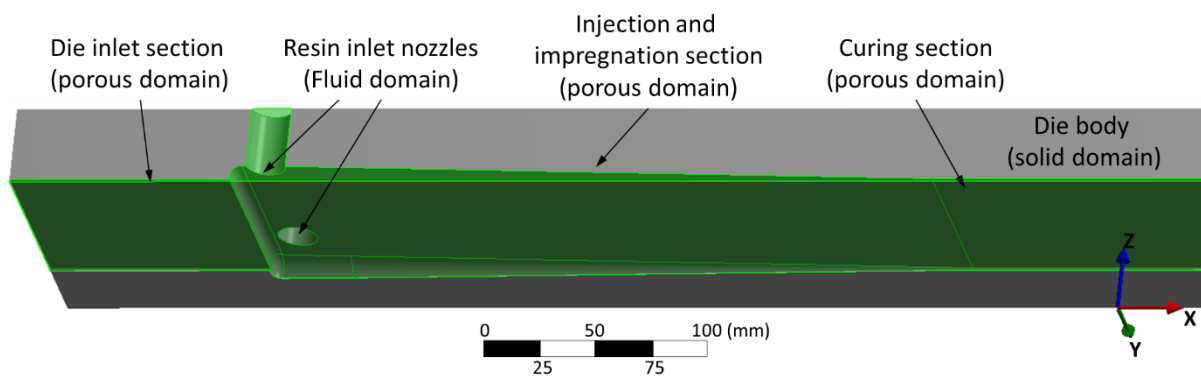


Figure 7.2: 3D geometric model of tear drop die (curing section not shown entirely)

The geometric details of the die are also parametrized, as done in the conical die design. This allows modifications of the geometry in order to perform parametric studies (see Section 7.2.3). Table 7.3 lists the set geometric parameters for the tear drop die described above.

In order to evaluate only curing aspects in steady state, another geometrical design was set with a constant cross section over the whole die length, i.e. excluding the injection and impregnation region. This is needed because the relatively large impregnation region volume leads to ever growing reaction conversion at low local velocity spots. The steady state computation is thus unstable in this configuration.

Table 7.3: Geometric parameters set in the tear drop die design

Geometric parameter	Default value
Composite thickness [mm]	1,22
Length of die inlet section [mm]	100
Inlet nozzles x-position [mm]	116
Nozzle diameter [mm]	18
Spacing between nozzles [mm]	71
Angle of tapered section [°]	1.2
Length of tapered section [mm]	320

7.1.2 Meshing strategy

The next step in building the simulation model is the meshing of the volume domain, which is also executed within the Ansys Workbench Meshing application. The program is capable of automatically discretizing a volume domain, but also provides a number of user options for global and/or local mesh control, e.g. definition of element types and local refinement. In accordance to the geometric designs previously described, the meshing process for the 3D tear drop model is also more complex than the 2D conical die model.

7.1.2.1 Conical die

The simplified layer model shown in Figure 7.1 can be easily discretized in a structured mesh of hexahedral elements. This is done by setting the same number of elements in the thickness direction both in the straight section and in the chamber inlet. An example is shown in Figure 7.3 (a), in which the porous region is set to have 5 elements in the thickness direction throughout the whole length. Note that the element length is increased in the straight section, in order to reduce the total number of elements.

In order to evaluate the effect of mesh resolution in the interface between fluid and solid domains, a comparison was made between a coarse grid in the porous domain, as depicted in Figure 7.3 (a), and a finer mesh with high resolution at the boundary layer in Figure 7.3 (b). In this mesh, 15 elements were set in the thickness, with a bias factor to increase the resolution near the interface. This is recommended for liquid domains to account for the boundary layer formed near the walls. The necessity of this finer resolution in the case of the porous domain was examined in this study.

The generation of a high resolution mesh according to this strategy leads to very thin elements, i.e. with a large length to thickness ratio, especially at the straight section near the outlet of the porous region. This was however preferred over the generation of an unstructured mesh with poor levels of orthogonality.

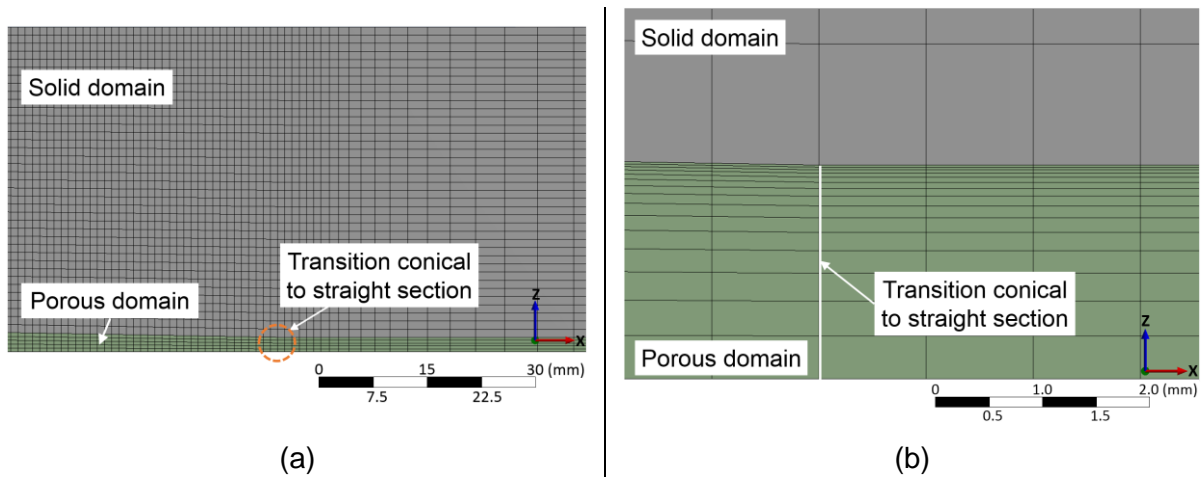


Figure 7.3: (a) Example of local mesh for the conical die quasi 2D model; (b) zoomed view of the mesh with high resolution at the solid-porous interface, in the transition region conical-straight in the conical die model

7.1.2.2 Tear drop die

Due to the increased geometric complexity, finding a suitable and reliable meshing strategy for the tear drop design is more challenging than in the case of the conical die. On the other hand, further simplification of the design geometry is not desirable, as the primary interest is to calculate the flow field within the more complex tapered section. Defining a reliable meshing strategy is even more important when considering parametric studies, as the geometry and subsequently the meshing process are ideally updated automatically, i.e. without further manipulating the meshing setup configuration.

The most consistent meshing method found requires further subdivision of the whole porous domain (green body in Figure 7.2) into several separate bodies in the design application: the die inlet and the curing sections, which can be meshed to a similar structured grid composed of hexahedral elements, and the injection and impregnation section (including the injection nozzles), which is further subdivided into four sections. Figure 7.4 shows a top view of the porous domain subdivided into meshing sections. The meshing process is conducted sequentially for the six defined bodies in the shown order sequence. The section denoted as 1 is the die inlet section denoted in Figure 7.2, and section 2 is the beginning of the curing region. The die body is meshed in a last step (denominated as 7). By the sequential meshing

procedure, the algorithm takes into account neighboring section(s) previously meshed in respect of their contact surface mesh. This allows for the generation of structured grids similar to the quasi 2D model (see Figure 7.3), i.e. composed of hexahedral elements only, in the sections 1 through 4. Sections 5 through 7 are then meshed with tetrahedral elements.

In the sections 1 and 3 through 6, one is interested in the flow field, and therefore a better grid resolution is needed. An element size of 1 mm was set in these sections. In section 2, the element length is set as starting with 1 mm and then increasing towards the downstream direction of the die up to a length of 6 mm, similarly to the grid shown in Figure 7.3. The sections 1 through 4 are set to have 5 elements in the thickness direction.

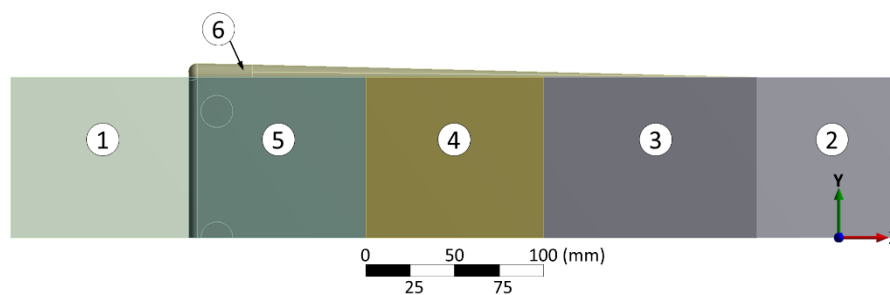


Figure 7.4: Top view of the tear drop die geometry model (the die body is hidden), showing the sequence used for meshing the different regions

Despite the relatively large element size set to the die body, the final mesh is formed by a relatively large number of volume elements. Quality parameters obtained for the created mesh are given in Appendix B. The overall mesh quality is good, with some isolated poor elements in regions 5 and 6 of the resin flow domain, and in the die body, which is considered uncritical, since only the energy balance is solved in the latter region.

7.1.3 Model parameters

In complementation to the general modelling aspects presented in Section 7.1, the input parameters specific to each of the modelled dies are discussed in the following Subsections. The general material parameter settings, domain configurations, and boundary conditions are described. Of major importance is the definition of the permeability within the porous domain, which is specific to the die geometry.

7.1.3.1 Conical die

In the straight section of the conical die, the fiber volume content is constant. In the tapered section, the porosity and consequently the permeabilities vary according to the position along the x-axis. Two models of increasing complexity are proposed and applied in this study. The first simplified model assumes that the fibers are distributed uniformly across the thickness direction within the tapered region. For a unidirectional roving stack, the porosity is calculated from Equation 7.1 and the corresponding geometric parameters shown in Figure 7.5. The fiber volume fraction along the conical section, V_{fx} , is given by Equation 7.2 as a function of the geometric parameters and the final volume fraction V_f in the straight section.

$$\phi_x = 1 - \frac{h_c(1 - \phi_c)}{h_c + (L - x) \tan \theta} \quad \text{Equation 7.1}$$

$$V_{fx} = 1 - \phi_x = \frac{h_c \cdot V_f}{h_c + (L - x) \tan \theta} \quad \text{Equation 7.2}$$

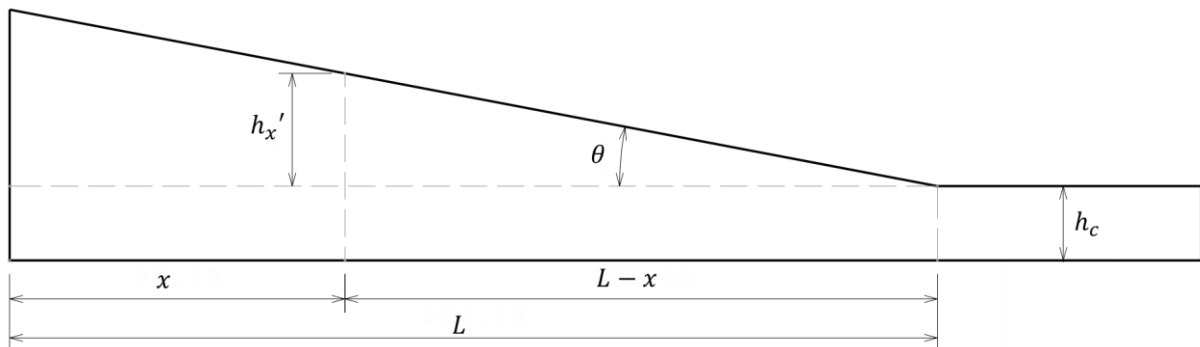


Figure 7.5: Geometric parameters of the tapered inlet used for calculating the local porosity of the fiber stack as a function of the x position

The second model proposed considers the inhomogeneous distribution of fiber bundles within the tapered region. In the conical die assembly, the fiber bundles are threaded through a guiding plate with a specific hole pattern. These bundles are therefore actually separated from each other during the pulling process until they reach a point in the tapered region where the stack is compacted. Figure 7.6 schematically depicts the fiber bundle distribution within the tapered region and how it is converted to a simplified porosity distribution in the simulation model.

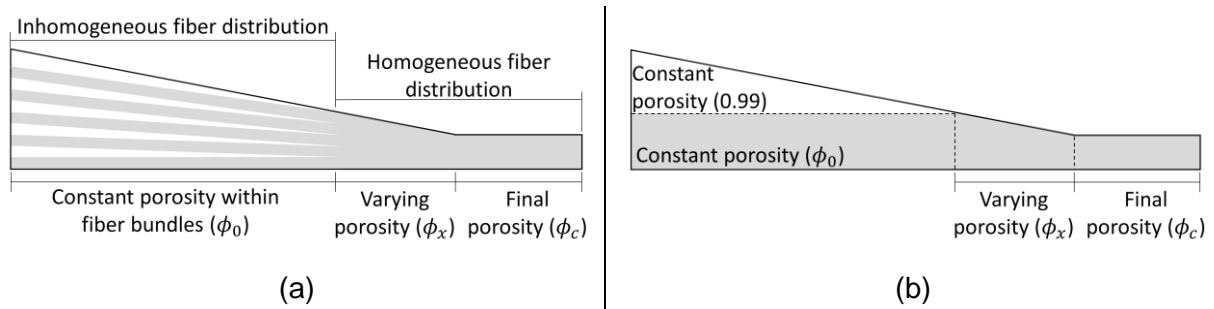


Figure 7.6: (a) Schematic representation of fiber bundle distribution within the tapered region, according to experimental assembly; (b) Porosity distribution applied to porous domain in the simulation model

Within the inhomogeneous region, the fiber bundles have a constant porosity $\phi_0 = 0.65$, which is the value of porosity at zero compaction pressure found in compressibility measurements (see Table 5.4). For simplification purposes, the respective regions of fiber bundles and neat resin are assembled together and assigned to the regions depicted in Figure 7.6 (b). A very large porosity of 0.99 is assigned to the neat resin region. The function ϕ_x is calculated according to Equation 7.1.

Figure 7.7 shows the values of porosity and the permeability values K_1 and K_2 for a fiber volume fraction of 64 % in the straight section of the die. The permeabilities are calculated according to the Gebart functions (Equation 3.19 and Equation 3.20) and the equivalent fiber diameters obtained from the fitting procedure discussed in Section 5.3.2. For the second model, the position along the tapered section from which the fiber stack is compacted is found as $x = 405$ mm, where the porosity is equal to 0.65.

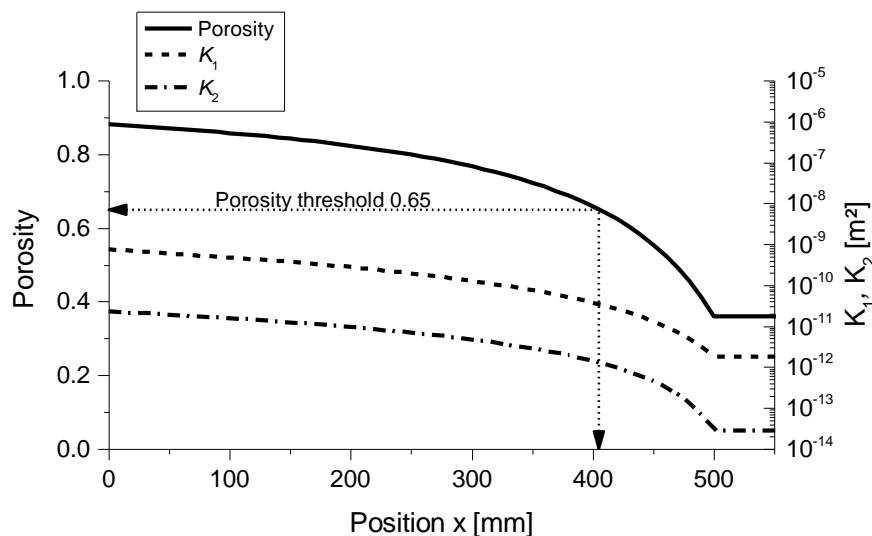


Figure 7.7: Porosity and permeability coefficients of a roving stack as a function of the x position in the tapered section of the conical die.

The permeability function of a CFM / roving / CFM reinforcement stack along the tapered section cannot be directly calculated as the above unidirectional case. The individual thicknesses of each layer as function of mechanical pressure must be taken into account. The following procedure is used to calculate the permeabilities:

1. Define a compaction pressure for the stack in the final profile cross section (90 x 2 mm²). The pressure was set to 2.1 bar in this study
2. Calculate the thickness of the roving layer by subtracting the thickness of CFM layer (0.49 mm in this study) for the given compaction pressure
3. Calculate the number of rovings needed to fill the remaining 90 x 1.51 mm² cross section (83 rovings in this study)
4. Obtain curves of thickness vs compaction pressure in the range 0 – 2.1 bar. The maximum thickness (zero compaction pressure) found for the stack is 3.61 mm. The CFM layer thickness (1.14 mm) is considered constant and only the roving layer fills the tapered region where the cavity height ($h_c + h_x'$) is larger than 7.23 mm
5. Calculate the porosity and permeability distributions along the x-axis for each layer

Figure 7.8 shows the values of porosity and the longitudinal permeability K_1 calculated according to the procedure described above. The roving layer permeability is calculated according to the Gebart function and the CFM permeability according to the Kozeny-Carman model with the adjusted longitudinal constant shown in Figure 5.13. The implementation of individual layers in the CFX preprocessor considers the conventional stacking sequence of pultruded laminates with the CFM as an outer layer. In the model, this results in a region with constant thickness running parallel to the tapered wall up to approximately 400 mm from the die inlet. From this point on, it is compressed together with the roving layer until the end thickness is reached. Due to the increased complexity of this multilayered case, the inhomogeneity in the roving layer is not implemented in this model, as previously done for the unidirectional case.

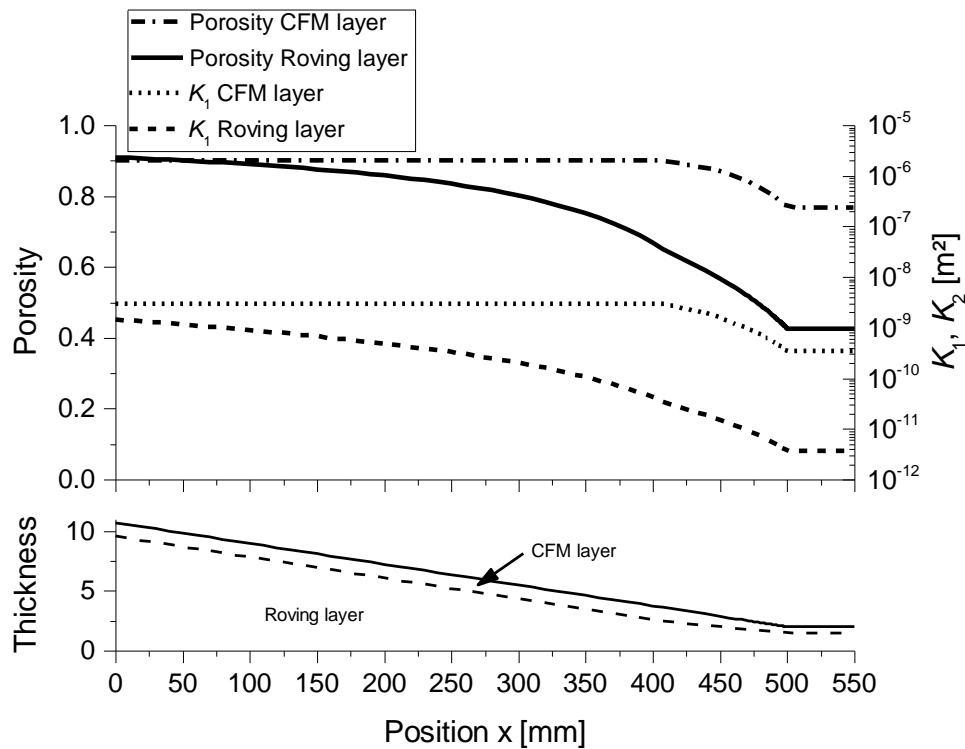


Figure 7.8: Porosity and permeability coefficients of a CFM / roving stack as a function of the x position in the tapered section of the conical die

Two geometric models were defined for the conical die. A first one has a shorter length of the conical chamber, starting from the opening to the atmosphere. A single-phase material model was applied to this design, i.e. the only fluid occupying the liquid domain, as well as the liquid part of the porous domain is the resin.

A multiphase material model was set to the second design. This was set as a homogeneous mixture of resin and air. The homogeneous model is a limiting case of multiphase flow with very large interphase transfer rates. This results in both fluids sharing a common flow field, and thus allows the two phases to easily separate and build a well-defined free surface [81].

The goal of applying two different models is to obtain easy convergence of the simulation depending on the focus of the study. If one is for example primarily concerned with the evolution of the curing reaction in the straight section of the die, the single-phase model delivers easier and faster convergence. On the other hand, the multiphase model is more suitable for analyzing the flow and pressure fields in the conical section, since it can determine the fluid flow front in the tapered region.

There are two inlet boundaries in the model: the resin inlet is set at a constant pressure, and the fibers inlet is set as an entrainment, i.e. an opening in which flow inwards and/or outwards is allowed. The outlet is set at a normal speed condition equal to the pulling speed.

Heat transfer between the solid domain and the environment is done by different surfaces assigned as one of the following options with corresponding boundary conditions:

- Wall: heat transfer coefficient (HTC): $10 \text{ W}/(\text{m}^2 \text{ K})$
- Ambient temperature $25 \text{ }^\circ\text{C}$, or actual temperature during the corresponding experimental trial
- Cooling zone: defined heat flux out of the domain
- Heating zone: heat flux in or out of the domain, depending on the location

The heat transfer between porous and solid domains is determined by a thermal contact resistance coefficient (TCR). According to Baran et al. [108], adjusting of this parameter is necessary for pultrusion process simulations including the heat transfer between the composite material and the solid die. An optimization procedure is presented in this study in which local TCR values are found that lead to good fitting of simulation results to experimental data. The reasoning for this is explained in the context of different material states along the die.

7.1.3.2 Tear drop die

A single-phase material model was considered for the tear drop 3D design, since the flow front is irrelevant in terms of process control, in contrast to the conical die. The cavity is always full of resin at all times, and this condition is monitored by adjusting the flow rate such that a small excess of resin flows out of the die inlet. The boundary conditions are defined similarly to the conical die specifications described in the previous section.

The porosity and permeability distribution in the inlet region of the tear drop die is set according to the analysis presented in Section 6.2.3. In the large volume inlet region, the fiber stack is assumed to have a constant thickness. Furthermore, the fiber distribution within this thickness is assumed to be uniform, and therefore constant porosity and permeability parameters are attributed to the stack. Towards the end of the tapered section, the stack is then constrained by the decreasing cross section area; the porosity and permeabilities assume in this region a profile like the calculated for the conical die (see Figure 7.7). Figure 7.9 shows the curves implemented in the model, as a function of the position along the x-axis from the die inlet.

The subdivision of the inlet region into different bodies is also advantageous for assigning the different values of porosity and permeability to the porous domain. In the regions where pure liquid resin flows, a very large porosity (0,99) and large values of permeability are set. A comparison was made between a flow simulation using these values and another one setting the same domain as a fluid, and the results obtained were identical. Table 7.4 lists the parameters assigned to each of the volume regions represented in Figure 7.4 for the base case of 64% final fiber volume fraction.

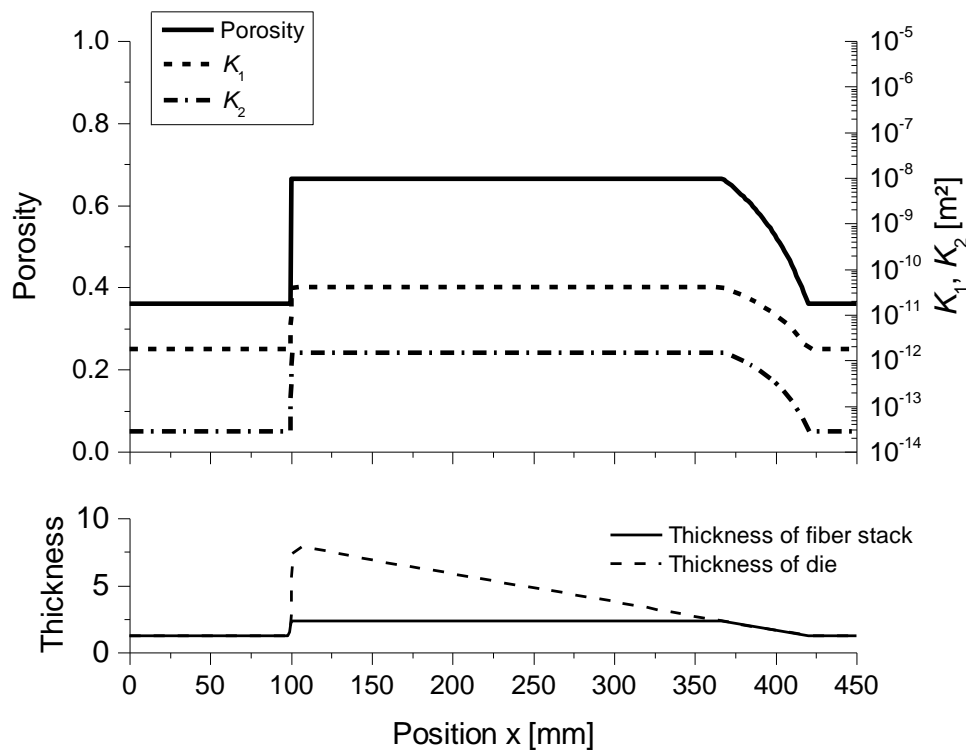


Figure 7.9: Porosity and permeability coefficients as a function of the x position in the inlet region section of the tear drop die

Table 7.4: Functions of porosity and permeability assigned for the different regions depicted in Figure 7.4

Region	Porosity	K_1 [m^2]	K_2 [m^2]
1, 2	0.36	1.8×10^{-12}	2.8×10^{-14}
3	Equation 7.1	Equation 3.19	Equation 3.20
4, 5	$z \leq 2,35$ mm	0.664	4.0×10^{-11}
	$z > 2,35$ mm	0.99	1×10^{-5}
6	0.99	1×10^{-5}	1×10^{-5}

In the curing simulations using the tear drop model, an unsteady state prevails due to the large volume in the inlet region occupied by resin only. This leads to a continuously increasing local degree of cure and reaction heat development. To overcome this, another simplified model was implemented with the same die body outer dimensions but without the injection and impregnation chamber.

7.1.4 Stress-strain model

A simulation code was written in the Wolfram language (Mathematica 9) based on the finite difference (FD) iterative algorithm proposed by Bogetti and Gillespie [88] [89], and recently applied by Baran et al [87] in pultrusion related studies. In these studies, the goal was to obtain the development of internal stresses and distortions within the laminate as the matrix cures. In the present study, this additional numerical solver is used for two purposes: (1) to correct the temperature of the rheology measurements and obtain a more accurate prediction for the degree of cure (see Section 4.4) and (2) to obtain a more realistic pressure distribution within the straight curing section of the die. The pressure changes within the region are modelled as being caused by two concurrent effects: the thermal expansion due to temperature increase within the material and volume shrinkage of the matrix as curing progresses. These effects on the resulting pressure in the die cavity cannot be calculated by CFX, since the coefficient of thermal expansion (CTE) is only used there to account for buoyancy effects in gases.

7.1.4.1 Model development and validation

The code was implemented as an alternating difference explicit (ADE) discretization method over a 2D domain representing the die cavity cross section. For the conical model, the 2D model reduces to a quasi 1D model with a very thin width and the minimum of 3 nodes in the y-direction, to allow for solving of the discretization equations in the same way as in a full 2D model. The spatial discretization is shown in Figure 7.10. By the ADE method, two sweeps, forward and backward are done in each iteration. The calculation of the temperature at a node i, j is done by each sweep from the known values at four adjacent nodes. The temperature at node i, j for that iteration step is then taken as the average value from both sweep results. The model is a time marching procedure, i.e. each iteration step corresponds to a real increment in time by the time step Δt .

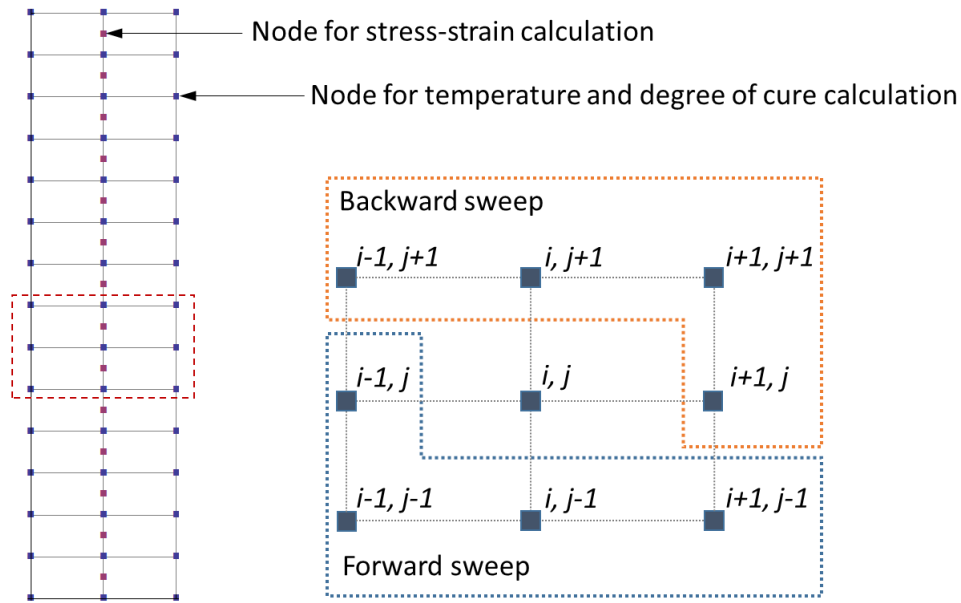


Figure 7.10: Grid definition showing nodes used to calculate the temperature and degree of cure fields and stress-strain relationships

The model was validated by running the same simulations for a plane stress assumption reported in [87] - [89]. The results obtained were similar to the literature reports. A comparison for some of the simulations is shown in Figure 7.11. For the pultrusion case, a plane strain assumption is applied for the profile cross section (see next section).

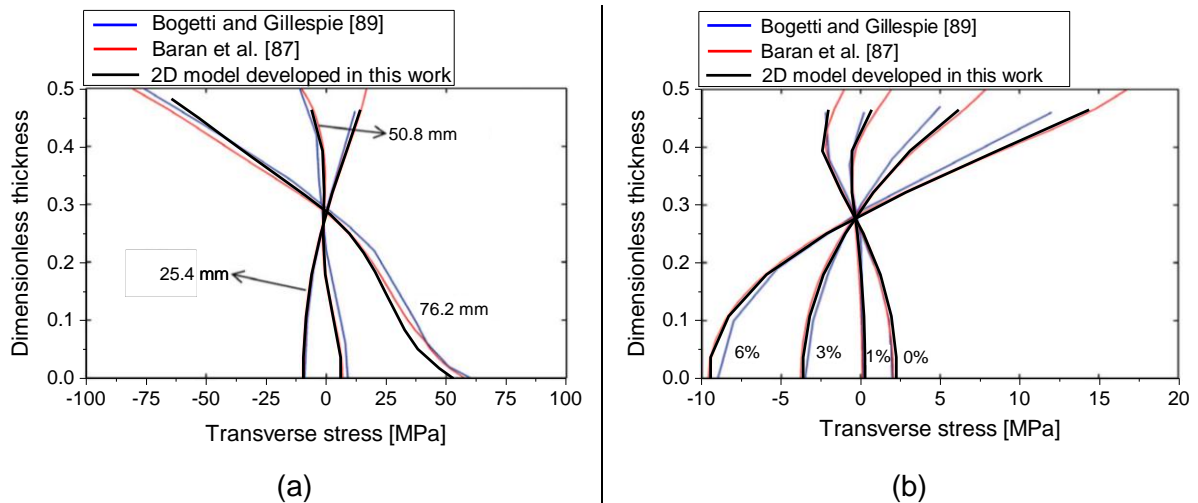


Figure 7.11: Comparison of results obtained from developed simulation code and results available in the literature [87] [89]. Predicted in-plane transverse stress for (a) different composite thicknesses and (b) different resin shrinkage factors

The kinetic model developed in Section 4.3 was applied to the implemented code for the calculation of degree of cure and temperature in a 2D field. The temperature function of time according to the heating rate was set as a prescribed value (Dirichlet condition). The curves

obtained by the NETZSCH Thermokinetics software and the implemented algorithm for the heating rates measured in DSC are compared in Figure 7.12.

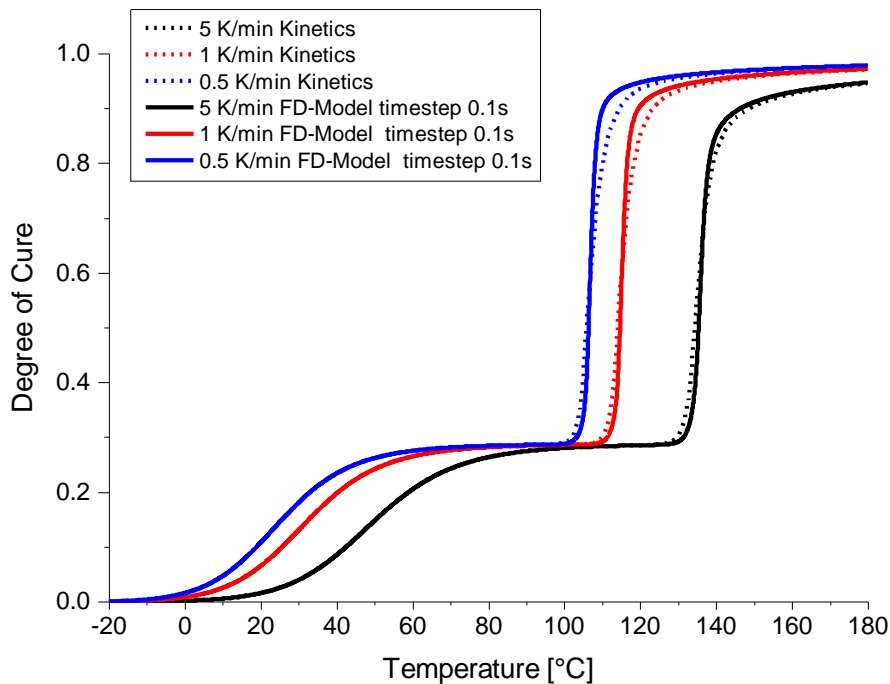


Figure 7.12: Degree of cure development as calculated by the Kinetics software and the Finite Difference (FD) model for different heating rates

Very similar plots are obtained by both calculations, thus giving confidence on the validity of the implemented algorithm. The use of this code has the advantage of taking into account the effects of heat conduction and of internal heat generation within the material on the temperature, and thus on acceleration of the reaction rate. An example of these effects is shown in Figure 7.13. The curves of degree of cure and temperature development for a heating rate of 5 K/min are plotted as calculated by the Kinetics software, as well as for 2D fields with $25 \times 1 \text{ mm}^2$ and $25 \times 2 \text{ mm}^2$ calculated by the implemented code. Plots are given for a point in the center of the 2D field, designated as bulk. It can be seen that the first reaction step evolves relatively smoothly, so that no significant temperature peak due to exothermic heat release is observed. The second reaction, on the other hand, evolves very fast, leading to a pronounced local temperature increase and faster curing in the bulk of the material. The extent of temperature increase and reaction acceleration is sensitive to the material thickness. A less pronounced temperature increase can also be detected at the margin of the 2D field, corresponding to the material surface (not shown in the plot).

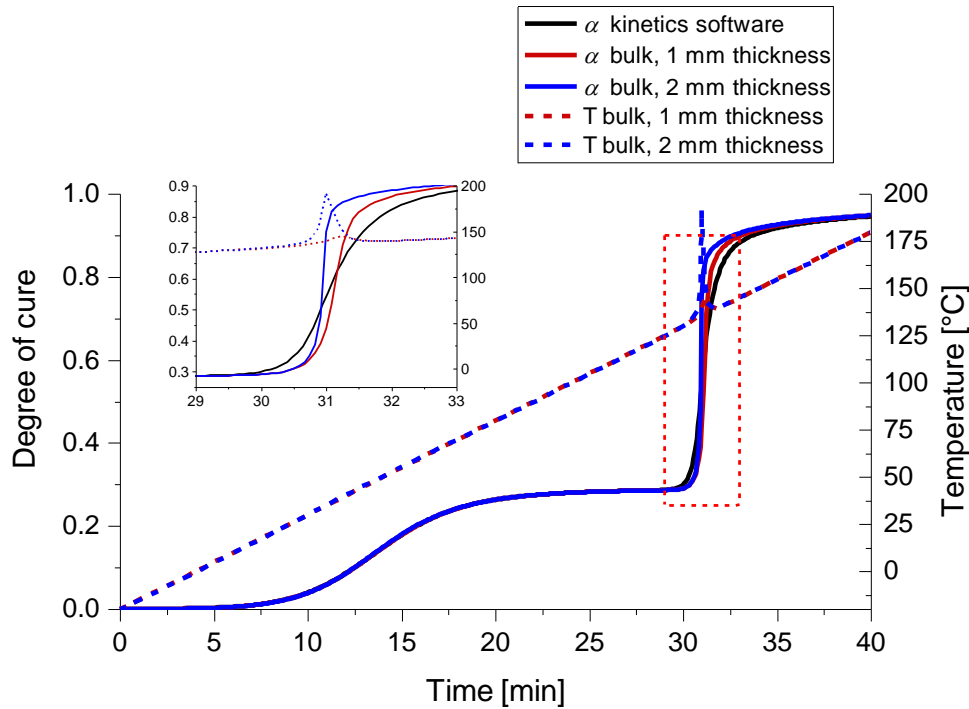


Figure 7.13: Degree of cure development and temperature for 2D fields of 1 and 2 mm thicknesses

7.1.4.2 Application in pultrusion process

Considering the coordinate system universally used in classical laminate theory, i.e. 1 being the main fiber orientation direction, 2 the cross direction and 3 the out-of-plane direction and setting these directions coincident with the global Cartesian coordinates xyz , a transfer of the model to the pultrusion process is depicted by Figure 7.14. As the material travels through the die, the temperature and degree of cure development is iteratively calculated, and from these values the stress-strain field is also obtained. In contrast to the results reported in [88] and [89], the material properties are the same for both directions in the 2D field considered in the pultrusion case. The time marching procedure translates to a Lagrangian framework in which each time step corresponds to a forward step in the x direction by $U \cdot \Delta t$.

The simulation run calculates the temperature and degree of cure distributions within the profile along the die, as well as the stress and strain in the cross section plane. A plane strain assumption is applied to the cross section plane. Normal stresses acting at the domain boundaries, i.e. at the material surface in contact to the die are calculated. These stresses are calculated considering the fictive unconstrained strain distribution within the material, i.e. as if the laminate was free to expand or shrink. However, the material is actually constrained by the die inner walls, which are here assumed as perfectly rigid; therefore a normal stress of the same magnitude but opposite direction is needed to “force” the material back to the

original cross section $b \cdot h$. The pressure exerted by the material over the die inner walls can thus be directly calculated from the load resultants. The cross sections considered in this study have relatively small thicknesses, so only the pressure exerted over the die top and bottom interfaces is considered.

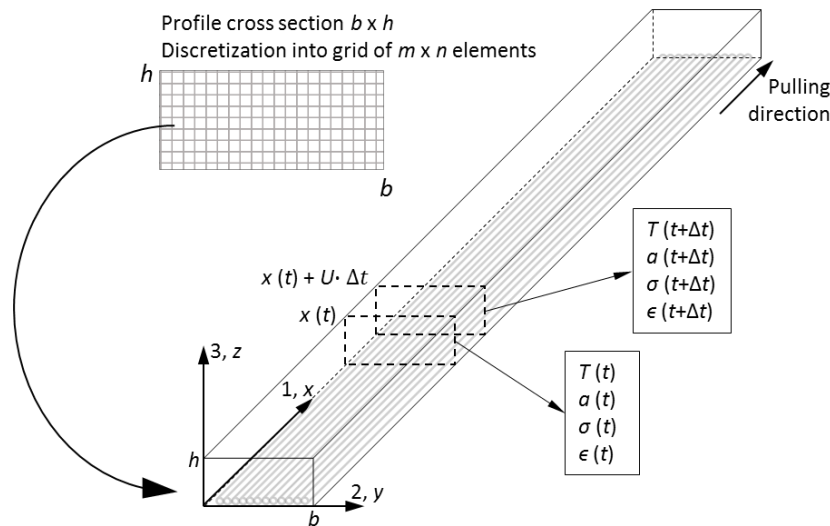


Figure 7.14: Schematic representation of pultrusion process in the context of the developed model for calculating the temperature, degree of cure, stress and strain fields

7.1.5 Simulation procedure

The procedure adopted for the simulation runs is represented by the flow diagram in Figure 7.15. After an initial simulation is run with a constant viscosity set in CFX, the development of temperature T and degree of cure α along the die is calculated. The temperature at the profile surface, i.e. directly in contact to the die interface is then transferred to the 2D stress-strain model and set as a prescribed function (Dirichlet condition). It should be noted that this model only reproduces the die straight curing section. The simulation calculates the contribution of thermal expansion and shrinkage to the pressure along this die section, which is implemented as a source term in the CFX environment.

A viscosity function of the x -position is also calculated as an average between the viscosity evolution curves along the material centerline and the material surface. The viscosity evolution is calculated by the Castro-Macosko model (Equation 3.16) with the parameters listed in Section 4.5. However, the solving process in CFX becomes unstable when a high viscosity value is set, because the solving algorithm is designed for turbulent flow regimes of low viscosity liquids and gases. In order to overcome instability issues during calculations,

viscosity is defined in CFX as the minimum between the value obtained from the viscosity function described above and 10 Pa·s.

A second simulation is then conducted with the viscosity and pressure source functions set in CFX to obtain the velocity and pressure distributions in the porous domain.

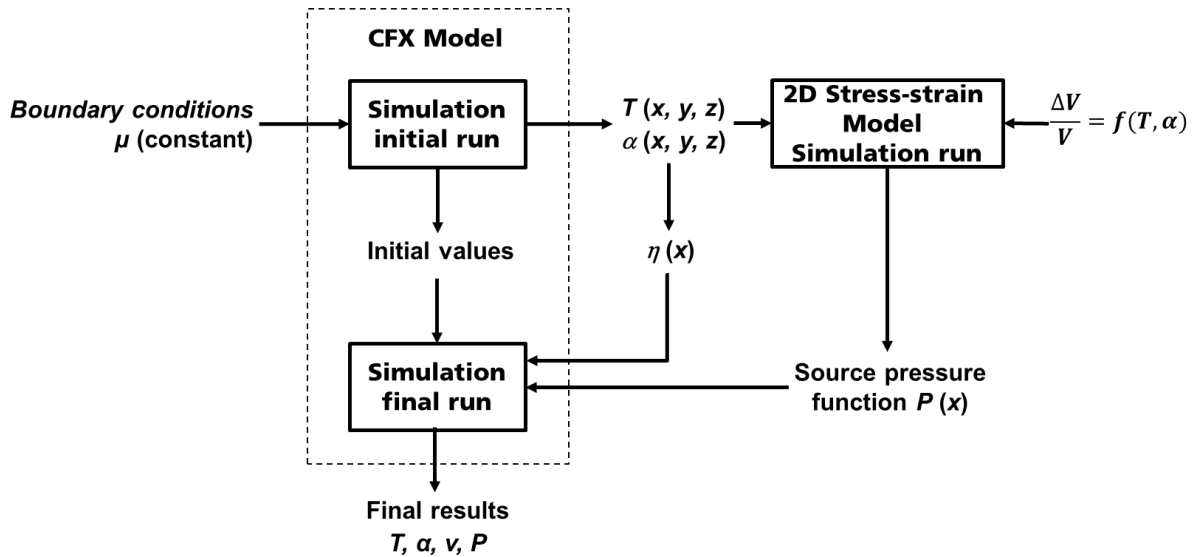


Figure 7.15: Flow diagram adopted for the simulation runs

7.2 Simulation studies

In the following sections, the results obtained from simulations based on the models presented in Section 7.1 will be discussed. Simulations were run following the procedure described in the previous Section 7.1.5. Following the procedure sequence, Section 7.2.1 will firstly deal with the simulation of resin curing and energy balance between the processed material and the metal die. In Section 7.2.2, the results for the flow behavior within the two modelled dies will be discussed by considering a comparison with analytical models and experimental results. At last, simulations run with different model parameters will be analyzed and the implications to die design will be discussed in Section 7.2.3.

7.2.1 Evolution of curing reaction

Simulation of the thermal balance between the material being processed and the steel die is the first step in the simulation workflow. Most studies reporting similar simulations have limited the domain to the volume of composite material being processed, i.e. heat transfer between the composite material and the die was not considered. The wall temperature is in this case set to a fixed value or function. The feasibility of simulating the thermal balance

between the composite material, including the curing resin and the metal die was investigated in this study. The 2D conical die model and the 3D tear drop die model were employed.

For the 2D conical die model, experimental temperature data from trial configuration 1 (refer to Table 6.1, glass fiber volume content 64%, pulling speed 0.3 m/min, set temperature of heating zones 100 °C), shown in Figure 6.3, was used to validate the simulation. Fixed heat fluxes were set to the cooling and each of the heating zones. To find appropriate values of heat fluxes, a first simulation was run with fixed temperatures at the cooling zone (20 °C) and at heating zones (100 °C). The heat fluxes found by this simulation run are then used as an initial guess for an optimization procedure to minimize the differences between the temperature values measured by TCs, both located in the die and in the processed material, and simulation results. The same method described in Section 5.1.3.2 to minimize pressure residuals is applied in the optimization procedure.

Figure 7.16 shows the results of various simulations carried out with different set parameters. The target temperatures used for the optimization procedure are shown as blue (TCs located in the die body) and red (temperatures at the profile surface measured by wire TC) points. The temperature prediction within the composite material along the die agrees reasonably well with measured values. A better correlation is achieved by setting a Thermal Contact Resistance coefficient (TCR) at the interface between the composite and die. The profile surface temperature predictions from three simulation cases with different TCR values are plotted: (1) 0 m².K/W over the whole die length, (2) 0.005 m².K/W over the die length and (3) a variable TCR at different sections of the die (each section is 200 mm long), according to the values plotted in the right axis. It can be concluded that a variable TCR along the die length leads to a better correlation between temperatures as measured during processing and obtained from simulations. Such a qualitative correlation was also observed in [108]. In that study, a larger TCR in the region close to the die inlet was attributed to cooling channels which were not explicitly modelled. One possible explanation for the larger TCR in the inlet section found in the present study is a difference in material composition. The larger resin to fiber ratio, leads to a proportionally lower thermal conductivity at the tapered section. This effect is accentuated by the inhomogeneous distribution of the rovings, i.e. a resin-only film actually exists at the contact interface, in contrast with the simplified, homogeneous porous model.

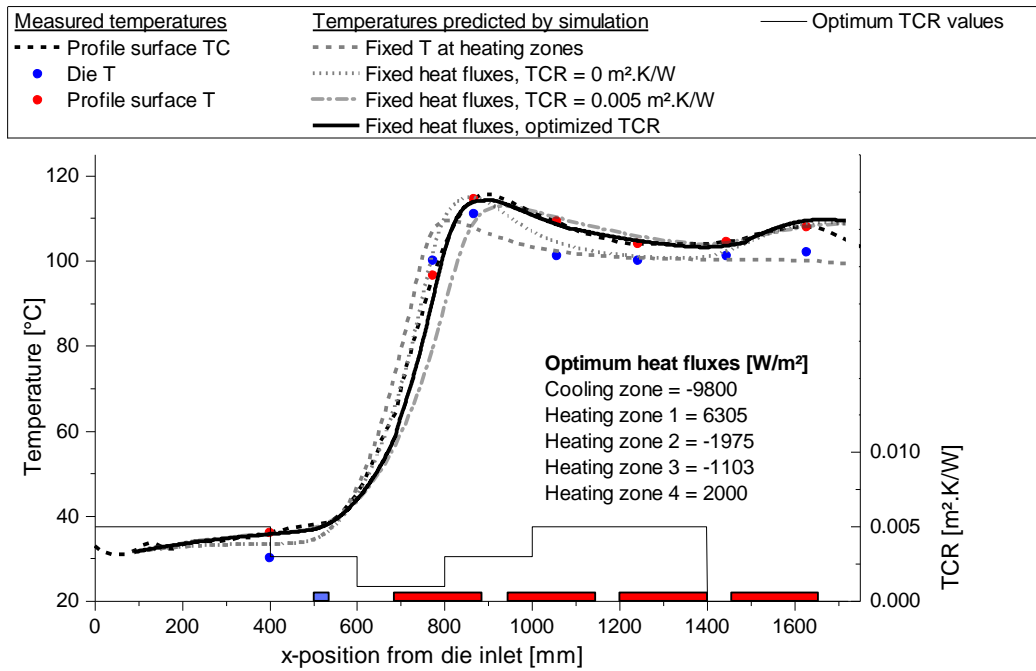


Figure 7.16: Temperature curves obtained from simulations of the conical die model with different set parameters

Figure 7.17 (top) shows a comparison of measured temperatures and the final simulation results of the conical die. The bars located close to the x-axis reflect the positions of the die cooling and heating zones. Good agreement is found between the measured temperature evolution and the simulation results. Some discrepancy is observed near the exothermic peak, where the predicted temperature increase is steeper than the experimental results. Towards the downstream section there is another slight temperature increase in the fourth heating zone, which is also not accurately reproduced by the simulation. In this section, TC measurements in the die body show a lower value than predicted by simulation. However, the temperature prediction within the processed material is close to the experimental data, allowing for a realistic prediction of the degree of cure at the end of the die.

Figure 7.17 (bottom) shows the calculated degree of cure and viscosity evolution for the conical die. A considerable portion of the reaction already takes place in the conical region, as can be seen by both the increasing temperatures, as well as in the predicted degree of cure. By the end of the conical section ($x = 500$ mm) approximately 5% conversion, i.e. about 17% of the B-staging reaction, is reached. However, viscosity remains low (under 1 Pa·s) within the length of the conical region, which is a decisive factor for stable processing. It can be seen that a viscosity drop occurs upon reaching the first heating zone, where the temperature increase (Arrhenius relation) effect in the viscosity exceeds the reciprocal network formation effect. This is immediately followed by a steep viscosity increase indicating gelation at a distance of approximately 850 mm from the die inlet. Furthermore, a stable

processing to a B-stage product is reached, since the degree of cure approaches a plateau at approximately 28% conversion, yet not triggering the second reaction step.

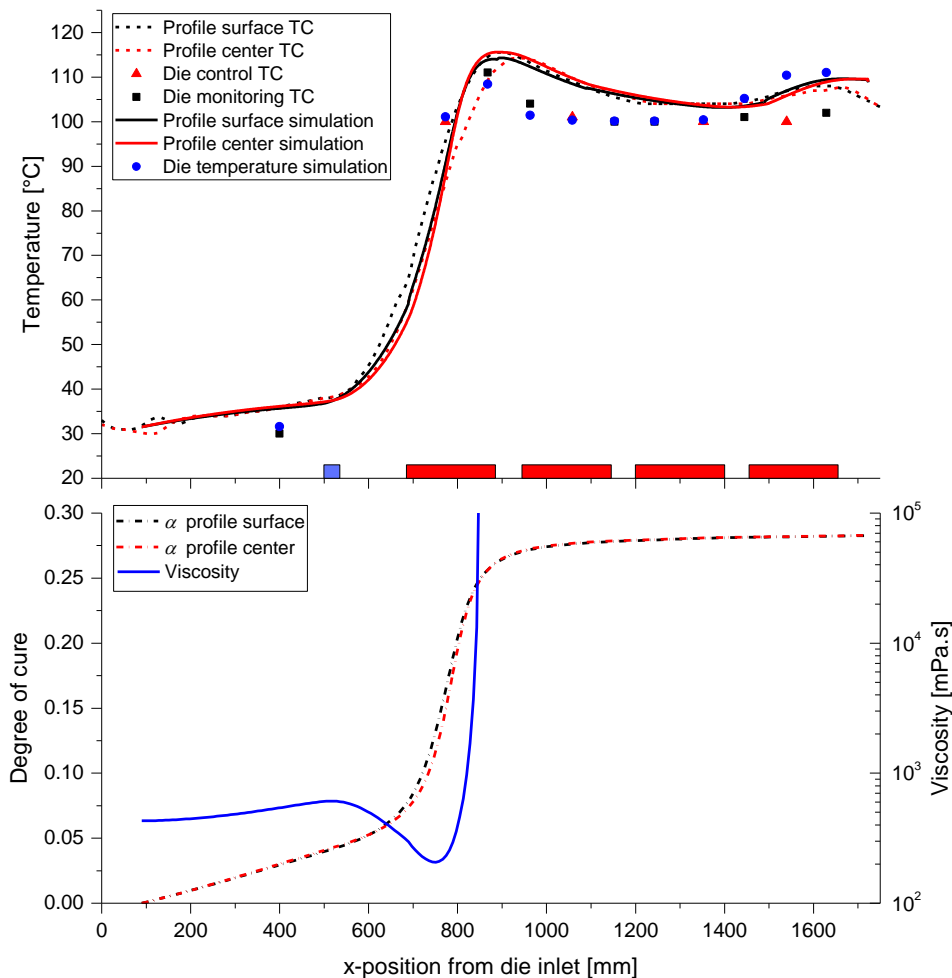


Figure 7.17: Top: comparison of experimental temperature data and simulation results along the length of the conical die for trial configuration 1 (refer to Table 6.1); bottom: predicted degree of cure and calculated viscosity along the die length

Comparison of the heat fluxes obtained from experimental data and simulation reveals that the thermal balance in the metal die is not realistically reproduced, at least by the 2D simulation. The heat flux from heating plates in zones 2 and 3 is close to zero (marginally positive), while simulation results point out to a net heat flux out of the domain in these regions. The pultrusion die has a larger surface area in contact to the ambient air (top area between heating plates and side faces) than the 2D design. The heat dissipation is therefore more constrained in the simulation model. Consequently, heating zones 2 and 3 act as a heat sink to achieve a satisfactory energy balance within the composite material, i.e. to obtain temperature prediction curves similar to measured data. The 3D simulation is expected to deliver better results for the thermal balance, since the dimensions and

positioning of cooling and heating zones are designed according to the experimental assembly.

A simulation was run with a reinforcement stack composed of an outer mat and an inner roving layer. Refer to Figure 7.8 for the distribution of the reinforcement within the die cavity. No experimental data is available for this configuration. The TCR values were kept at the optimized values shown in Figure 7.16. The heat flux of the cooling plate was kept at the same value of -9800 W/m^2 and the fluxes at the heating zones were adjusted to reach the set temperature of $100 \text{ }^\circ\text{C}$ at all control TCs. Results are shown in Figure 7.18. A higher exothermic peak can be distinguished in comparison to the unidirectional fiber stack case, which is due to the higher reacting mass. Another important difference is that higher gradients in the degree of cure and viscosity between the center and the surface line arise. However, the second reaction step does not set on. In this case, assuming an average viscosity as a function of the position along the x axis would expectedly lead to larger errors in the prediction of flow. The viscosity must be implemented in the CFX-Preprocessor as a spatial function of x and y.

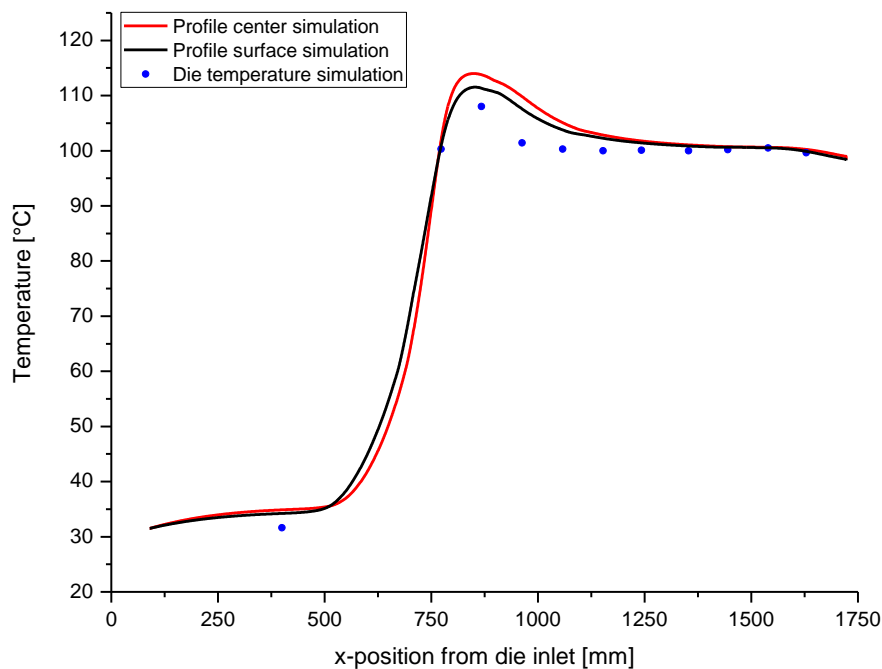


Figure 7.18: Simulation results for the temperature evolution of a profile with a CFM / roving reinforcement stack while processing in the conical die

The same optimization procedure was conducted for the tear drop die model to obtain a temperature evolution that fits experimental data. Results of the best fit are shown in Figure 7.19.

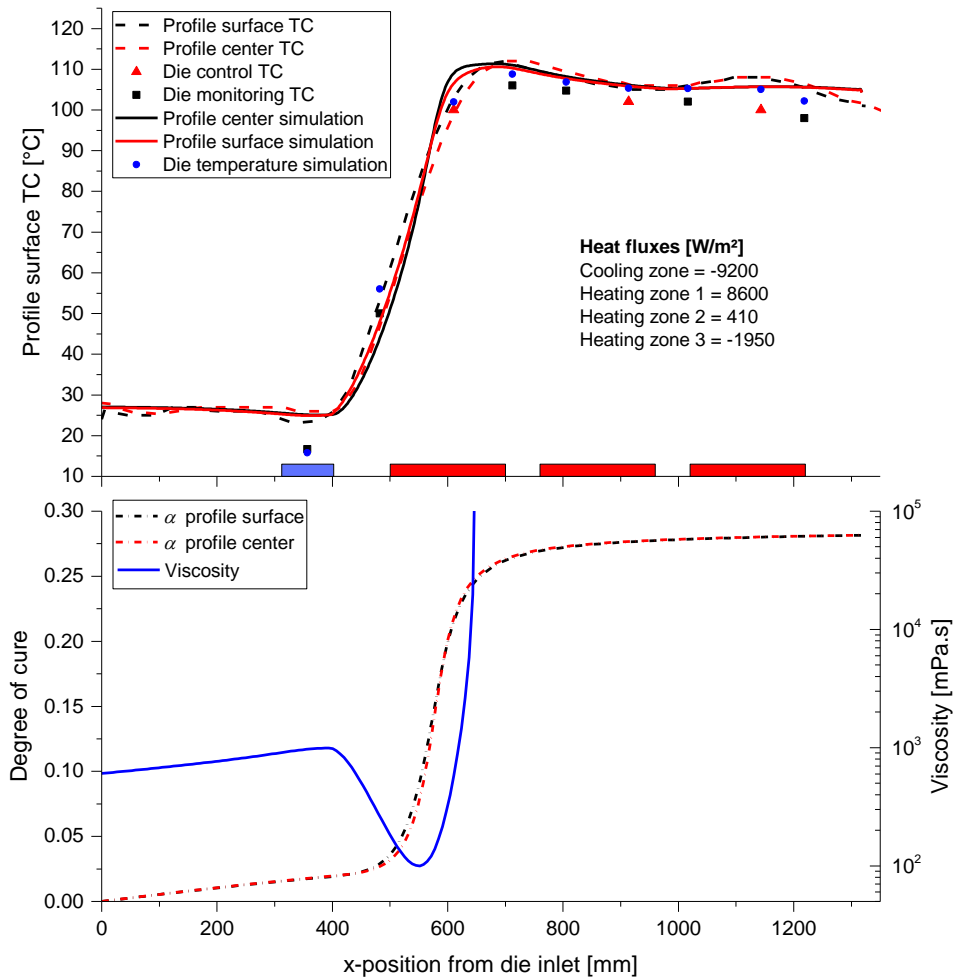


Figure 7.19: Top: comparison of experimental temperature data and simulation results along the length of the tear drop die for trial configuration 9 (refer to Table 6.1); bottom: predicted degree of cure and calculated viscosity along the die length

In this case, a better correlation is reached between the power inputs of the heating plates as logged during experiments (see Figure 6.8) and predicted by the simulation, at least in qualitative terms. A quantitative validation is not feasible at this stage; for such a comparison, experimental electrical output data (apparent and effective power) would need to be measured separately for each heating zone during a processing trial.

7.2.2 Flow behavior of liquid resin

Successful processing of a profile by means of closed injection pultrusion is determined by the flow of liquid resin relative to the moving reinforcement stack. In this case, the compacted stack must be thoroughly wetted within a short impregnation chamber length containing a relatively small resin volume. Understanding the aspects of resin flow are therefore of vital importance in designing an appropriate injection and impregnation chamber for a particular die. It is also evident that such a design will be intrinsically dependent on the

material being processed, i.e. the characteristics of resin and fiber stack, especially the properties examined in this work (see Sections 4 and 5). The following sections deal with such aspects. A comparison is made between results obtained by the presently developed model and analytic models available in the literature. The velocity and pressure fields obtained from simulations of both die models are then examined in terms of plausibility and agreement with experimental observations.

7.2.2.1 Comparison with analytic models

Two previous models described in the literature [10] [27] were used to compare simulation results obtained with the present model for the conical die. Both studies present analytical equations for obtaining the pressure rise function along a conical tapered section, based on a simplification assumption of 1D flow. The analytical model presented by Kim et al. [27] is described by Equation 3.30. The pressure rise is caused by the so called drag effect i.e. the effect of backflow of a relatively high viscous fluid through a porous medium with finite permeability governed by the Darcy's law, in combination with a contracting cross-sectional area.

A simulation run was set to solely evaluate the pressure rise and compare to the model prediction. The geometry studied is presented in Section 7.1.1.1 Atmospheric pressure is defined at the inlet boundary. The Gebart model was set for the permeability dependency. A constant viscosity of 400 mPa·s and a pulling speed of 0.3 m/min were defined. The transverse permeability was varied in the CFX model to evaluate the validity of the 1D flow assumption of the analytic model. One simulation was run with permeabilities K_1 in the longitudinal fiber orientation and K_2 transverse to the fibers set as determined in Section 5.3.2, and another one with isotropic permeability, i.e. K_1 was set in both orientations.

Figure 7.20 shows the results obtained by the CFX simulations and calculated by the analytical model. The pressure rise curves obtained from CFX simulations with different permeabilities are exactly the same and overlap with the analytic model results, indicating that the 1D flow assumption is good for the pressure rise prediction. It should however be noticed that the simulation in this case is based on a single phase system, i.e. it is assumed that the whole tapered volume is filled with resin.

In order to obtain a more realistic prediction of the pressure profile in the tapered section, it is useful to examine the analytical model proposed by Ding et al. [10]. The model was derived for a conical tapered die designed according to the patent by Gauchel [7], in which the resin

is injected at the transition between conical and straight sections, .i.e. the location of maximum pressure. They also assumed a simplified 1D flow, and argued that the pressure rise in the injection case is caused by two superimposed effects: the drag flow and a flow caused by the injection pressure. They then deduce an explicit formulation for the pressure function, which can be solved for a given flow front position or an injection pressure. The analytical solution was compared with a CFX simulation by applying a multiphase material model composed of air and resin. The anisotropic permeability case, as well as the same remaining parameters as the single phase simulation were set, and an injection pressure of 150 bar at the transition at the conical-straight junction was defined. The results are also plotted in Figure 7.20. Very good agreement between the analytical model and the numerical simulation is also observed for the injection case. A flow front at a position of 165 mm is found for this simulation case.

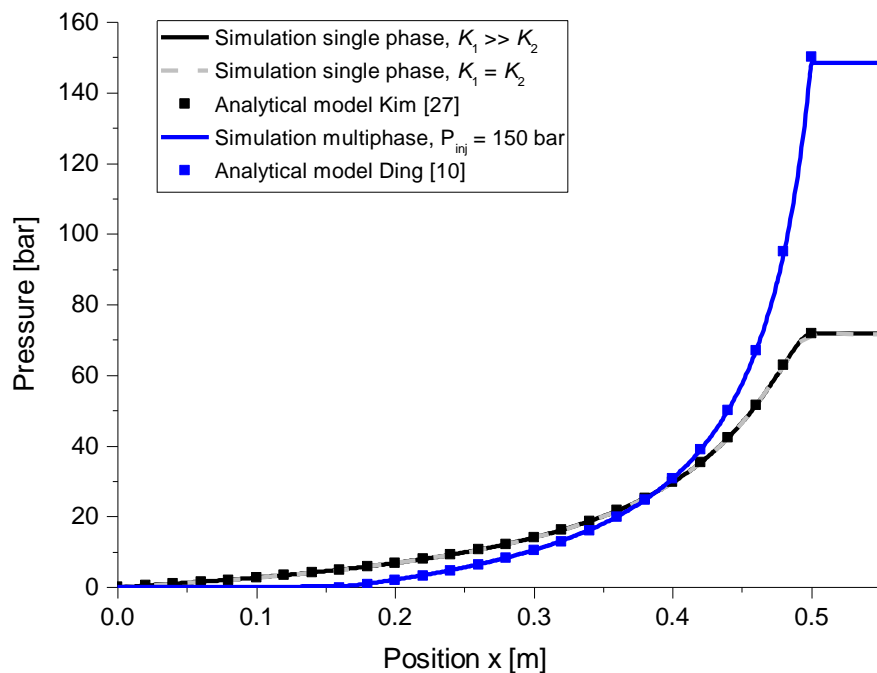


Figure 7.20: Comparison of pressure rise curves calculated according to the analytical model proposed by Kim [27] and Ding [10] and by simulations in CFX

By analysis of the above plots, it can be stated that injecting the resin at the junction between conical and straight sections is counterproductive, due to the large pressure needed to obtain a flow front at a x position with reasonable distance from the injection point and thus provide the resin with a long enough impregnation length. It should be stressed at this point, that the pressure rise is explicitly dependent on material composition and pulling speed. The unidirectional fiber stack represents a limiting case in terms of (low) permeability and overall (high) fiber volume ratio, though very common in real pultrusion applications. On the other

hand, a relatively low viscosity value was set in the calculations; Viscosities in the range of 1 to 4 Pa·s are typical for UP and VE pultrusion formulations [4]. The pulling speed is also relatively low, comparing to typical production speeds of 1 m/min. Table 7.5 lists the injection pressure calculated by the Ding model from different processing parameters and a given flow front located at $x = 150$ mm. The die geometric parameters are the same as the previous simulation. The values of fiber volume content and permeability refer to the final value within the constant cross section. The permeability function for the CFM / rovings / CFM stacks was obtained by a weighted average from the values shown in Figure 7.8. The values in bold indicate the parameters varied from the base case 1.

The calculated injection pressures reinforce the above statement that pultrusion with this die design is not feasible for the stable processing of unidirectional fiber stacks. The theoretical needed injection pressure is too large, though in practical terms a lateral shifting of rovings near the injection nozzles would be unavoidable, leading to race tracking of resin in the upstream direction and insufficient wetting of fibers. On the other hand, laminates composed of a mat / rovings / mat stack sequence show lower injection pressures and may thus be processed with this die configuration. The application of mats also has the advantages of acting as a flow and resin distribution aid in the transverse direction and limiting lateral shifting of rovings. This fiber stack configuration as also chosen for the experimental studies reported in [10].

Table 7.5: Calculated injection pressures for a tapered die with injection at the junction between conical and straight section and different processing parameters

	Case number						
	1	2	3	4	6	7	8
Reinforcement stack *	<i>R</i>	<i>R</i>	<i>R</i>	<i>R</i>	<i>M/R/M</i>	<i>M/R/M</i>	<i>M/R/M</i>
Fiber volume content	0.64	0.60	0.64	0.64	0.49	0.49	0.49
Permeability [$\times 10^{-12}$ m ²]	1.8	2.8	1.8	1.8	87	87	87
Resin viscosity [Pa·s]	0.4	0.4	1.0	0.4	0.4	1.0	0.4
Pulling speed [m/min]	0.3	0.3	0.3	1.0	0.3	0.3	1.0
Injection pressure [bar]	151	118	377	502	9.5	24	32

* *R* = unidirectional rovings fiber stack;

M/R/M = outer CFM layers (M8643 300 g/m²) and inner roving layer (83 rovings).

To overcome this limitation, newly designed conical geometries for pultrusion dies have applied one or more injection ports at some position in the conical section, e.g. the die presented in Section 6.1.1. It is evident that in this case a combination of both analytical

models should deliver a better representation of the pressure function. Upstream of the injection port position, the superimposed drag and pressure flows must be considered, to account for the flow front balance at steady state. Downstream of the injection location, pure drag flow is expected; since the pressure is larger than at the injection, no pressure-driven flow will take place in this section. To validate this hypothesis, further multiphase simulations were run. The parameter configuration was the same as the previously discussed, the only difference being the position along the x axis of the injection port and the injection pressure. For the first simulation, the injection port is located at $x = 200$ mm, and an injection pressure of 1 bar is set. For the second simulation, $x = 450$ mm and the injection pressure is 60 bar. The results are plotted in Figure 7.21.

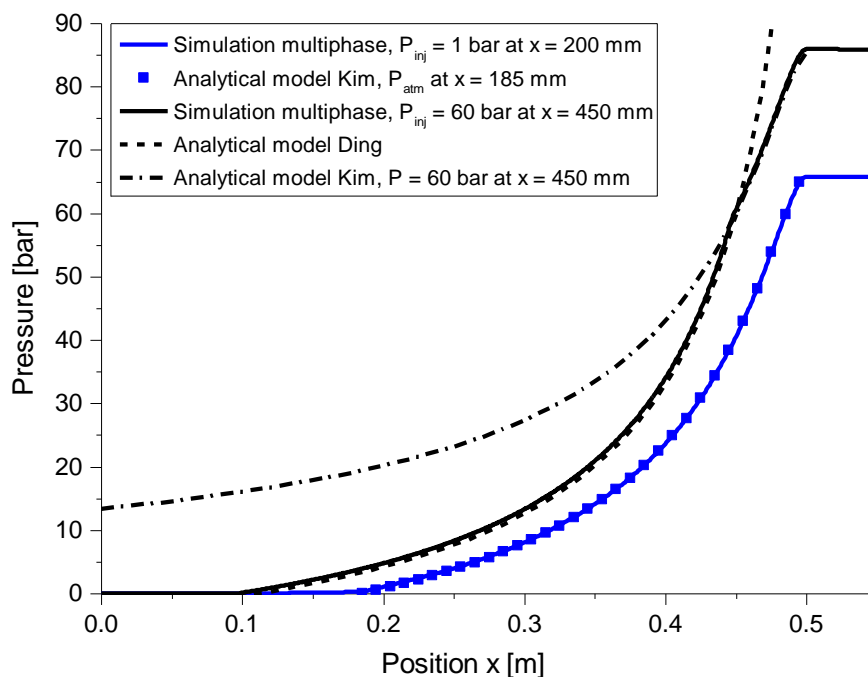


Figure 7.21: Comparison of pressure rise curves calculated according to the analytical models by Kim and Ding and simulations in CFX for a conical inlet geometry with injection port located at different positions in the conical section

The validity of the hypothesis is clearly attested by the coinciding results. Considering an injection configuration under a low pressure, the pressure curve can be well approximated by Kim's model alone, since the upstream distance between injection port and flow front is very short, in this case only about 15 mm. The solution to Kim's model was calculated by setting atmospheric pressure at the position $x = 185$ mm. By moving the injection port downstream and applying a higher injection pressure, the pressure-driven flow component will become significant, so that a combination of both models can be applied to predict the pressure curve.

In summary, the 1D flow simplification and the analytical models proposed by Kim and Ding provide an easy and accurate way to predict the pressure rise in a conical inlet section of a pultrusion die, provided that the tapering angle is small ($\sim 1^\circ$). The effect of a much lower transverse permeability has been found to be negligible, and a combination of both models has been proven to deliver results consistent with simulations for an arbitrary position of the injection port along the x axis. A derivation of an explicit pressure function for a given injection port and pressure can be found in Appendix C.

7.2.2.2 Flow behavior in the conical inlet section

The experimental results have shown that a considerable pressure rise results from pulling of the material through the tapered chamber, even for the relatively low pulling speed set during the trials. The thermal simulation results indicate that stable processing is feasible for the cooler/heater configuration and set temperatures. The discussion of analytic models in the previous section has indicated that the predicted pressure rise is in qualitative agreement with experimental results. Furthermore, it was found that the permeability in transverse direction K_2 has no noticeable impact in the pressure rise function. On the other hand, it is expected that the chosen model for the longitudinal permeability K_1 will have a significant effect on the pressure rise. To evaluate the magnitude of this effect, a comparison was made between simulations run under the processing conditions of trial configuration 1 (64% vol. glass fibers and 0.3 m/min) and different model assumptions for the permeability. The results are plotted in Figure 7.22.

Comparison of the results shows that, for a glass fiber stack, the permeability function using the Gebart model with an effective fiber diameter of 27 μm , as experimentally estimated for a similar fiber stack (see Section 5.3.2), results in a relatively good correlation to the measured pressure in the straight die region. The pressure prediction assuming a constant viscosity of 0.4 Pa·s is also plotted for comparison purposes. From observation of the peak pressures close to the junction from tapered to straight section, it can be stated that a more realistic pressure prediction is obtained by taking into account the viscosity evolution of liquid resin up to the gel point. The discrepancy found for the pressure transducer in the tapered region is attributed to the actual distribution of the fiber stack not being uniform as modelled, but rather assembled in bundles. This distribution leaves comparatively more space and less resistance for resin flow around the bundles.

By applying the nominal glass fiber diameter of $24\ \mu\text{m}$ to the Gebart model, a considerable difference of approximately 17 bar is already obtained for the peak pressure. By using the model proposed by Westhuizen and Du Plessis [75], the discrepancy in the peak pressure is even larger. The shape of the pressure rise curve is also distinct. This is due to differences in the predicted permeability for low fiber volume contents. In contrast to LCM processes, in which the volume content remains constant throughout processing, a large variation in permeability is observed in the closed injection pultrusion case. It should be noted that experimental validation of permeability models has been done only for high volume contents, in this work as well as in previous studies. In practical terms, a fiber stack of low volume content will not approach a homogeneous porous medium, the flow will rather be driven by race tracking between individual rovings and/or roving bundles. The selection of a particular permeability model is therefore somewhat arbitrary. Nevertheless, supported by the qualitative agreement between simulation and measured pressure values, the Gebart model with the adjusted equivalent fiber diameter will be used for the remaining analysis.

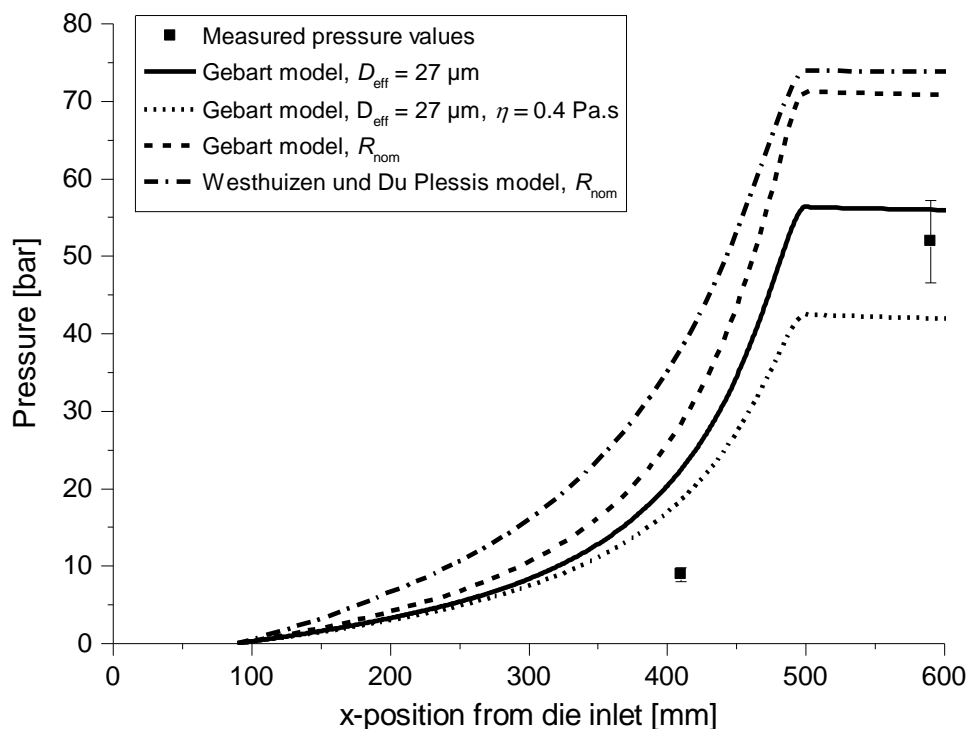


Figure 7.22: Comparison between simulations with the conical die and different permeability model assumptions

Figure 7.23 shows the pressure rise curves corresponding to different fiber volume contents and the same pulling speed (experimental trial configurations 1 to 3). The pressure is plotted up to the gel point calculated for each trial configuration. Upon reaching the gel point, the

matrix consists of an incipient polymer network, therefore the liquid pressure vanishes. It should be noted, however, that a small gradient actually exists between reaching of the gel point at the profile surface and centerline. This gradient is disregarded in the model, as the viscosity function is obtained by averaging the calculated viscosities at the surface and centerline.

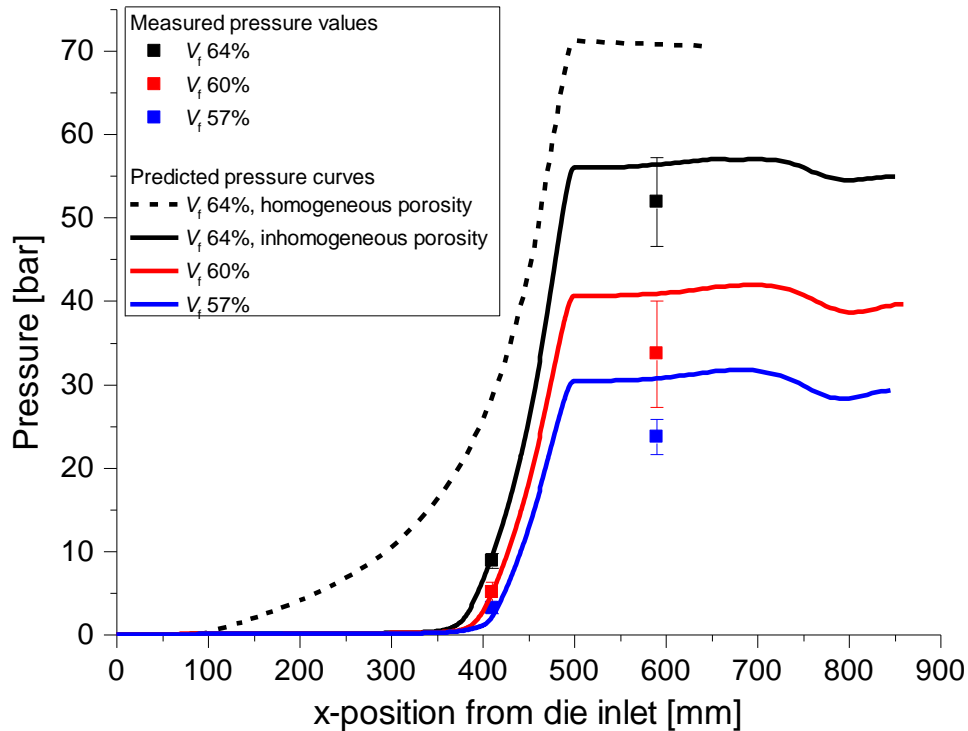


Figure 7.23: Predicted pressure distribution along the conical die length for trial configurations 1 to 3 up to the gel point

A good agreement between measured values by the pressure transducer located at the tapered region and simulation results, indicating that the proposed model accounting for an inhomogeneous fiber distribution delivers a good estimate of the pressure rise. In all cases, the peak pressure predicted by simulation is higher than measurement values, and the deviation between predicted and measured pressures increases with decreasing fiber volume content. This is probably caused by a higher inhomogeneity of fiber distribution with decreasing volume content. In other words, by reducing the final volume content, the fibers are not distributed evenly within the profile section, but rather tend to form agglomerates. This in turn results in resin-rich regions providing a preferred flow path in an opposite direction to pulling, and thus in an overall lower pressure level during the experiments.

It should be noted that relatively large pressure fluctuations were measured in all experimental trials, as indicated by the error bars. A probable cause for these fluctuations

could be a “breathing die” effect. The large pressures resulting from drag flow may cause the following cyclic effect:

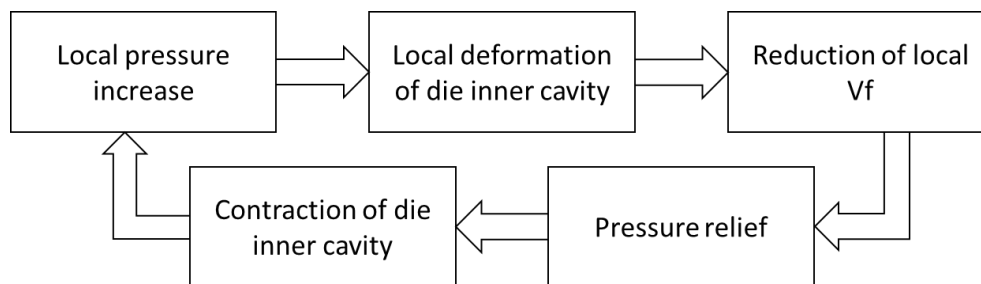


Figure 7.24: Cyclic “breathing die” effect resulting from large liquid pressures inside the die

This hypothesis is supported by the fact that during experimental trials, liquid resin leaks are observed at the die split line, i.e. the pressure is sufficient to create a small gap between die halves. Deformation of the die body has also been observed during pultrusion experiments by means of changing of value of a dial gauge in contact to the upper die half. This effect, however, has not been systematically measured for different trials configurations.

This is a typical Fluid-Structure interaction (FSI) problem. This is clearly a very important issue because it directly affects the final part properties in terms of fiber volume content and dimensional tolerances, which may be crucial depending on the application. Design guides provided by pultrusion companies already give quite large tolerances (e.g. 0.3 mm in thickness), for standard profiles produced by the standard open bath method, in which pressure levels are typically lower (in the range of 10 bar [107]). For the injection case with this specific die geometry, the problem is expected to be accentuated.

The pressure variations in the straight die section is caused solely by thermal expansion and cure shrinkage effects. This variation amounts to approximately ± 1 bar and is thus relatively small in view of the absolute pressure reached by pulling of the material along the constraining channel. Nevertheless, the pressure evolution along the straight section may also affect the profile quality.

The impregnation quality is directly related to the pressure evolution in the closed injection case. Freed [32] argued that, for the standard pultrusion process, small pressure gradients arising in the liquid region due to thermal expansion are important for expelling air entrapped in the processed material, i.e. in creating a preferred flow path towards the die inlet. For the closed injection case, the pressure gradient is determined not only by the thermal expansion in the straight section, but also on the pressure rise in the tapered region. By creating a large pressure gradient, resin is forced to flow against the pulling direction, thus wetting the

reinforcement stack. Figure 7.25 shows a plot of the pressure gradient at the center line against the x-position for the trial configuration 1. Below the plot, the corresponding region is displayed as a pressure contour plot together with vector arrows corresponding to the local pressure gradients. The x-axis scales of the graph and the contour plot are aligned; the out-of-plane axis of the contour plot is scaled up for visualization purposes.

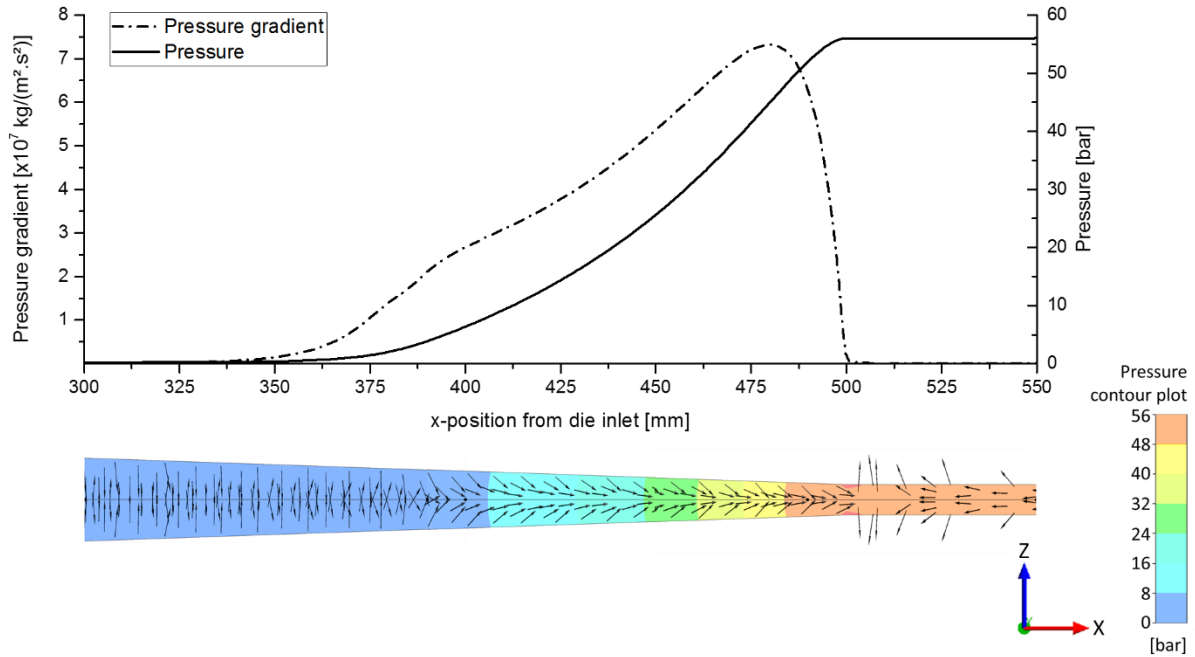


Figure 7.25: Top: center line pressure and pressure gradient plot for trial configuration 1; bottom: pressure contour plot and vector arrows indicating local pressure gradients

It can be seen that the pressure gradient reaches a maximum shortly before the transition edge ($x = 480$ mm). It is expected that entrapped air will flow against the pressure gradient vector, i.e. in the direction of pressure decrease. This process is facilitated in the tapered region between approximately 350 mm distance from the die inlet up to the transition to the curing section of the die. In the region immediately after the transition, it is expected that further air release is hindered due to a slight pressure decrease after reaching a maximum at the transition edge. This can also be seen by the vector arrows pointing to the left direction between 500 mm and 550 mm. One way to improve air release also in the straight section would be to optimize the positioning of heating plates and/or remove or reduce the cooling power, such that thermal expansion would lead to further pressure increase immediately after the transition conical-straight. However, such a modification of the trial assembly would potentially increase premature curing of resin in the tapered section, and thus reduce processing stability.

7.2.2.3 Flow behavior in the tear drop impregnation section

The tear drop cavity has a more complex geometry, and no previous publication containing a corresponding modelling attempt has been found during the literature research. The simulation results for trial configuration 8 are shown in Figure 7.26. The porosity and permeability as defined according to the different region assignments listed in Table 7.4. For comparison purposes, another simulation run was conducted by setting the thickness and permeability of the fiber stack along the impregnation chamber to the same value as in the inlet and curing sections. The reason for this comparison was to evaluate whether the simulation setting may be simplified, because in this case a subdivision of porosity and permeability regions according to Table 7.4 is not necessary. An inlet boundary condition of 1.3 bar constant pressure was set, corresponding to the measured value of pressure transducer 1.

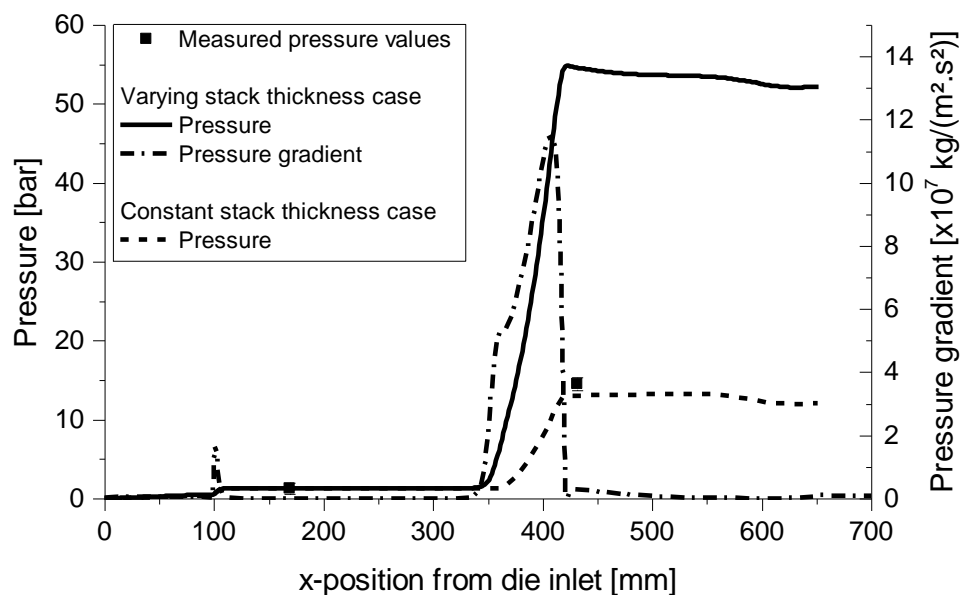


Figure 7.26: Predicted pressure and pressure gradient along the tear drop die center line for trial configuration 8 up to the detachment point

The centerline pressure remains practically constant along the injection region up to the point where the fiber stack is compressed towards the end of the tapered region (see Figure 7.9). The predicted pressure level at the end of the tapered section is higher than the measured signal. Comparison of results obtained from the simulation run assuming a constant stack thickness indicate that the simulation set according to the simpler assumption slightly underestimates the pressure evolution along the impregnation region.

It can be concluded that the proposed model does not reproduce well the process conditions observed during experimental trials. A number of factors are likely to play a role in the non-applicability of the model:

- Deformation of the die cavity under liquid pressure. As previously discussed, although the absolute liquid pressure is lower in comparison to the reached pressure levels within the conical die, the inner cavity of the tear drop die has twice the width of the conical die and the die body has a smaller thickness (36 mm each die half vs 45 mm of the conical die).
- Insufficient liquid impregnation of the reinforcement material. The model assumes a single liquid phase and therefore a perfect filling of the liquid portion in the porous domains. The presence of large dry spots may eventually reduce the pressure level in the chamber. Support for this supposition is given by the various micrographs, which have as a general rule shown lots of air pockets (see Figure 6.12 and Figure 6.14).
- Inhomogeneous distribution of porosity within the fiber stack. The model assumes a homogeneous fiber distribution of the fiber stack within the impregnation chamber. This might represent an oversimplification of the process. The much lower pressure rise obtained from the simulation assuming a constant stack thickness throughout the whole die is indication of this hypothesis. It is evident from comparison of both simulation results and observation of the micrographs that a refined model assuming a porosity gradient across the stack thickness should deliver more realistic results.

The pressure gradient plot in Figure 7.26 shows a similar trend already seen for the conical die case. The pressure gradient vectors show a favorable orientation for air release along the die entrance and the whole impregnation chamber, i.e. towards the die entrance (vectors not shown).

An important observation made during experimental trials with the tear drop assembly was the progressive clogging of the die, leading to complete obstruction of the impregnation chamber after a couple of hours (see Section 6.2.2). This is clear evidence that no steady state governs the flow of liquid resin within this region, but rather a transient condition prevails, in which the resin gradually cures at regions with presumably low local velocity. In other words, the geometric design is not optimized for this combination of fast curing resin system and processing conditions. Observation of the 3D flow field obtained from a steady state simulation provides insight of stagnation regions. Contour plots of a cross section at a position $x = 116$ mm from the die inlet, i.e. the location of the injection ports, and a longitudinal view are given in the following Figures. The plots were reflected over the XY plane for visualization purposes.

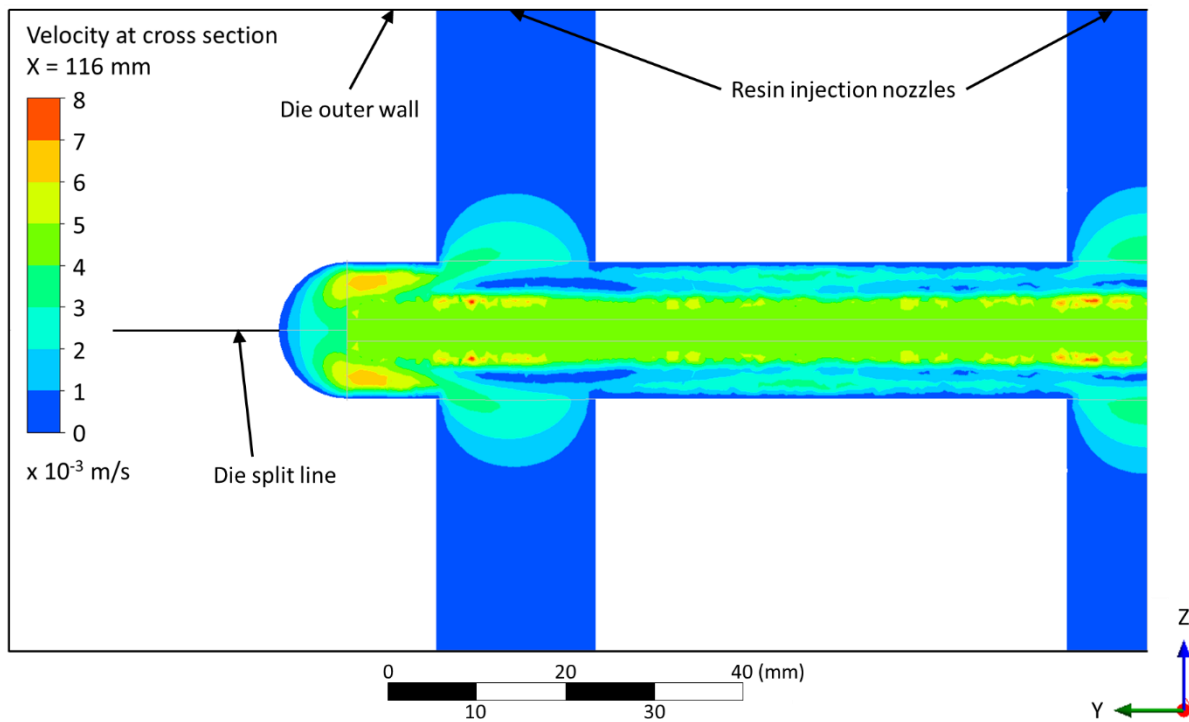


Figure 7.27: 2D contour plot showing velocity field in the cross section of the tear drop die where the injection ports are located

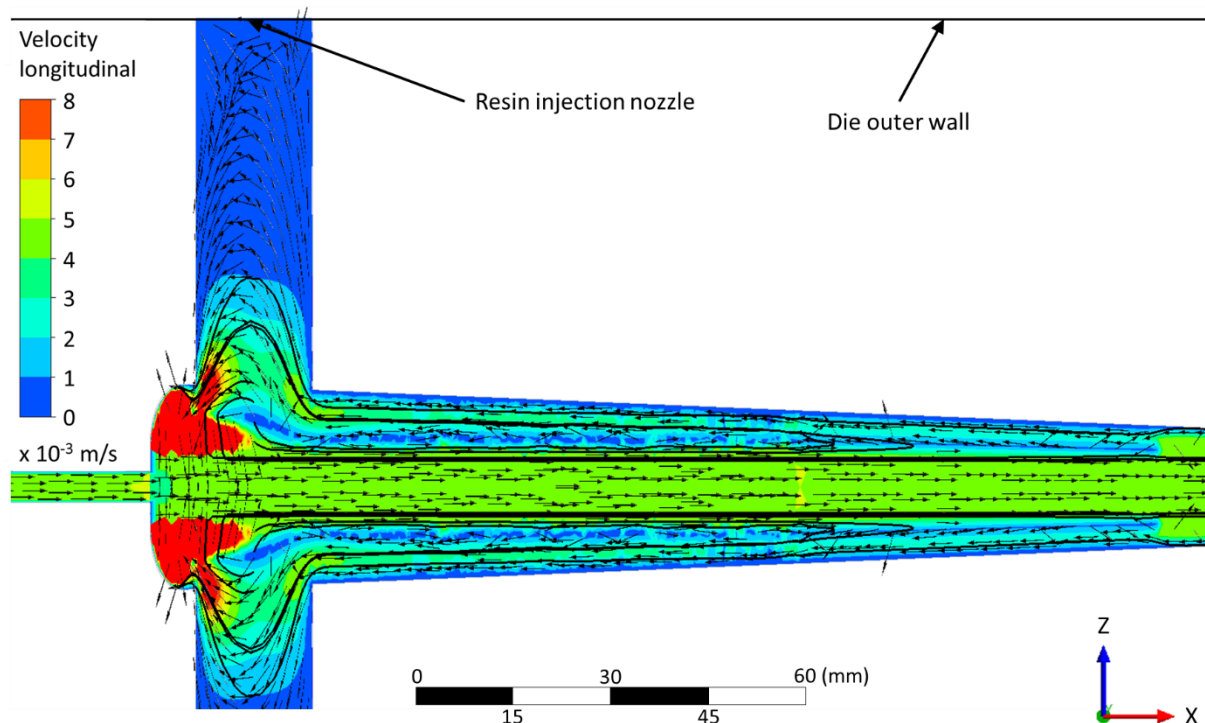


Figure 7.28: 2D contour plot showing the velocity field in a longitudinal view of the tear drop die middle plane (zoomed view near the injection location). Vectors show the local flow directions and streamlines the flow path from the starting points

Low local velocities are found in the regions near the tapered wall but also in the bulk of the fluid region. In the longitudinal plot, the neat resin region between the moving fiber stack and the tapered die wall can be clearly discerned as a backflow region. The region around the injection ports is characterized by swirling. The large diameter of the injection ports results in a stagnation volume with very low velocities. From this steady state result, the flow path and residence times for particles located in defined positions can be calculated. The flow path is shown by streamlines for five starting points located at $x = 116$ mm and different heights. It can be seen that the fluid can cover a large distance along the tapered section and flow back to the inlet region. It should be noted that the fluid flow within the impregnation region actually has a 3D pattern. The 2D representation in Figure 7.28 solely provides an easier visualization and physically only makes sense at the symmetry plane considered.

According to the flow paths described above, the particles are submitted to a specific temperature and consequently a curing history. Another way of evaluating the effect of stagnation regions on local curing would be to run transient simulations; however, such a transient analysis is not included in this work.

7.2.3 Parametrization of geometric design

In order to explore the impact of processing parameters and geometric design features on simulation predictions, a number of parametrization studies was conducted. For the conical die, the effect of varying the heat input / output to the die was analyzed, as well as the pulling speed. In terms of geometric design, the conical angle was varied, and simulated under the non-homogeneous porosity distribution assumption (see Figure 7.6). Additionally, the impact of die body thickness on the thermal balance was evaluated.

For the tear drop die, focus was given to modifying the chamber design in order to obtain less stagnation regions, i.e. to avoid low velocity pockets. The position and diameter of the injection nozzles, the length and tapering angle of the chamber were simulated in this case.

The impact of variations in the heat input to the die were evaluated modifying the base case (see Figure 7.17) by the following two scenarios: (1) removal of the cooling zone and (2) removal of the cooling zone, increase of the heat input by 30% in heating zones 1 and 4 and reduction of the heat output by 30% in heating zones 2 and 3. Comparison of these two scenarios with the base case is shown in Figure 7.29.

Removal of the cooling zone leads to a slight increase in temperature and degree of cure at the intersection between tapered and straight regions. This is however, according to the simulation, uncritical. The increase of heat input, on the other hand, results in an overall higher temperature plateau in the range of 130 – 140 °C and triggering of the second reaction step towards the end of the die. This is considered as an unstable processing condition, especially because the heat release from the curing reaction is expected to promote curing also after the material is pulled out of the die.

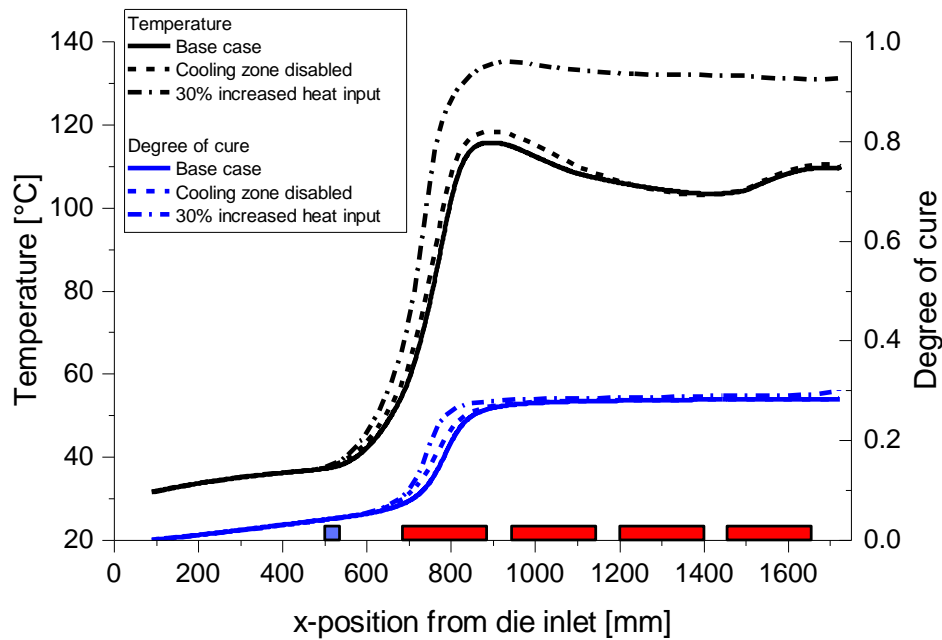


Figure 7.29: Comparison between simulation results of the conical die with different scenarios in terms of heat input / output to the die

The issue of the die inner cavity deformation, which has been discussed in Section 7.2.2.2, may in principle be minimized or eliminated by designing the die with thicker body halves. The original die half thickness of 45 mm was increased by 10% and 50% for comparison purposes. The results of temperature evolution along the die length from steady state simulations are plotted in Figure 7.30.

It can be stated that increasing the die body thickness is advantageous both in terms of reducing the cavity deformation as well as in terms of thermal management. By increasing the die thickness by 50%, the exothermic peak located between the first and second heating zones is distinctly reduced, i.e. the additional body mass is able to absorb more effectively the released reaction heat. On the other hand, the effect on the conversion progress is almost negligible. A slightly slower degree of cure evolution can be seen, and the curves approach the same plateau corresponding to the B-stage towards the end of the die. It

should be noted, however, that these results are based on steady state simulations. If one considers a process with varying temperature set points, a die with larger body mass is expected to take longer to reach a new steady state after changing the temperature setting. This should however not represent a limitation for pultrusion, which is supposed to run on stationary conditions.

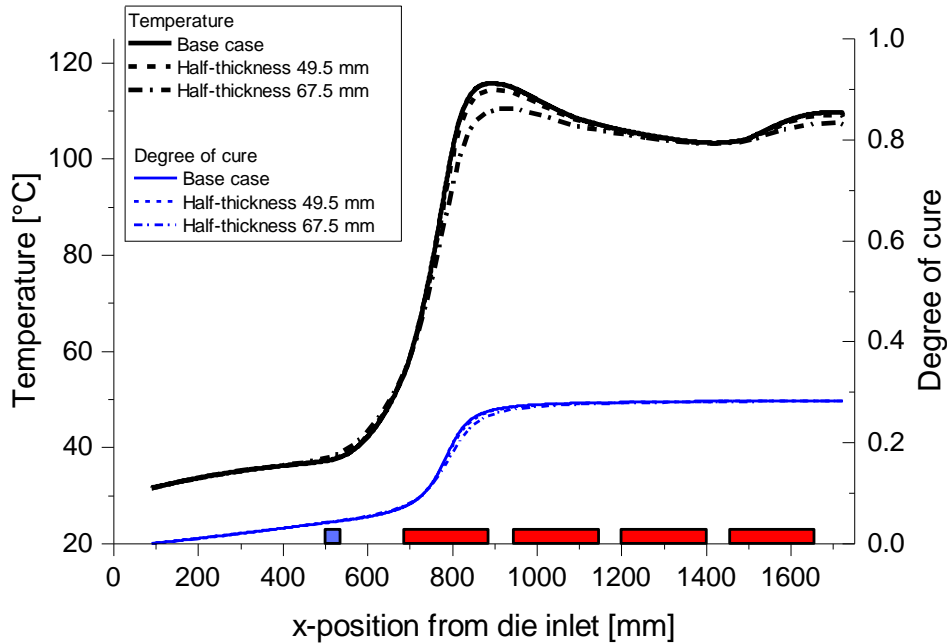


Figure 7.30: Comparison between thermal simulations results of the conical die with different die body thicknesses

Increasing the pulling speed is usually desired as a means to increase productivity. It is expected that the pulling speed will have a significant impact on the pressure rise within the tapered section. The effect of the pulling speed in the curing reaction evolution was evaluated by two simulations. On scenario 1, the pulling speed was increased to 0.5 m/min and the heat exchange through the cooling and heating zones was kept as the base case. On scenario 2, the heat input through the heating zones was changed in order to obtain the set temperature of 100 °C on the control TC corresponding to zones 1 through 3. The resulting curves of temperature, degree of cure and viscosity evolution along the center line are shown in Figure 7.31.

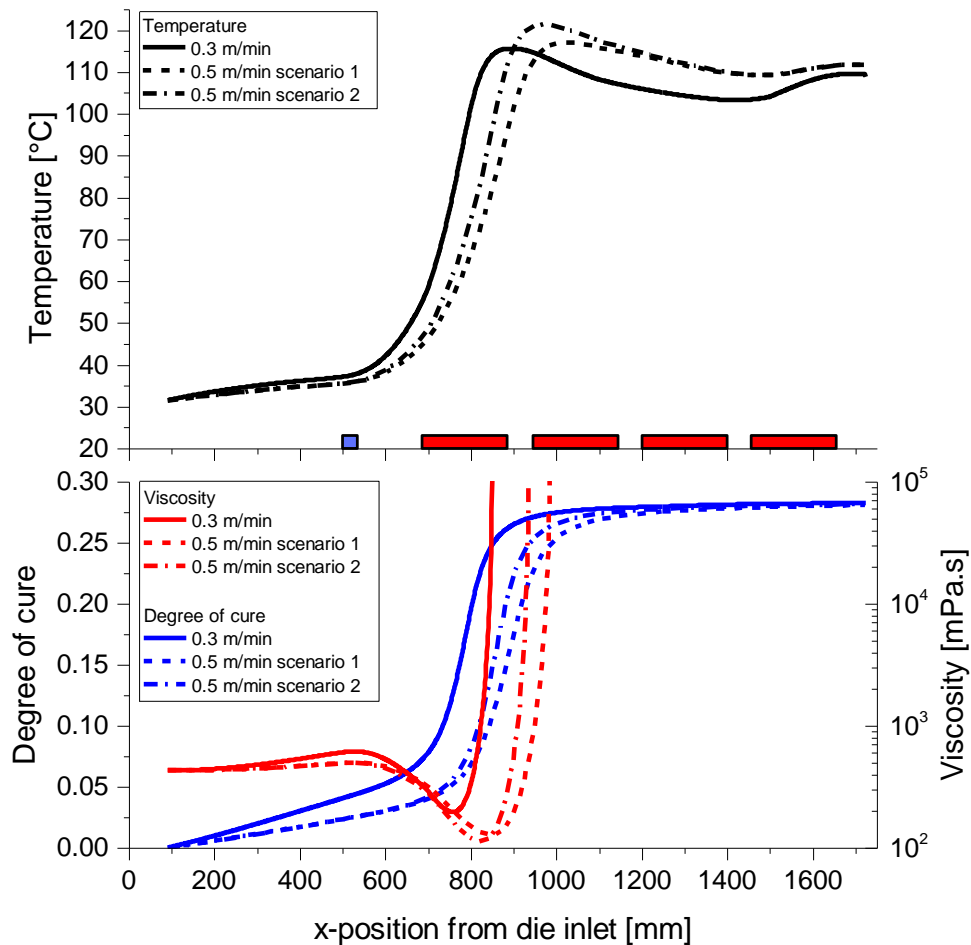


Figure 7.31: Comparison between thermal simulation results of the conical die with varying pulling speed

It can be seen that varying the pulling speed has a significant impact in the profile temperature evolution. For the higher pulling speed, heat accumulation in the profile leads to a higher temperature level in heating zones 2 and 3, considering the same heat input condition. Adjusting the thermal input in the heating zones such as to obtain similar set temperatures in the control thermocouples results in a more pronounced exothermic peak. Differences in the viscosity evolution as a result of temperature and degree of cure progress are also quite noticeable. The different viscosity evolution is expected to have an impact in the pressure rise in the conical section, together with the pressure caused by moving the reinforcement stack through the tapered section.

This correlation is explored in the following simulation scenarios: (1) increasing the pulling speed to 0.5 m/min, (2) changing the tapering angle to 1.2° for the base case speed of 0.3 m/min and (3) setting the tapering angle to 1.2° and the pulling speed to 0.5 m/min. Resulting plots are shown in Figure 7.32. A considerable dependence of the tapering angle on the pressure rise can be observed. Considering a pulling speed of 0.3 m/min, a difference

of 7 bar in the peak pressure is obtained, by increasing the pulling speed to 0.5 m/min the difference reaches approximately 13 bar.

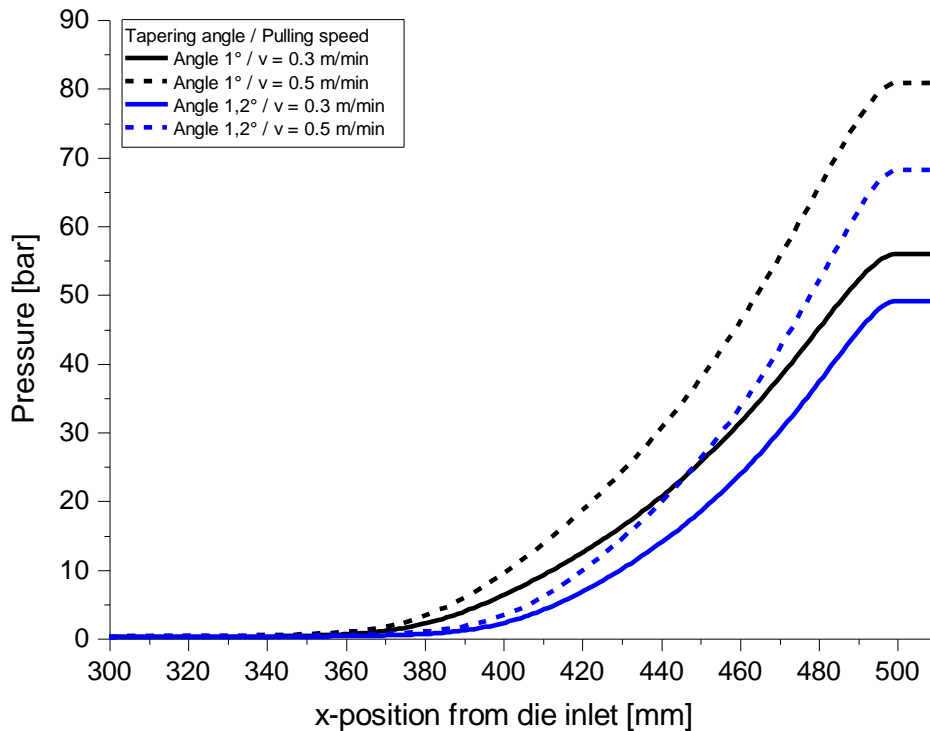


Figure 7.32: Comparison between simulations of the conical die with varying pulling speed and tapering angle

Parametrization studies based in the tear drop die design were conducted to explore the effect of design parameters on the flow field within the injection chamber. As experimentally observed, the available die in combination with the fast reacting resin system applied to this study results in an unstable processing condition. As time progresses, the resin chamber becomes clogged with gelled resin. Gelling presumably starts in regions with low local velocities (stagnation regions). Low local fluid flow was observed not only, as expected, at the wall of the impregnation chamber, but also in other pocket volumes along the chamber. This can be explained by the fact that the flow velocities are in general quite low, i.e. the flow regime is to a large extent laminar. This results in the appearance of a stagnation volume between the moving fiber stack and the backflow region.

In order to obtain a robust processing condition with long operating times, it is desirable to reduce and/or eliminate such stagnation volumes. In the subsequent parametrization studies, contour plots obtained from simulations with changed design parameters were compared to the base case (see Section 7.2.2.3). The position of the injection nozzles and tapering angle of the chamber were chosen as design parameters.

Simulation results for the tear drop die design replicating the actual die geometry has shown that the injection nozzle diameter is too large, resulting in a stagnation region and backflow as seen in Figure 7.28. In the following simulations, the nozzle diameter was reduced to 6 mm.

The velocity field in the longitudinal middle plane is shown for a case in which the tapering angle was reduced to 1° (against the base case angle of 1.2°) in Figure 7.33. An inlet boundary condition of constant pressure of 1.3 bar was set. A discontinuity is discernible in the velocity field at the position $x = 200$ mm from the die inlet. This is due to the interface between the domains 4 (with hexagonal elements) and 5 (with tetrahedral elements) (see Figure 7.4). For the base case, the effect of this interface is much less pronounced. However, the influence of this discontinuity may be assumed as negligible for the purpose of comparison of the flow fields.

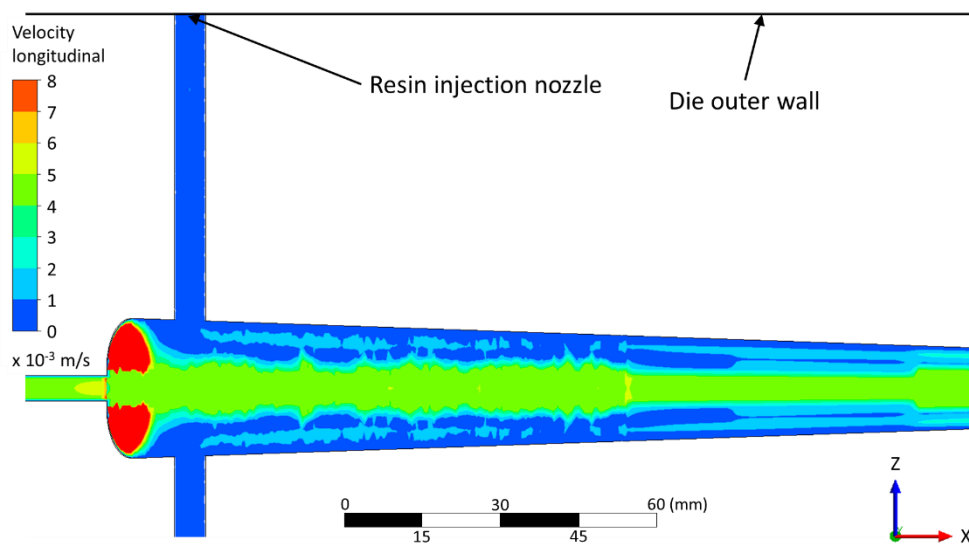


Figure 7.33: 2D contour plot showing velocity field in a longitudinal view of the tear drop die middle plane (zoomed view near the injection location) for a case with tapering angle of 1°

Comparison between Figure 7.33 and Figure 7.28 reveals a marginal changing of the velocity field near the nozzle channel discharge. Low velocity regions can still be found along the cavity, however, due to the reduced free volume between the reinforcement stack and the cavity inner walls, the overall stagnation volume is reduced.

The velocity field in the longitudinal middle plane is shown for three cases with different injection nozzle locations in Figure 7.34. In all cases the same inlet boundary condition of

constant pressure of 1.3 bar was set. A similar discontinuity already observed in the previous case is also visible in these comparison cases.

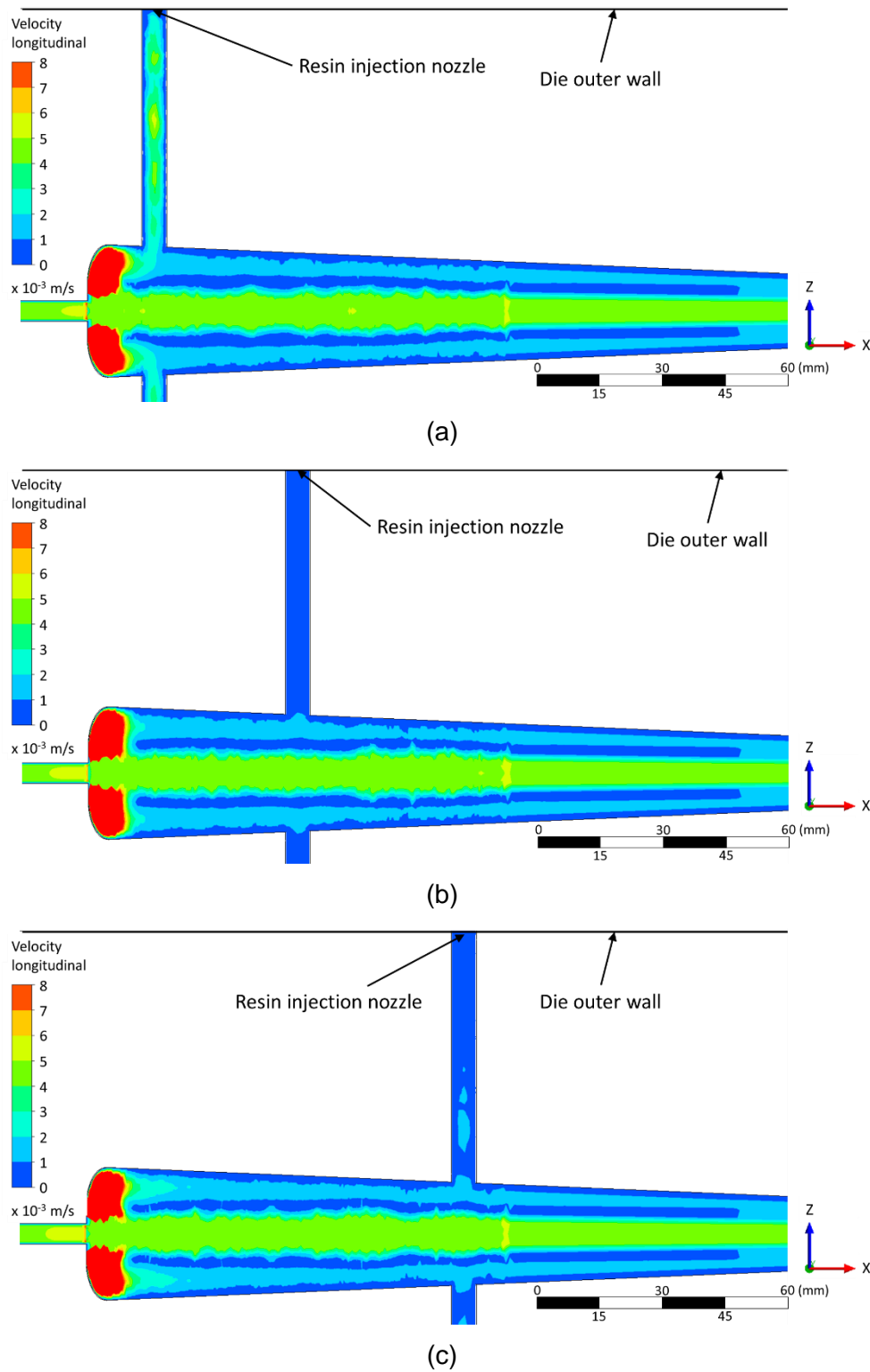


Figure 7.34: 2D contour plots showing velocity field in a longitudinal view of the tear drop die middle plane (zoomed view near the injection location) for three different injection nozzle locations: (a) $x = 116$ mm from die inlet, (b) $x = 150$ mm and (c) $x = 190$ mm

It can be stated that changing nozzle position along the x axis has little influence in the flow field within the impregnation chamber itself; however, the flow within the nozzle channel is influenced. By maintaining the nozzle in its original position (Figure 7.34 (a)), higher velocities are reached than in the comparing cases (b) and (c). This is possibly due to the fact that a vortex region is located close to the nozzle discharge, a condition which was already observed for the base case. It can be concluded that a reduction of the nozzle diameter would be advantageous in increasing local velocities and therefore reducing the risk of channel obstruction. On the other hand, the impact of designing the injection nozzles downstream of the base case position may be considered as negligible.

8 Conclusions and outlook

In this thesis, a holistic approach to the simulation of physical processes involved in pultrusion dies with a closed injection and impregnation cavity was developed. Most previously published studies have focused in only one aspect of such physical processes, i.e. reaction kinetics and energetics evolution (thermo-chemical approach), fluid dynamics or evolution of internal stress and distortions throughout curing (thermo-mechanical approach). Specifically, in this study, the thermo-chemical model is applied to obtain a more realistic prediction of the viscosity of the resin while it cures, i.e. coupling of the thermo-chemical and fluid dynamics model. Furthermore, the thermo-chemical and thermo-mechanical models are coupled to obtain a prediction of liquid pressure in the curing section of the die up to the point where the resin gels.

Different experimental characterization techniques were employed to obtain reliable material data to feed the simulation models. A fast reacting, two-step-curing resin system was characterized in terms of reaction kinetics by DSC and the viscosity evolution throughout curing was determined by rheology measurements. For this resin system, it was shown that taking into account the viscosity evolution is essential for obtaining realistic predictions for the flow behavior. The kinetics of the first reaction step leading to a B-stage intermediate product is rather fast, leading to a considerable conversion while the material is still in the injection and impregnation chamber. This, in turn, causes changes in the material viscosity. Simulation results for the pressure rise obtained by incorporating a varying viscosity agreed better with experimental results than results obtained under a constant viscosity assumption.

Reinforcement materials were characterized in terms of their compressibility, i.e. the elastic response of a fiber stack to a transverse mechanical load, and in-plane permeability. For the compressibility, reproducible results could be obtained for glass continuous filament mats, and stacks composed of glass fiber and carbon fiber rovings. It was argued that determining the compressibility of reinforcements is important for the process simulation of cases in which different materials are applied, e.g. a combination of CFM and roving layers. In such cases, the fiber volume content of each layer cannot be determined from the cavity cross section alone, it is rather a function of the mechanical pressure applied to the whole reinforcement stack.

The results for the experimental permeability characterization were less consistent. This material parameter is extremely sensitive to the fiber volume fraction. The developed method for in-plane characterization delivered results comparable to the literature in the case of

planar textiles. The determination of the permeability of roving stacks was, on the other hand, challenging due to the narrow range of measurable fiber volume fractions, in which a very restricted saturated flow takes place. The permeability along the fiber orientation agreed reasonably well with Gebart's theoretical model, while values for the traverse permeability were considerably lower than theoretically predicted for the same fiber volume content. Simulation studies comparing different permeability values showed that the flow field and pressure rise is very sensitive to the longitudinal permeability, but are practically not influenced by the transverse permeability.

Two pultrusion dies with different closed injection and impregnation chambers were modelled and simulated: one with a conical inlet geometry and another with a so-called tear drop injection and impregnation chamber. Experimental trials were conducted with both die assemblies in order to compare simulation results with real processing data.

The simulation model needs the definition of the porosity within the domain corresponding to the fiber stack over a broad range of fiber volume content. Two models were proposed for the case of the conical die: a simplified model assuming a homogeneous fiber distribution over the whole cavity cross section, and a model accounting for an inhomogeneous distribution of the reinforcement within the cross section.

The simulation results for the pressure rise in a conical injection chamber agree well with experimentally determined pressures for different fiber volume contents. This gives confidence in the validity of the developed model. The conical geometry study causes a pressure rise of the order of magnitude of 50 bar. Such a liquid pressure is expected to account for a considerable fraction of the pulling force. The direct correlation of measured pulling force and pressure signals is also indication of this behavior.

The predicted pressure rise is not in good agreement with experimental processing data in the case of the tear drop chamber, i.e. the predicted liquid pressure at the beginning of the straight curing section is higher. The discrepancy was attributed to a combination of different factors: deformation of the die cavity under liquid pressure, insufficient impregnation of the reinforcement stack and an oversimplification of the fiber stack distribution assumption.

Future work in this topic could include a coupling of the flow field with an elastic deformation model of the die body (Fluid-Structure Interaction). Since the high liquid pressures are, in contrast to the conventional pultrusion technique, characteristic of the closed injection pultrusion, a possible deformation of the die body should be considered in the simulation.

The importance of such an approach is justified by the high sensitivity of the permeability to variations in the die cavity and, consequently, in the fiber volume content.

Furthermore, efforts should be undertaken to study the correlation of the liquid pressure level and/or pressure gradient with the impregnation quality. In other words, the optimization of pressure rise or pressure gradient function should be sought. In general, a relatively low pressure level on the order of 10 – 20 bar would be preferable than 50 – 60 bar, which could be easily obtained by designing a slightly larger tapering angle. The question as to which pressure level and/or pressure increase rate is necessary to obtain a satisfactory impregnation quality can only be addressed by an extensive characterization study on pultruded profiles produced under different dies and processing conditions.

The fast reacting resin system applied to this study does not allow for stable processing with the tear drop die. This is due to the relatively large impregnation cavity volume, which creates stagnation regions, i.e. regions with low flow velocities. In combination with the curing kinetics, this leads to a progressive clogging of the chamber with gelled resin. It has been shown that, by reducing the injection nozzle diameter and the conical angle, and thereby the chamber volume, a more favorable flow field can be obtained, i.e. the stagnation volume is reduced. A more detailed study of this die design would demand the conduction of transient simulation studies, to obtain a prediction of the viscosity field in the impregnation chamber and of incipient gelling regions.

In this study, a commercial CFD software was applied, with results comparable to previous self-written simulation codes described in the literature, as was proven in comparing studies for simplified 1D/2D geometries. Considering the possibility of implementing complex geometric models, the present simulation model can be a useful tool in studying other impregnation chamber geometries and/or profile cross sections. The application of a commercial package also facilitates the potential use in an industrial environment, as a support tool for the design of pultrusion dies with closed injection and impregnation chambers.

Appendix

Appendix A: Processing data from pultrusion experimental trials

Table A.1: Processing data from trials with the conical die

	Trial number					
	1	2	3	4	5	6
Fiber stack	<i>GF</i>	<i>GF</i>	<i>GF</i>	<i>CF</i>	<i>CF</i>	<i>CF</i>
Pulling speed [m/min]	0.3	0.3	0.3	0.5	0.3	0.3
Fiber volume content [%]	0.64	0.6	0.57	0.64	0.64	0.6
Set Temperature [°C]	100	100	100	100	100	100
TC1 [°C]	100	100	100	100	100	100
TC2 [°C]	101	101	101	100	100	100
TC3 [°C]	100	100	100	100	100	100
TC4 [°C]	100	100	100	100	100	100
TC5 [°C]	30	31	31	26	27	27
TC6 [°C]	111	111	111	111	111	111
TC7 [°C]	104	104	104	103	103	103
TC8 [°C]	100	100	100	100	100	100
TC9 [°C]	100	100	100	100	100	100
TC10 [°C]	101	100	100	99	99	100
TC11 [°C]	102	102	101	101	100	100
Electrical power, Zone 1 [%]	46.0 ± 5.9	46.2 ± 4.5	46.6 ± 5.0	52.1 ± 5.6	41.6 ± 7.0	44.1 ± 6.2
Electrical power, Zone 2 [%]	1.4 ± 2.9	1.2 ± 2.9	1.9 ± 3.8	1.2 ± 3.1	2.4 ± 4.1	1.9 ± 3.2
Electrical power, Zone 3 [%]	7.2 ± 3.9	7.5 ± 3.3	7.7 ± 3.4	7.4 ± 3.5	8.2 ± 3.6	7.7 ± 2.9
Electrical power, Zone 4 [%]	12.8 ± 5.6	13.1 ± 3.8	13.9 ± 3.9	15.3 ± 6.7	16.8 ± 4.6	17.2 ± 3.2
Pulling force [kN]	12.1 ± 1.5	8.4 ± 1.7	7.7 ± 1.2	1.9 ± 0.2	2.7 ± 1.0	2.8 ± 0.8
Resin injection pressure [bar]	0.4 *	0.4 *	0.4 *	0.4 *	0.4 *	0.4 *
Pressure transducer 1 [bar]	8.9 ± 0.9	5.1 ± 1.2	3.2 ± 0.6	0	0	0
Pressure transducer 2 [bar]	51.9 ± 5.3	33.7 ± 6.4	23.7 ± 2.1	5.9 ± 1.4	7.6 ± 5.7	16.7 ± 4.4

* Resin is injected intermittently.

Table A.2: Processing data from trials with the tear drop die

	Trial number			
	7	8	9	10
Fiber stack	<i>GF</i>	<i>GF</i>	<i>GF</i>	<i>GF</i>
Pulling speed [m/min]	0.5	0.3	0.3	0.3
Fiber volume content [%]	0.64	0.64	0.6	0.64
Set Temperature [°C]	100	100	100	80
TC1 [°C]	100	100	100	80
TC2 [°C]	102	101	100	82
TC3 [°C]	100	100	100	80
TC4 [°C]	17	17	17	21
TC5 [°C]	50	52	53	47
TC6 [°C]	106	106	106	84
TC7 [°C]	105	104	103	83
TC8 [°C]	102	102	101	79
TC9 [°C]	98	98	98	76
Electrical power, Zone 1 [%]	34.1 ± 4.0	25.8 ± 5.0	26.7 ± 6.0	18.2 ± 4.6
Electrical power, Zone 2 [%]	1.5 ± 3.2	2.3 ± 3.8	2.2 ± 4.1	2.2 ± 4.2
Electrical power, Zone 3 [%]	7.1 ± 7.1	6.9 ± 3.9	6.7 ± 3.1	3.7 ± 2.9
Pulling force [kN]	2.1 ± 0.1	3.9 ± 0.2	2.5 ± 0.2	2.8 ± 0.2
Resin injection pressure [bar]	2.3 ± 0.1	3.4 ± 0.7	1.5 ± 0.2	3.0 ± 0.8
Pressure transducer 1 [bar]	0	1.3 ± 0.7	0	1.1 ± 0.7
Pressure transducer 2 [bar]	11.7 ± 1.0	14.5 ± 0.8	7.6 ± 0.5	13.3 ± 0.9

Appendix B: Mesh quality parameters of the tear drop die 3D model

Region	Number of nodes	Number of elements	Average skewness factor	Elements with skewness > 0.75 [%]
1	55146	45000	1.3×10^{-10}	0
2	224406	184500	1.6×10^{-10}	0
3	29484	23850	8.1×10^{-3}	0
4	91728	75150	8.1×10^{-3}	0
5	94071	488474	0.31	0.46
6	16973	80297	0.26	0.47
7	655165	3538915	0.24	0.76

Appendix C: Analytical model for the pressure rise in a conical inlet section

The analytical models proposed by Kim et al. [27] and Ding et al. [10] for the pressure rise function in a conical die inlet, which are based on a 1D flow assumption were found to agree well with simulations in a 2D field. It has also been shown that the analytical model can be generalized to an injection port located at a determined position along the tapered section. An explicit formulation for the pressure rise along the conical inlet section is derived in this appendix. It should be noted that the analytical solution is valid for a unidirectional fiber stack only, because the permeability is expressed as a smooth function of the tapering geometry.

Ding derived from the mass conservation and Darcy's laws the following relationships for the pressure gradients due to drag flow and flow driven by the injection pressure. Refer to Figure 7.5 for the geometrical parameters defined in the equations.

$$\frac{dP_D}{dx} = -\frac{C_G \cdot \eta \cdot U \cdot V_f^2 \cdot h_c^2}{D_f^2} \cdot \frac{(L-x) \tan \theta}{[(1-V_f)h_c + 2(L-x) \tan \theta]^3} \quad \text{Equation B.1}$$

$$\frac{dP_p}{dx} = -\frac{C_G \cdot \eta \cdot U \cdot V_f^2 \cdot h_c^2}{2D_f^2} \cdot \frac{(1-V_f)h_c}{[(1-V_f)h_c + 2(L-x) \tan \theta]^3} \quad \text{Equation B.2}$$

Where P_D and P_p are the pressure distributions due to drag flow and due to the injection pressure, respectively. D_f is the filament diameter and C_G is the shape factor defined by Gebart, with value 57 for a quadratic fiber arrangement. It should be noted that Equation B.1 is exactly the same as Equation 3.30 by neglecting volume change effects. Integration of the above equations yields:

$$P_D = A \cdot \left[\frac{1+2\varepsilon}{2(1+\varepsilon)^2} \right] + C1 \quad \text{Equation B.3}$$

$$P_p = A \cdot \left[\frac{1}{2(1+\varepsilon)^2} \right] + C2 \quad \text{Equation B.4}$$

With A and ε defined as:

$$A = \frac{C_G \cdot \eta \cdot U \cdot h_c \cdot V_f^2}{4D_f^2 \cdot \tan \theta (1-V_f)} \quad \text{Equation B.5}$$

$$\varepsilon = \frac{2(L-x)\tan\theta}{(1-V_f)h_c} \quad \text{Equation B.6}$$

Assuming a location port at a position x_{in} within the conical section where resin is injected under pressure P_{in} , the integration constants C_1 and C_2 can be determined by considering that at this location the superposed flow function, which is valid upstream of the port, equals the downstream drag flow, i.e. $P_D = P_D + P_p$, leading to:

$$P_D = P_{in} \quad \rightarrow \quad C_1 = P_{in} - A \left[\frac{1 + 2\varepsilon_{in}}{2(1 + \varepsilon_{in})^2} \right] \quad \text{Equation B.7}$$

$$P_p = 0 \quad \rightarrow \quad C_2 = -A \left[\frac{1}{2(1 + \varepsilon_{in})^2} \right] \quad \text{Equation B.8}$$

Where ε_{in} is the value of ε calculated at x_{in} . By substituting the integration constants in Equations B.3 and B.4, we arrive at the general pressure function for the conical inlet section:

$$P = P_{in} + A \left[\frac{1}{1 + \varepsilon} - \frac{1}{1 + \varepsilon_{in}} \right], \quad 0 \leq x \leq x_{in} \quad \text{Equation B.9}$$

$$P = P_{in} + A \left[\frac{1 + 2\varepsilon}{2(1 + \varepsilon)^2} - \frac{1 + 2\varepsilon_{in}}{2(1 + \varepsilon_{in})^2} \right], \quad x_{in} \leq x \leq L \quad \text{Equation B.10}$$

References

- [1] R. Bezerra, F. Wilhelm, S. Strauß and H. Ahlborn, "Manufacturing of Complex Shape Composite Parts through the Combination of Pull-braiding and Blow-Moulding," in *20th International Conference on Composite Materials*, Copenhagen, 2015.
- [2] L. Herbeck, *Anforderungen an eine Faserverbund-Produktionstechnik*, DLR, Ed., Braunschweig, 2009.
- [3] S. Bühler, "PulPress - Large scale production of complex sandwich profiles," in *13th World Pultrusion Conference*, Prague, 2016.
- [4] T. F. Starr, *Pultrusion for engineers*, Boca Raton, FL: CRC Press, 2000.
- [5] "Pultrusion | Fiberline Composites," [Online]. Available: <http://fiberline.com/pultrusion>. [Accessed 29 1 2016].
- [6] C. Koppernaes, S. G. Nolet and J. P. Fanucci, "Method and apparatus for wetting fiber reinforcements with matrix materials in the pultrusion process using continuous in-line degasing". United States Patent 5,073,413, 1991.
- [7] J. V. Gauchel and R. N. Lehman, "Apparatus for resin impregnated pultrusion". United States Patent 5,747,075, 1998.
- [8] R. J. Brown, S. Kharchenko, H. D. Coffee and I. Huang, "System for producing pultruded components". United States Patent 8,597,016, 2013.
- [9] M. G. Dubé, G. L. Batch, J. H. Vogel and C. W. Macosko, "Reaction Injection Pultrusion of thermoplastic and thermoset Composites," *Polymer Composites*, vol. 16, no. 5, p. 378–385, 1995.
- [10] Z. Ding, S. Li, H. Yang, J. L. Lee, H. Engelen and P. M. Puckett, "Numerical and experimental analysis of resin flow and cure in resin injection pultrusion (RIP)," *Polymer Composites*, vol. 21 (5), pp. 762-778, 2000.
- [11] M. Connolly, M. Brennan and T. Shidaker, "CFD Modeling of the Closed Injection Wet-Out Process For Pultrusion," in *EPTA's 2008 World Pultrusion Conference*, 2008.
- [12] S. Li, L. Xu, Z. Ding, L. J. Lee and H. Engelen, "Experimental and Theoretical Analysis of Pulling Force in Pultrusion and Resin Injection Pultrusion (RIP)-Part I: Experimental," *Journal of Composite Materials*, vol. 37 (2), pp. 163-189, 2003.
- [13] D. Srinivasagupta, S. Potaraju, J. L. Kardos and B. Joseph, "Steady state and dynamic analysis of a bench-scale injected pultrusion process," *Composites Part A: Applied Science and Manufacturing*, vol. 34, no. 9, p. 835–846, 2003.
- [14] H. Engelen, "Development and Comparison of Resin Injection and Impregnation Chambers for Pultrusion," in *11th World Pultrusion Conference*, Istanbul, 2012.

- [15] J. K. Gillham, "Formation and Properties of Thermosetting and High Tg Polymeric Materials," *Polymer Engineering and Science*, pp. 1429-1433, 26 November 1986.
- [16] P. J. Halley and M. E. Mackay, "Chemorheology of thermosets - an overview," *Polymer Engineering & Science*, vol. 36, no. 5, pp. 593-609, 1996.
- [17] A. Yousefi, P. G. Lafleur and R. Gauvin, "Kinetic studies of thermoset cure reactions: A review," *Polymer Composites*, vol. 18, no. 2, pp. 157-168, 1997.
- [18] M. R. Kamal and S. Sourour, "Kinetics and thermal characterization of thermoset cure," *Polymer Engineering and Science*, vol. 13, no. 1, pp. 59-64, 1973.
- [19] M. R. Kamal, "Thermoset characterization for moldability analysis," *Polymer Engineering and Science*, vol. 14, no. 3, pp. 231-239, 1974.
- [20] W. I. Lee, A. C. Loos and G. S. Springer, "Heat of Reaction, Degree of Cure, and Viscosity of Hercules 3501-6 Resin," *Journal of Composite Materials*, vol. 16, no. 6, pp. 510-520, 1982.
- [21] I. V. Arkhangel'skii, *Non-isothermal kinetic methods*, 1. publ ed., vol. 1, Berlin: Ed. Open Access, 2013, p. 65 S.
- [22] J. Opfermann, "Kinetic Analysis Using Multivariate Non-linear Regression. I. Basic concepts," *Journal of Thermal Analysis and Calorimetry*, vol. 60, no. 2, p. 641-658, 2000.
- [23] H. L. Price Jr, "Curing and Flow of Thermosetting Resins for Composite Material Pultrusion," Old Dominion University, 1979.
- [24] L. Aylward, G. Douglas and D. Roylance, "A transient finite element model for pultrusion processing," *Polymer Process Engineering*, no. 3(3), pp. 247-261, 1985.
- [25] G. L. Batch and C. W. Macosko, "Heat Transfer and Cure in Pultrusion: Model and Experimental Verification," *AIChE Journal*, vol. 39 (7), pp. 1228-1241, 1993.
- [26] C. D. Han and D. S. Lee, "Development of a mathematical model for the pultrusion process," *Polymer Engineering and Science*, vol. 26, pp. 393-404, 1986.
- [27] D.-H. Kim, P.-G. Han, G.-H. Jin and W. I. Lee, "A Model for Thermosetting Composite Pultrusion Process," *Journal of Composite Materials*, vol. 31 (20), pp. 2105-2122, 1997.
- [28] S. JOSHI and Y. LAM, "Integrated approach for modelling cure and crystallization kinetics of different polymers in 3D pultrusion simulation," *Journal of Materials Processing Technology*, vol. 174, no. 1-3, pp. 178-182, 2006.
- [29] J. Blaurock, "Zur Optimierung des Strangziehverfahrens für endlosfaserverstärkte, hochfeste Kunststoffprofile," Aachen, 1999.
- [30] I. Baran, R. Akkerman and J. H. Hattel, "Material characterization of a polyester resin system for the pultrusion process," *Composites Part B: Engineering*, vol. 64, pp. 194-

- 201, 2014.
- [31] Z. Ding, S. Li and L. J. Lee, "Influence of heat transfer and curing on the quality of pultruded composites. II: Modeling and simulation," *Polymer Composites*, vol. 23, no. 5, pp. 957-969, 2002.
- [32] A. D. Freed, "Modelling the pultrusion process to obtain low void fraction composites," West Virginia University, 06.05.2002.
- [33] S. Li, L. Xu, Z. Ding, L. J. Lee and H. Engelen, "Experimental and Theoretical Analysis of Pulling Force in Pultrusion and Resin Injection Pultrusion (RIP) - Part II: Modeling and Simulation," *Journal of Composite Materials*, vol. 37 (3), pp. 195-216, 2003.
- [34] R. M. Hackett and S.-Z. Zhu, "Two-Dimensional Finite Element Model of the Pultrusion Process," *Journal of Reinforced Plastics and Composites*, vol. 11, no. 12, pp. 1322-1351, 1992.
- [35] S. Kommu, B. Khomami and J. L. Kardos, "Modeling of injected pultrusion processes: A numerical approach," *Polymer Composites*, vol. 19, no. 4, pp. 335-346, 1998.
- [36] I. Mustafa, B. Khomami and J. L. Kardos, "3-D nonisothermal flow simulation model for injected pultrusion processes," *AIChE Journal*, vol. 45, no. 1, pp. 151-163, 1999.
- [37] H. Ng and I. Manas-zloczower, "A nonisothermal differential scanning calorimetry study of the curing kinetics of an unsaturated polyester system," *Polymer Engineering and Science*, vol. 29, no. 16, pp. 1097-1102, 1989.
- [38] H. Ng and I. Manas-Zloczower, "Kinetic studies of a composite thermoset cure reaction - application in pultrusion simulations," *Polymer Engineering and Science*, vol. 29, no. 5, pp. 302-307, 1989.
- [39] S. M. Moschiar, M. M. Reboledo, J. M. Kenny and A. Vázquez, "Analysis of pultrusion processing of composites of unsaturated polyester resin with glass fibers," *Polymer Composites*, vol. 17, no. 3, pp. 478-485, 1996.
- [40] R. Gorthala, J. A. Roux and J. G. Vaughan, "Resin Flow, Cure and Heat Transfer Analysis for Pultrusion Process," *Journal of Composite Materials*, vol. 28, pp. 486-506, 1994.
- [41] R. Gorthala, J. Roux, J. Vaughan and R. Donti, "Comparison of Processing Parameters for Pultruded Graphite/Epoxy and Fiberglass/Epoxy: A Heat Transfer and Curing Model," *Journal of Reinforced Plastics and Composites*, vol. 13, no. 4, pp. 288-300, 1994.
- [42] Y. R. Chachad, J. A. Roux, J. G. Vaughan and E. Arafat, "Three-Dimensional Characterization of Pultruded Fiberglass-Epoxy Composite Materials," *Journal of Reinforced Plastics and Composites*, vol. 14, pp. 495-512, 1995.

- [43] Y. R. Chachad, J. A. Roux, J. G. Vaughan and E. S. Arafat, "Effects of Pull Speed on Die Wall Temperatures for Flat Composites of various Sizes," *Journal of Reinforced Plastics and Composites*, no. 15, pp. 718-739, 1996.
- [44] Y. R. Chachad, J. A. Roux, J. G. Vaughan and E. S. Arafat, "Thermal Model for Three-Dimensional Irregular Shaped Pultruded Fiberglass Composites," *Journal of Composite Materials*, vol. 30 (6), pp. 692-721, 1996.
- [45] M. Valliappan, J. A. Roux and J. G. Vaughan, "Temperature and Cure in Pultruded Composites Using Multi-Step Reaction Model for Resin," *Journal of Reinforced Plastics and Composites*, vol. 15, pp. 295-321, 1996.
- [46] M. Valliappan, J. A. Roux, J. G. Vaughan and E. S. Arafat, "Die and post-die temperature and cure in graphite/epoxy composites," *Composites Part B: Engineering*, vol. 27, no. 1, pp. 1-9, 1996.
- [47] B. R. Suratno, L. Ye and Y.-W. Mai, "Simulation of temperature and curing profiles in pultruded composite rods," *Composites Science and Technology*, vol. 58, no. 2, pp. 191-197, 1998.
- [48] X. Lin Liu, I. G. Crouch and Y. C. Lam, "Simulation of heat transfer and cure in pultrusion with a general-purpose finite element package," *Composites Science and Technology*, vol. 60, no. 6, pp. 857-864, 2000.
- [49] S. C. Joshi and Y. C. Lam, "Three-dimensional finite-element/nodal-control-volume simulation of the pultrusion process with temperature-dependent material properties including resin shrinkage," *Composites Science and Technology*, vol. 61, pp. 1539-1547, 2001.
- [50] P. Carlone, G. Palazzo and R. Pasquino, "Pultrusion manufacturing process development by computational modelling and methods," *Mathematical and Computer Modelling*, vol. 44, no. 7-8, pp. 701-709, 2006.
- [51] P. Carlone, G. Palazzo and R. Pasquino, "Pultrusion manufacturing process development: Cure optimization by hybrid computational methods," *Computers & Mathematics with Applications*, vol. 53, no. 9, pp. 1464-1471, 2007.
- [52] J. H. Lee and J. W. Lee, "Kinetic parameters estimation for cure reaction of epoxy based vinyl ester resin," *Polymer Engineering and Science*, vol. 34, no. 9, pp. 742-749, 1994.
- [53] X. -L. Liu, "Numerical modeling on pultrusion of composite I beam," *Composites Part A: Applied Science and Manufacturing*, vol. 32, no. 5, pp. 663-681, 2001.
- [54] T. Mezger, *Das Rheologie-Handbuch*, 3., überarb. Aufl. ed., Hannover: Vincentz Network, 2010, p. 441 S..

- [55] J. D. Ferry, *Viscoelastic properties of polymers*, 3d ed ed., New York: Wiley, 1980, pp. xxiv, 641.
- [56] W. P. Cox and E. H. Merz, "Correlation of dynamic and steady flow viscosities," *Journal of Polymer Science*, vol. 28, no. 118, pp. 619-622, 1958.
- [57] H. H. Winter, "Can the gel point of a cross-linking polymer be detected by the G' - G'' crossover?," *Polymer Engineering and Science*, vol. 27, no. 22, pp. 1698-1702, 1987.
- [58] *Test Method for Plastics: Dynamic Mechanical Properties: Cure Behavior*, West Conshohocken, PA, 2008.
- [59] J. M. Castro and C. W. Macosko, "Studies of mold filling and curing in the reaction injection molding process," *AIChE Journal*, vol. 28, no. 2, p. 250–260, 1982.
- [60] T. A. Osswald and N. Rudolph, *Polymer rheology*, Cincinnati: Hanser Publications, 2015, pp. xi, 225.
- [61] T. G. Gutowski, Z. Cai, S. Bauer, D. Boucher, J. Kingery and S. Wineman, "Consolidation Experiments for Laminate Composites," *Journal of Composite Materials*, vol. 21, no. 7, pp. 650-669, 1987.
- [62] Y. R. Kim, S. P. McCarthy and J. P. Fanucci, "Compressibility and relaxation of fiber reinforcements during composite processing," *Polymer Composites*, vol. 12, no. 1, pp. 13-19, 1991.
- [63] G. L. Batch, S. Cumiskey and C. W. Macosko, "Compaction of fiber reinforcements," *Polymer Composites*, vol. 23, no. 3, pp. 307-318, 2002.
- [64] R. Arbter et al, "Experimental determination of the permeability of textiles: A benchmark exercise," *Composites Part A: Applied Science and Manufacturing*, vol. 42, no. 9, pp. 1157-1168, 2011.
- [65] S. Whitaker, "Flow in porous media I: A theoretical derivation of Darcy's law," *Transport in Porous Media*, vol. 1, no. 1, pp. 3-25, 1986.
- [66] R. B. Bird, W. E. Stewart and E. N. Lightfoot, *Transport phenomena*, Rev. 2nd ed ed., New York: J. Wiley, 2007, pp. xii, 905.
- [67] K. L. Adams, W. B. Russel and L. Rebenfeld, "Radial penetration of a viscous liquid into a planar anisotropic porous medium," *International Journal of Multiphase Flow*, vol. 14, no. 2, pp. 203-215, 1988.
- [68] A. W. Chan and S.-T. Hwang, "Anisotropic in-plane permeability of fabric media," *Polymer Engineering and Science*, vol. 31, no. 16, p. 1233–1239, 1991.
- [69] J. R. Weitzenböck, R. A. Shenoi and P. A. Wilson, "Radial flow permeability measurement. Part A: Theory," *Composites Part A: Applied Science and Manufacturing*, vol. 30, no. 6, p. 781–796, 1999.

- [70] J. R. Weitzenböck, R. A. Shenoi and P. A. Wilson, "Radial flow permeability measurement. Part B: Application," *Composites Part A: Applied Science and Manufacturing*, vol. 30, no. 6, p. 797–813, 1999.
- [71] K. K. Han, C. W. Lee and P. R. Rice, "Measurements of the permeability of fiber preforms and applications," *Composites Science and Technology*, vol. 60, no. 12-13, p. 2435–2441, 2000.
- [72] R. Arbter, "Contribution to robust resin transfer molding," ETH, Zürich, 2008.
- [73] N. Vernet et al, "Experimental determination of the permeability of engineering textiles: Benchmark II," *Composites Part A: Applied Science and Manufacturing*, vol. 61, pp. 172-184, 2014.
- [74] B. R. Gebart, "Permeability of Unidirectional Reinforcements for RTM," *Journal of Composite Materials*, vol. 26, no. 8, pp. 1100-1133, 1992.
- [75] Westhuizen, Josiasvd, Du Plessis, J. Prieur, "Quantification of Unidirectional Fiber Bed Permeability," *Journal of Composite Materials*, vol. 28, no. 7, pp. 619-637, 1994.
- [76] J. Beckman, R. Lehman, J. Gauchel, R. Werner, Z. Kusibab, J. Kufner and B. Werner, *A Method for Producing Ladder Rail Using High Pressure Injection Die Impregnation*, Owens Corning Technical Paper No. 1-PL-19592, 1995.
- [77] P. J. Bates, D. Taylor and M. Cunningham, "Transverse Permeability of Direct Glass Rovings," *Journal of Reinforced Plastics and Composites*, vol. 19, no. 15, pp. 1217-1226, 2000.
- [78] J. S. U. Schell, M. Siegrist and P. Ermanni, "Experimental Determination of the Transversal and Longitudinal Fibre Bundle Permeability," *Applied Composite Materials*, vol. 14, no. 2, pp. 117-128, 2007.
- [79] J. D. Anderson, *Computational fluid dynamics*, New York: McGraw-Hill, 1995, pp. xxiv, 547.
- [80] S. V. Patankar, *Numerical heat transfer and fluid flow*, Washington; New York: Hemisphere Pub. Corp.; McGraw-Hill, 1980, pp. xiii, 197.
- [81] *Ansys CFX 14.0 Help*.
- [82] S. U. Gadam, J. A. Roux, T. A. McCarty and J. G. Vaughan, "The impact of pultrusion processing parameters on resin pressure rise inside a tapered cylindrical die for glass-fibre/epoxy composites," *Composites Science and Technology*, vol. 60, pp. 945-958, 2000.
- [83] K. S. Raper, J. A. Roux, T. A. McCarty and J. G. Vaughan, "Investigation of the pressure behavior in a pultrusion die for graphite/epoxy composites," *Composites Part A: Applied Science and Manufacturing*, vol. 30 (9), pp. 1123-1132, 1999.

- [84] D. Sharma, T. A. McCarty, J. A. Roux and J. G. Vaughan, "Fluid mechanics analysis of a two-dimensional pultrusion die inlet," *Polymer Engineering & Science*, vol. 38, no. 10, pp. 1611-1622, 1998.
- [85] D. Sharma, T. A. McCarty, J. A. Roux and J. G. Vaughan, "Investigation of Dynamic Pressure Behavior in a Pultrusion Die," *Journal of Composite Materials*, vol. 32, no. 10, pp. 929-950, 1998.
- [86] D. Sharma, T. A. McCarty, J. A. Roux and J. G. Vaughan, "Pultrusion die pressure response to changes in die inlet geometry," *Polymer Composites*, vol. 19 (2), pp. 180-192, 1998.
- [87] I. Baran, C. C. Tutum, M. W. Nielsen and J. H. Hattel, "Process induced residual stresses and distortions in pultrusion," *Composites Part B: Engineering*, vol. 51, p. 148–161, 2013.
- [88] T. A. Bogetti and J. W. Gillespie, "Two-Dimensional Cure Simulation of Thick Thermosetting Composites," *Journal of Composite Materials*, vol. 25, no. 3, p. 239–273, 1991.
- [89] T. A. Bogetti and J. W. Gillespie, "Process-Induced Stress and Deformation in Thick-Section Thermoset Composite Laminates," *Journal of Composite Materials*, vol. 26, no. 5, p. 626–660, 1992.
- [90] A. Johnston, R. Vaziri and A. Poursartip, "A Plane Strain Model for Process-Induced Deformation of Laminated Composite Structures," *Journal of Composite Materials*, vol. 35, no. 16, p. 1435–1469, 2001.
- [91] I. Baran, J. H. Hattel, R. Akkerman and C. C. Tutum, "Mechanical Modelling of Pultrusion Process," *Applied Composite Materials*, vol. 22, no. 1, p. 99–118, 2015.
- [92] I. Baran, R. Akkerman and J. H. Hattel, "Modelling the pultrusion process of an industrial L-shaped composite profile," *Composite Structures*, vol. 118, p. 37–48, 2014.
- [93] I. Baran, J. H. Hattel and R. Akkerman, "Investigation of process induced warpage for pultrusion of a rectangular hollow profile," *Composites Part B: Engineering*, vol. 68, p. 365–374, 2015.
- [94] I. Baran, J. H. Hattel, C. C. Tutum and R. Akkerman, "Pultrusion of a vertical axis wind turbine blade part-II," *International Journal of Material Forming*, vol. 8, no. 3, p. 367–378, 2015.
- [95] P. Carlone, I. Baran, J. H. Hattel and G. S. Palazzo, "Computational Approaches for Modeling the Multiphysics in Pultrusion Process," *Advances in Mechanical Engineering*, vol. 5, no. 0, p. 301875, 2013.
- [96] S. Voorakaranam, B. Joseph and J. L. Kardos, "Modeling and Control of an Injection

- Pultrusion Process," *Journal of Composite Materials*, vol. 33, no. 13, p. 1173–1204, 1999.
- [97] X.-L. Liu, "A finite element/nodal volume technique for flow simulation of injection pultrusion," *Composites Part A: Applied Science and Manufacturing*, vol. 34, no. 7, p. 649–661, 2003.
- [98] X.-L. Liu, "Iterative and transient numerical models for flow simulation of injection pultrusion," *Composite Structures*, vol. 66, no. 1-4, p. 175–180, 2004.
- [99] S. S. Rahatekar and J. A. Roux, "Numerical Simulation of Pressure Variation and Resin Flow in Injection Pultrusion," *Journal of Composite Materials*, vol. 37, no. 12, p. 1067–1082, 2003.
- [100] S. S. Rahatekar, "Injection Pultrusion Simulation for Polyester/Glass Mat/Rovings/Mat Composites," *Journal of Reinforced Plastics and Composites*, vol. 24, no. 1, p. 53–68, 2005.
- [101] A. L. Jeswani, J. A. Roux and J. G. Vaughan, "Multiple Injection Ports and Part Thickness Impact on Wetout of High Pull Speed Resin Injection Pultrusion," *Journal of Composite Materials*, vol. 43, no. 19, p. 1991–2009, 2009.
- [102] B. K. Ranga, J. A. Roux, J. G. Vaughan and A. L. Jeswani, "Effect of injection chamber length and pull speed of tapered resin injection pultrusion," *Journal of Reinforced Plastics and Composites*, vol. 30, no. 16, p. 1373–1387, 2011.
- [103] D. R. Palikhel, J. A. Roux and A. L. Jeswani, "Die-Attached Versus Die-Detached Resin Injection Chamber for Pultrusion," *Applied Composite Materials*, vol. 20, no. 1, p. 55–72, 2013.
- [104] "Origin Help," [Online]. Available: <http://www.originlab.com/doc/Origin-Help/NLFit-Theory>. [Accessed 14 1 2016].
- [105] R. Bezerra, F. Wilhelm and F. Henning, "Compressibility and permeability of fiber reinforcements for pultrusion," 2014.
- [106] F. Wilhelm, "Konzeption, Konstruktion und Erprobung eines Versuchsaufbaus für die Ermittlung der Permeabilität von Textilhalbzeugen in der Ebene," Karlsruher Institut für Technologie, Karlsruhe, 13.09.2013.
- [107] B. Beck, "Messung der Abzugskräfte im Pultrusionsprozess in Abhängigkeit von Profildicke und Fasergehalt," Karlsruher Institut für Technologie, Karlsruhe, 30.08.2011.
- [108] I. Baran, C. C. Tutum and J. H. Hattel, "The effect of thermal contact resistance on the thermosetting pultrusion process," *Composites Part B: Engineering*, vol. 45, no. 1, p. 995–1000, 2013.